

COMPUTATIONAL METHODS FOR IDEAL
MAGNETOHYDRODYNAMICS

by

Andrew D. Kercher

A Dissertation

Submitted to the

Graduate Faculty

of

George Mason University

In Partial fulfillment of

The Requirements for the Degree

of

Doctor of Philosophy

Computational Science and Informatics

Committee:

Dr. Robert Weigel, Dissertation Director

Dr. Rainald Löhner, Committee Member

Dr. Jie Zhang, Committee Member

Dr. Fernando Camelli, Committee Member

Dr. Chi Yang, Director, School of Physics,
Astronomy, and Computational Sciences

Dr. Donna M. Fox, Associate Dean,
Office of Student Affairs & Special Programs,
College of Science

Dr. Peggy Agouris, Dean,
College of Science

Date: _____

Fall Semester 2014

George Mason University

Fairfax, VA

Computational Methods for Ideal Magnetohydrodynamics

A dissertation submitted in partial fulfillment of the requirements for the degree of
Doctor of Philosophy at George Mason University

By

Andrew D. Kercher
Bachelor of Science
George Mason University, 2008

Director: Dr. Robert Weigel, Professor
School of Physics, Astronomy, and Computational Science

Fall Semester 2014
George Mason University
Fairfax, VA

Copyright © 2014 by Andrew D. Kercher
All Rights Reserved

Dedication

This dissertation is dedicated to my wife, without whom, I would have faltered.

Acknowledgments

First, I would like thank my adviser, Dr. Robert Weigel for all his help and support throughout the years, for working on the weekend, and for guiding me through my graduate studies.

Second, I would like to thank Dr. Rainald Löhner for introducing me to computational fluid dynamics, for taking the time to answer all my questions, and for helping me overcome the initial problems I encountered during code development.

Third, I would like to thank Andrew Corrigan for always being available when I hit a wall.

Forth, I would like to thank Dr. Jie Zhang and Dr. Fernando Camelli for their time and effort.

My final thanks is to my friends and family for their love and support; to my daughter Abigail, for keeping a smile on my face during the frustrating times; to my expected child for keeping me motivated, and above all, to Anita for everything.

Table of Contents

	Page
List of Tables	vii
List of Figures	viii
Abbreviations	xiv
Abstract	xvi
1 Introduction	1
2 Riemann problems and conservative systems	5
2.1 Formulation	5
2.2 Linear advection	6
2.3 Linear systems	7
2.4 Nonlinear systems	9
2.5 Compressible hydrodynamics	12
2.5.1 Exact Riemann solvers	14
2.5.2 Approximate Riemann solvers	17
2.6 Ideal magnetohydrodynamics	26
2.6.1 Waves in ideal magnetohydrodynamics	27
2.6.2 Shock classification	28
2.6.3 Nonlinear Riemann solver	29
2.6.4 HLLD approximate Riemann solver	32
3 Numerical solutions for ideal magnetohydrodynamics	37
3.1 Finite volume discretization and Godunov's method	38
3.2 Higher-order extensions	40
3.3 Riemann problems of ideal magnetohydrodynamics	46
3.4 Numerical tests	47
3.5 Non-unique solutions to Riemann problems of ideal magnetohydrodynamics	67
3.6 Nonuniform convergence	72
4 Compound wave modification	74
4.1 Convergence with finite volume schemes	74
4.2 Error analysis	85

5	Parallel processing	89
5.1	Methods for ideal MHD in higher dimensions	89
5.2	Shared memory parallelism	93
5.3	Efficient algorithms	95
5.4	Performance results	100
6	Conclusion	105
A	Derivation of HLL fluxes	108
B	Thrust templates	109
C	Kelvin-Helmholtz instability initial conditions	110
	Bibliography	111

List of Tables

Table	Page
3.1 Exact solution of MHD shock tube test 1 (solid black line of Figure 3.8)	62
3.2 Residual and wave speeds of MHD shock tube test 1	62
3.3 Exact solution of MHD shock tube test 2 (solid black line of Figure 3.9)	62
3.4 Residual and wave speeds of MHD shock tube test 2	62
3.5 Exact solution of MHD shock tube test 3 (solid black line of Figure 3.10)	63
3.6 Residual and wave speeds of MHD shock tube test 3	63
3.7 Exact solution of MHD shock tube test 4 (solid black line of Figure 3.11)	63
3.8 Residual and wave speeds of MHD shock tube test 4	63
3.9 Exact solution of MHD shock tube test 5a (solid black line of Figure 3.12)	64
3.10 Residual and wave speeds of MHD shock tube test 5a	64
3.11 Exact solution of MHD shock tube test 5b (solid black line of Figure 3.13)	64
3.12 Residual and wave speeds of MHD shock tube test 5b	64
3.13 Exact solution of MHD shock tube test 6a (solid black line of Figure 3.14)	65
3.14 Residual and wave speeds of MHD shock tube test 6a	65
3.15 Exact solution of MHD shock tube test 6b (solid black line of Figure 3.15)	65
3.16 Residual and wave speeds of MHD shock tube test 6b	65
3.17 Exact solution of MHD shock tube test 7 (solid black line of Figure 3.16)	66
3.18 Residual and wave speeds of MHD shock tube test 7	66
5.1 Performance comparison of GPU and CPU.	103

List of Figures

Figure	Page
2.1 Initial conditions for a one-dimensional Riemann problem. The initial discontinuity at, x_d , separates two constant states, \mathbf{U}_l and \mathbf{U}_r	6
2.2 Solution to the Riemann problem for linear advection in the x - t plane. The position of the discontinuity is given by the dashed line.	7
2.3 Solution to the Riemann problem for a hyperbolic system of n linear equations in the x - t plane.	9
2.4 (left) Characteristics on both sides of a shock, (center) linear discontinuity, and (right) rarefaction (right).	10
2.5 Solution to a Riemann with one intermediate state in the x - t plane.	11
2.6 Possible structure of the solution to a Riemann problem for the Euler equations the x - t plane. The solution consists of a rarefaction wave to the left of contact discontinuity, and a shock wave to the right.	14
2.7 Exact solution to Sod shock tube problem. The head of the rarefaction is located at $x \approx 0.2$, and the tail is at $x \approx 0.45$. The contact discontinuity is located at $x \approx 0.72$, and the shock is located $x \approx 0.95$	16
2.8 Restoration of the contact discontinuity in the HLLC approximate Riemann solver.	19
2.9 HLLE (left), and HLLC (right) approximate solutions for a slow moving contact discontinuity. Athena [30] was used to compute the approximate solutions. The exact solution was computed with code written for this dissertation: https://github.com/akercher/dissertation	21
2.10 HLLE (Top row), HLLC (middle row), and Roe (bottom row) approximate solution to Sod shock tube problem computed using first-order piece-wise constant interpolation. Athena [30] was used to compute the approximate solutions. The exact solution was computed with code written for this dissertation available at: https://github.com/akercher/dissertation	25

2.11	Seven possible waves and/or discontinuities separating the eight possible regions, or states of the ideal MHD Riemann problem. The initial contact discontinuity, i.e., the entropy wave, separates regions \mathbf{U}_{3l}^* and \mathbf{U}_{3r}^*	30
2.12	Intermediate states and waves used in the HLLD approximate Riemann solver.	33
3.1	Piecewise constant (dotted line) and piecewise linear (solid line) reconstruction of interface states that define the local Riemann problem for Godunov's method.	39
3.2	(Top row) HLLE, (middle row) HLLC, and (bottom row) Roe approximate solution to Sod shock tube problem computed using third-order parabolic interpolation. Athena [30] was used to compute the approximate solutions. The exact solution was computed with code written for this dissertation available at: https://github.com/akercher/dissertation	41
3.3	The allowable range for the high order solution is defined such that monotonicity is preserved.	43
3.4	(Top row) Rusanov without FCT , and (bottom row) with FCT, approximate solutions to Sod shock tube problem on a grid of 512 points. Solutions computed with code written for this dissertation available at: https://github.com/akercher/dissertation	45
3.5	Initial configuration of magnetic field on both sides of the discontinuity. The initial twist angle $\alpha = \psi_r - \psi_l$ is the difference in rotation angles of the left and right tangential field.	47
3.6	The density and tangential magnetic field of the solution to a Riemann problem of ideal MHD. All rotations are about the x-axis. In the reference frame of the CD, the direction of each wave w.r.t. the x-axis is positive for those under the solid blue line, and negative for those under the solid red line. . .	48
3.7	A view in the positive x-direction of Figure 3.6. The influence of regular waves on the tangential magnetic field for a non-planar Riemann problem of ideal MHD. The orientation of the tangential magnetic field is given by the angle $\psi = \tan B_z/B_y$. Regular waves only influence the magnitude or orientation of the tangential magnetic field. The intermediate states are defined in Figure 2.11, with $\mathbf{B}_{t3l}^* = \mathbf{B}_{t3r}^*$ denoted by the CD.	48

3.8	Solution of MHD shock tube test 1 at time 0.2. The initial conditions are given by (3.29). HLLC-TVD solution generated with Athena [30]. All other solutions generated with code written for this dissertation: https://github.com/akercher/dissertation .	53
3.9	Solution of MHD shock tube test 2 at time 0.2. The initial conditions are given by (3.30). HLLC-TVD solution generated with Athena [30]. All other solutions generated with code written for this dissertation: https://github.com/akercher/dissertation .	54
3.10	Solution of MHD shock tube test 3 at time 0.3. The initial conditions are given by (3.31). HLLC-TVD solution generated with Athena [30]. All other solutions generated with code written for this dissertation: https://github.com/akercher/dissertation .	55
3.11	Solution of MHD shock tube test 4 at time 0.2. The initial conditions are given by (3.32). HLLC-TVD solution generated with Athena [30]. All other solutions generated with code written for this dissertation: https://github.com/akercher/dissertation .	56
3.12	Solution of MHD shock tube test 5a (3.33) with $\alpha = \pi$, at time 0.2066. HLLC-TVD solution generated with Athena [30]. All other solutions generated with code written for this dissertation: https://github.com/akercher/dissertation .	57
3.13	Solution of MHD shock tube test 5b (3.33) with $\alpha = 3.0$, at time 0.2066. HLLC-TVD solution generated with Athena [30]. All other solutions generated with code written for this dissertation: https://github.com/akercher/dissertation .	58
3.14	Solution of MHD shock tube test 6a (3.34) with $\alpha = \pi$, at time 0.15. HLLC-TVD solution generated with Athena [30]. All other solutions generated with code written for this dissertation: https://github.com/akercher/dissertation .	59
3.15	Solution of MHD shock tube test 6b (3.34) with $\alpha = 3.0$, at time 0.15. HLLC-TVD solution generated with Athena [30]. All other solutions generated with code written for this dissertation: https://github.com/akercher/dissertation .	60

3.16	Solution of MHD shock tube test 7 (3.35) at time 0.05. HLLC-TVD solution generated with Athena [30]. All other solutions generated with code written for this dissertation: https://github.com/akercher/dissertation	61
3.17	Initial configuration for a coplanar magnetic field on both sides of the discontinuity.	68
3.18	Non-convergence for the coplanar case. A non-regular structure (compound wave) in the approximate solution exists in place of the rotational discontinuity in the exact solution at $x = 0.303$. The domain used for error analysis is $x = [0.254, 0.481]$	69
3.19	Non-convergence for the coplanar case. A non-regular structure (compound wave) in the approximate solution exists in place of the rotational discontinuity in the exact solution at $x = 0.365$. The domain used for error analysis is $x = [0.346, 0.551]$	70
3.20	Top: initial state of left-going rotational discontinuity for the coplanar case of Test 5. Middle: the left-going rotational discontinuity for the coplanar case of Test 5 after onetime step. The gas pressure is increased as a result of the decrease in B_t . Bottom: the left-going rotational discontinuity for the coplanar case of Test 5 after two time steps. The artificial increase in pressure creates the compound wave.	71
3.21	Pseudo-convergence for a near-coplanar case. As the grid is refined from 1024 and 2048 points, the solution begins to diverge from the c-solution.	73
3.22	Pseudo-convergence for a near-coplanar case. As the grid is refined from 1024 and 2048 points, the solution begins to diverge from the c-solution.	73
4.1	The slow compound wave of Test 5a, approximate non-converging c-solution, and exact r-solution for the coplanar case.	75
4.2	The fast compound wave of Test 6a, approximate non-converging c-solution, and exact r-solution for the coplanar case.	76
4.3	The approximate solution after the first flux correction of HLLD-CWM and exact r-solution to the full Riemann problem for the near-coplanar case with 4096 grid points. The compound wave is almost completely removed, except near $x = 0.303$ where a weak intermediate shock remains.	78

4.4	The approximate solution after the first flux correction of HLLD-CWM and exact r-solution to the full Riemann problem for the near-coplanar case with 2048 grid points. The compound wave is almost completely removed, except near $x = 0.365$ a weak intermediate shock remains.	78
4.5	The approximate solution after the first flux correction of HLLD-CWM and exact r-solution to the full Riemann problem for the near-coplanar case with 2048 grid points. The compound wave is almost completely removed, except near $x = 0.365$ where a weak intermediate shock remains.	79
4.6	The approximate solution after the first flux correction of HLLD-CWM and exact r-solution to the full Riemann problem for the near-coplanar case of Test 5 with 4096 grid points. The compound wave is almost completely removed, except near $x = 0.366$ and $x = 0.691$ where weak intermediate shocks remain.	79
4.7	The rotational discontinuity and slow shock solution found using HLLD-CWM without the (optional) flux redistribution step, HLLD, and the exact solver using 512 grid points for (top) a near-coplanar and pseudo-converging case and (bottom) the planar and non-converging (bottom) case.	80
4.8	The rotational discontinuity and slow shock solution found using HLLD-CWM after the (optional) flux redistribution step, HLLD, and the exact solver using 2048 grid points for (top) a near-coplanar and pseudo-converging case and (bottom) the planar and non-converging (bottom) case.	81
4.9	The fast rarefaction and rotational discontinuity solution found using HLLD-CWM without the (optional) flux redistribution step, HLLD, and the exact solver using 512 grid points for (top) a near-coplanar and pseudo-converging case and (bottom) the planar and non-converging (bottom) case.	82
4.10	The fast rarefaction and rotational discontinuity solution found using HLLD-CWM without the (optional) flux redistribution step, HLLD, and the exact solver using 2048 grid points for (top) a near-coplanar and pseudo-converging case and (bottom) the planar and non-converging (bottom) case.	83
4.11	Solution consisting of two fast rarefactions and two rotational discontinuities found using HLLD-CWM without the (optional) flux redistribution step, HLLD, and the exact solver using 2048 grid points for the non-planar case.	84

4.12	The approximate solution after the first flux correction of HLLD-CWM and exact r-solution to the full Riemann problem for the near-coplanar case with 2048 grid points. The compound wave is almost completely removed, except near $x = 0.365$ where a weak intermediate shock remains.	85
4.13	RMSE in $x = [0.254, 0.481]$ using HLLD (blue) and HLLD-CWM (red) for Tests (left) 5a and (right) 5b.	86
4.14	RMSE in $x = [0.348, 0.551]$ using HLLD (blue) and HLLD-CWM (red) for Tests (left) 6a and (right) 6b.	87
5.1	Staggered field geometry of the constrained transport scheme. The components of the magnetic field are located at the cell interfaces, ξ_z is located at the cell corners.	91
5.2	Colored grouping of interior faces for avoiding memory contention with cell centered finite volume schemes. Four groups, labeled 1-4, are required. . . .	94
5.3	Colored grouping of interior faces for avoiding memory contention with cell centered finite volume schemes plus constrained transport. Eight groups, labeled 1-8, are required.	95
5.4	The Kelvin-Helmoltz instability, ρ at times: $t = 1$ (top) and $t = 5$ (bottom). Simulation performed on a 400×400 grid of triangular elements with code written for this dissertation available at: https://github.com/akercher/dissertation	101
5.5	Spherical blast waves at times: $t = 0.2$ (left) and $t = 1.75$ (right). Simulation performed on a 400×600 grid of quadrilateral elements with code written for this dissertation available at: https://github.com/akercher/dissertation	102
C.1	Initial conditions of the Kelvin-Helmoltz instability problem. See Section 5.4 for solutions at times $t=1$ and $t=5$	110

Abbreviations

AoS array of structures.

CD contact discontinuity.

CLF Courant-Friedrichs-Lowy.

CT constrained transport.

CTU corner transport upwind.

CUDA compute unified device architecture.

FCT flux corrected transport.

FCW fast compound wave.

FLOPS floating-point operations per second.

FR fast rarefaction.

FS fast shocks.

FV finite volume.

GPU graphics processing unit.

HD hydrodynamics.

IS intermediate shocks.

IVP initial value problem.

MHD magnetohydrodynamics.

OMP OpenMP.

PPM piece-wise parabolic method.

RD rotational discontinuity.

RMSE root-mean-square-error.

SCW slow compound wave.

SoA structure of arrays.

SR slow rarefaction.

SS slow shocks.

STL Standard Template Library.

TBB thread building blocks.

TVD total variation diminishing.

VL van Leer.

Abstract

COMPUTATIONAL METHODS FOR IDEAL MAGNETOHYDRODYNAMICS

Andrew D. Kercher, PhD

George Mason University, 2014

Dissertation Director: Dr. Robert Weigel

Numerical schemes for the ideal magnetohydrodynamics (MHD) are widely used for modeling space weather and astrophysical flows. They are designed to resolve the different waves that propagate through a magnetohydro fluid, namely, the fast, Alfvén, slow, and entropy waves. Numerical schemes for ideal magnetohydrodynamics that are based on the standard finite volume (FV) discretization exhibit pseudo-convergence in which non-regular waves no longer exist only after heavy grid refinement. A method is described for obtaining solutions for coplanar and near-coplanar cases that consist of only regular waves, independent of grid refinement. The method, referred to as Compound Wave Modification (CWM), involves removing the flux associated with non-regular structures and can be used for simulations in two- and three-dimensions because it does not require explicitly tracking an Alfvén wave. For a near-coplanar case, and for grids with 2^{13} points or less, we find root-mean-square-errors (RMSEs) that are as much as 6 times smaller. For the coplanar case, in which non-regular structures will exist at all levels of grid refinement for standard FV schemes, the RMSE is as much as 25 times smaller.

A multidimensional ideal MHD code has implemented for simulations on graphics processing units (GPUs). Performance measurements were conducted for both the NVIDIA

GeForce GTX Titan and Intel Xeon E5645 processor. The GPU is shown to perform one to two orders of magnitude greater than the CPU when using a single core, and two to three times greater than when run in parallel with OpenMP. Performance comparisons are made for two methods of storing data on the GPU. The first approach stores data as an Array of Structures (AoS), e.g., a point coordinate array of size $3 \times n$ is iterated over. The second approach stores data as a Structure of Arrays (SoA), e.g. three separate arrays of size n are iterated over simultaneously. For an AoS, coalescing does not occur, reducing memory efficiency. All results are given for Cartesian grids, but the algorithms are implemented for a general geometry on a unstructured grids.

Chapter 1: Introduction

The formation of compound waves in numerical solutions of the ideal magnetohydrodynamics (MHD) equations is studied using dissipative finite volume schemes. Numerical solutions containing compound waves were encountered during the development of a finite volume (FV) flux corrected transport (FCT) solver for ideal MHD capable of running on a GPU. The FV-FCT code was used to determine the benefits and limitations of GPU parallelism. Chapter 5 contains original results on GPU efficiency. The first four chapters of this dissertation address compound wave solutions to Riemann problems of ideal MHD.

A Riemann problem is a one-dimensional initial value problem for a conservative system in which a single discontinuity separates two constant states. Riemann problems play an important role in fluid simulations; numerical algorithms in both computational fluid dynamics (CFD) and computational MHD use linear approximations of local Riemann problems for the computation of numerical fluxes [5, 28]. A Riemann problem is properly defined, and solutions for different conservative systems are discussed in Chapter 2. Solutions of Riemann problems are composed of multiple waves that emanate away from a discontinuity. Exact and approximate solutions for the Euler equations of hydrodynamics (HD) are presented. The exact solutions were obtained with a nonlinear solver for HD Euler equations, that was developed for this thesis.

The equations of ideal MHD is the final conservative system discussed in Chapter 2. The ideal MHD equations are more complex than the Euler equations of hydrodynamics. As a result, the number of possible structures is greater. In addition, the system of equations is non-strictly hyperbolic, which makes non-regular structures such as intermediate shocks and compound waves possible.

A solution is only considered physical if it satisfies entropy and evolutionary conditions [21]. The entropy is p_g/ρ^γ , where p_g is the gas pressure, ρ is the density, and γ is the ratio

of specific heats. The entropy condition states that the change in entropy across a shock is zero or larger. The evolutionary condition requires a shock to be structurally stable under small perturbations [21]. In hydrodynamics, the entropy and evolutionary conditions are equivalent.

In the past, intermediate shocks in ideal MHD have been considered unphysical because they are structurally unstable under small perturbations [22]. In recent years, their physicality has been reconsidered. Observations of heliospheric plasma and numerical simulations of bow shocks have provided evidence for their existence. Feng and Wang [17] reported that a discontinuity observed by *Voyager 2* in January 1979 was an intermediate shock. Chao et al. [7] identified an intermediate shock in *Voyager 1* measurements in 1980. Intermediate shocks have been observed in numerical simulations of bow shocks in both two- and three-dimensions [11, 12]. They were first observed in numerical simulations by Brio and Wu [5] whose results have been used extensively as a reference for numerical solutions of the ideal MHD equations. The classification systems for intermediate, and normal Lax shocks is given in Chapter 2.

Chapter 3 presents the exact and approximate solution to Riemann problems of ideal MHD. An nonlinear solver for ideal MHD non-linear Riemann solver, that is based on the method described by Dai and Woodward [9] with the rarefaction wave extension by Ryu and Jones [28], was implemented to provide the exact solution. The nonlinear solver is also used to create original benchmarks for ideal MHD model development.

Chapter 3 also discusses non-uniform convergence exhibited by dissipative FV schemes. Torrilhon [36] computed the convergence rates for various implementations of the finite volume method on one-dimensional Riemann problems with non-unique solutions. All implementations exhibited non-uniform convergence with respect to grid resolution. The schemes produced solutions that converged toward the non-regular solution until a certain level of grid refinement, at which point convergence was to the regular solution. This behavior was referred to as pseudo-convergence, and numerical diffusion was identified as the cause. For the coplanar case, in which the rotation angle is 180° , we argue that convergence to the

non-regular solution is expected to always occur, independent of grid resolution, because the transverse velocity and magnetic field are restricted to a single plane.

Because grids with more than 10^4 points are needed to obtain L^1 errors on the order of 10^{-2} , Torrhilon [36] suggested using adaptive mesh refinement (AMR) to reduce the computational costs. AMR can be a powerful computational tool but is complex to implement, and for structured grids, it introduces non-conformity.

In Chapter 4, we present an alternative method for error reduction, Compound Wave Modification (CWM), that requires modifying the flux from the finite volume approximation. The modification is done to the Harden-Lax-van Leer-Discontinuities (HLLD) [24] approximate Riemann solver implemented in the *Athena* MHD code [32, 30]. The CWM solutions are compared with one-dimensional exact solutions for a near-coplanar case and the coplanar case. Chapter 4 is almost entirely original work. In Chapter 5, the focus of the dissertation shifts to high performance computing with graphics processing units (GPUs).

Numerical solutions for problems in ideal MHD can be computationally expensive to obtain. Most large-scale simulations require some sort of parallelism, where data is processed simultaneously. Parallelism occurs in two ways: distributed-, and shared-memory. When parallelism is done by way of distributed-memory, the domain is partitioned geometrically and each subset is send to a separate processor where the solution is updated. The process is known as domain decomposition. After each update, the processors must communicate with one another to update the solution at the boundaries between sub-domains. This is done by assigning one processor as the *master* that handles communication. After each update of the solution, the processors exchange information with the master to ensure the boundaries of each sub-domain are updated appropriately.

Shared memory parallelism refers to simultaneous computation on a single processing unit, either CPU or GPU. The standard approach is to invoke multiple threads on the CPU, each thread performing the same computations and updating the solution independently. Shared memory parallelism does not suffer the overhead costs of communication between processor, but great must be taken to ensure that two or more threads do not attempt

to access the same portion of memory simultaneously. This issue is known as memory contention and it introduces errors into the computation. The GPU offers an alternative option to the CPU for a shared memory device. The GPU is capable of exceeding the computational power of a CPU by an order of magnitude. The theoretical peak performance in floating-point operations per second (FLOPS) of the NVIDIA GeForce GTX Titan is 4500 GFLOPS for single precision, for the Xeon E5645 @ 2.4 GHz is 460 GFLOPS per sec for single precision. The computational potential of the GPU is superior to the CPU, however, in order to take advantage of this, the data must be transferred from the host (CPU) to the device (GPU) and back to the host where it can be written to the drive. We expect to see the increased performance gains from running on the GPU as the number of operations, e.g., addition, subtraction, etc., increase.

Chapter 5 studies the performance of the two parallel shared memory processors mentioned above, namely the CPU and GPU. A multidimensional fluid solver capable of solving the Euler equations of hydrodynamics and the ideal MHD equations has been written for this dissertation and is available for download at: <https://github.com/akercher/dissertation>. The Thrust [19] library has been utilized to implement shared memory parallelism. Thrust is a C++parallel template library. It supports four device backends: compute unified device architecture (CUDA), OpenMP (OMP), thread building blocks (TBB), and the standard C++device for serial runs. The CUDA backend utilizes the GPU, while the OMP and TBB backends utilize multi-core processing on the CPU. The GPU is found to outperform the CPU running one core by one to two orders of magnitude and by two to three times when OMP is enabled. Chapter 5 demonstrates efficient memory access for the GPU by considering two approaches to data storage, array of structures (AoS) and structure of arrays (SoA). The SoA approach is shown to improve performance by one and a half to two times depending on the algorithm used.

Chapter 2: Riemann problems and conservative systems

In this chapter we define a Riemann problem and show that the solution consists of one or more waves emanating from the initial discontinuity. The structure, i.e., the different waves and their properties, of the solution is introduced via linear advection and is then more thoroughly developed by solving select Riemann problems for linear and nonlinear systems. The first nonlinear system discussed is the one-dimensional Euler equations of hydrodynamics. A method for obtaining the exact solution, as well as three methods of approximating the solution are given. The classic shock tube problem of Sod [29] is numerically approximated using routines implemented in *Athena* MHD code [32, 30]. The results are compared to the exact solution, obtained with a solver implemented for this dissertation. The final system discussed in this chapter is ideal MHD. An exact nonlinear solver and an approximate solver for the equations of ideal MHD are described.

2.1 Formulation

A Riemann problem is a type of initial value problem (IVP) for a conservation law. The initial conditions for a Riemann problem consist of two constant states separated by a discontinuity. The initial state, shown in Figure 2.1, is defined as

$$\mathbf{U}_0 = \begin{cases} \mathbf{U}_l & \text{if } x < x_d, \\ \mathbf{U}_r & \text{if } x > x_d, \end{cases} \quad (2.1)$$

where \mathbf{U}_l is the initial left state, \mathbf{U}_r is the initial right state, and x_d is the location of the discontinuity.

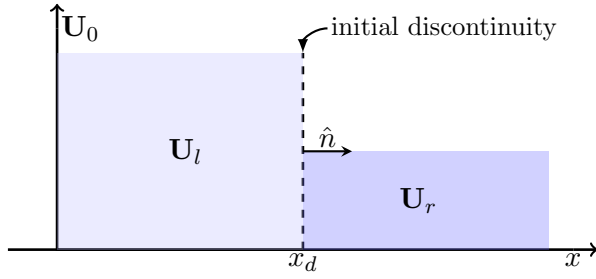


Figure 2.1: Initial conditions for a one-dimensional Riemann problem. The initial discontinuity at, x_d , separates two constant states, \mathbf{U}_l and \mathbf{U}_r .

Conservation laws are a system of partial differential equations of the form

$$\frac{\partial \mathbf{U}}{\partial t} + \frac{\partial \mathbf{F}}{\partial \mathbf{x}} = \mathbf{0},$$

where \mathbf{U} is a vector of the conservative state variables and \mathbf{F} is a vector of fluxes [33].

2.2 Linear advection

The one-dimensional linear advection equation is

$$\frac{\partial u}{\partial t} + a \frac{\partial u}{\partial x} = 0, \quad (2.2)$$

where u is the conserved variable, and a is the constant wave velocity. The solution to the Riemann problem for linear advection with $a > 0$, initial conditions given by Equation 2.2, and $x_d = 0$ is

$$u = \begin{cases} u_l & \text{if } x < at, \\ u_r & \text{if } x > at. \end{cases}$$

In the x - t plane, the solution changes from the initial left state, u_l , to the initial right

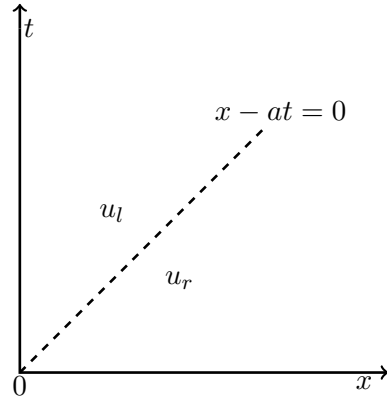


Figure 2.2: Solution to the Riemann problem for linear advection in the x - t plane. The position of the discontinuity is given by the dashed line.

state, u_r , across the characteristic line $x - at = 0$. Across the discontinuity the solution is given by the Rankine-Hugoniot jump conditions, which express the transition as conservation across the discontinuity:

$$\mathbf{F}_r - \mathbf{F}_l = S_i(\mathbf{U}_r - \mathbf{U}_l), \quad (2.3)$$

where S_i is the speed of a discontinuity connecting two states \mathbf{U}_l and \mathbf{U}_r . For the linear advection equation, the jump conditions are

$$au_r - au_l = S(u_r - u_l),$$

which gives the wave speed $S = a$. This is the speed defined by the characteristic, $x - at = 0$.

2.3 Linear systems

Consider the hyperbolic system of n linear equations

$$\frac{\partial \mathbf{U}}{\partial t} + \mathbf{A} \frac{\partial \mathbf{U}}{\partial x} = 0, \quad (2.4)$$

where \mathbf{A} is an $n \times n$ constant coefficient matrix. If \mathbf{A} has n real eigenvalues, $\lambda_1, \dots, \lambda_n$, and a corresponding set of n linearly independent right eigenvectors, $\mathbf{r}^1, \dots, \mathbf{r}^n$, the system is called hyperbolic. It is called strictly hyperbolic system if the eigenvalues are distinct. The hyperbolicity of the systems allows for it to be written in terms of the characteristic variables, that are the components of $\mathbf{W} = \mathbf{l}^i \mathbf{U}$, where \mathbf{l}^i is the matrix of left eigenvectors, see [33]. In characteristic form, the system is

$$\frac{\partial \mathbf{W}}{\partial t} + \mathbf{\Lambda} \frac{\partial \mathbf{W}}{\partial x} = 0, \quad (2.5)$$

where $\mathbf{\Lambda}$ is a diagonal matrix and i -th entry of the main diagonal is λ_i . The system has been transformed to n scalar equations of the form

$$\frac{\partial w_i}{\partial t} + \lambda_i \frac{\partial w_i}{\partial x} = 0, \quad (2.6)$$

where the eigenvalues are the characteristic speeds. The system is assumed to be strictly hyperbolic so that eigenvalues are arranged such that $\lambda_1 < \dots < \lambda_i < \dots < \lambda_n$. The solution to each scalar equation is given in terms of the characteristic variables by the solution to a linear advection problem with $a = \lambda_i$.

The solution in the x - t plane, for the linear system is shown in Figure 2.3. It is composed of n waves, each one corresponding to a characteristic speed, propagating away from the initial discontinuity. Only the state on one side of the wave is needed to determine the change across it because the speed of a linear wave is independent of the discontinuous quantity. The speed of the wave is calculated by the quantities in the known state. A rotational discontinuity is an example of a linear wave in plasma physics. It travels with a velocity equal to the Alfvén velocity, $B_n/\sqrt{4\pi\rho}$, where B_n is the magnitude of the normal component of the magnetic field, and ρ is the density. Across a rotational discontinuity, B_n , and ρ are unchanged, and determine the speed, and the jump conditions are then used to compute the connected state. In this way, every state, connected through multiple waves can be determined. The complete solution is then given by the superposition of the n waves.

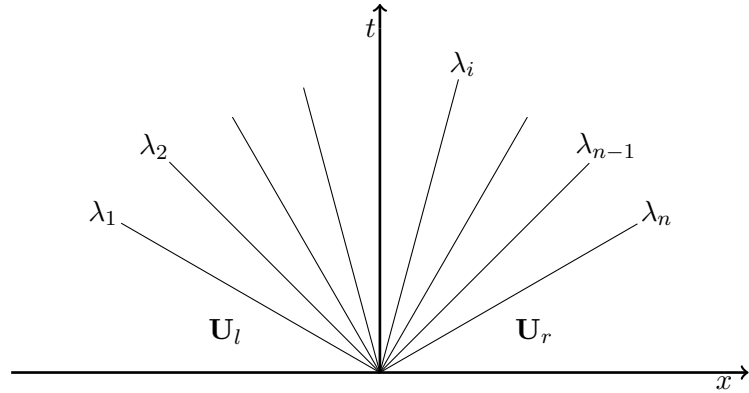


Figure 2.3: Solution to the Riemann problem for a hyperbolic system of n linear equations in the x - t plane.

The difference in characteristic variables across each wave is given by $\alpha_i = \mathbf{l}_i \cdot (\mathbf{U}_l - \mathbf{U}_r)$, and the solution in terms of conservative variables is

$$\mathbf{U} = \mathbf{U}_l + \sum_{i=1}^m \alpha_i \mathbf{r}^i, \quad \text{or} \quad \mathbf{U} = \mathbf{U}_r - \sum_{i=m+1}^n \alpha_i \mathbf{r}^i,$$

for $\lambda_m < x/t < \lambda_{m+1}$. As described next section, the states on both sides of a nonlinear wave are needed to determine the speed. As such, only local knowledge of the solution is available at a nonlinear discontinuity.

2.4 Nonlinear systems

The results from the previous sections are now extended to nonlinear hyperbolic systems of the form

$$\frac{\partial \mathbf{U}}{\partial t} + \frac{\partial \mathbf{F}}{\partial x} = 0, \tag{2.7}$$

where \mathbf{U} is a vector of conserved variables and $\mathbf{F}(\mathbf{U})$ is the flux vector. The system is called hyperbolic if the Jacobian matrix, $\mathbf{J}(\mathbf{U}) = \partial\mathbf{F}/\partial\mathbf{U}$, has n real eigenvalues and a corresponding set of n linearly independent right eigenvectors. Again the The system is also assumed to be strictly-hyperbolic so that the eigenvalues can be considered ordered based on speed. For each of the n eigenvalues there is an associated wave with speed S_i . As with the linear system, the n waves partition the solution into $n + 1$ states. Each wave in the linear system travels at a constant speed, λ_i , and has an associated jump discontinuity. In the nonlinear systems, the wave speeds are functions of the conservative variables and the structure of the wave is not always a jump discontinuity.

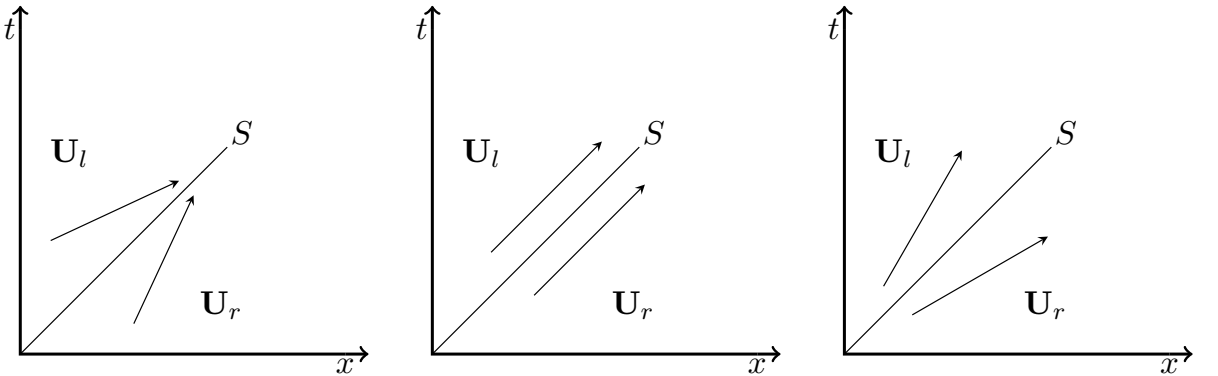


Figure 2.4: (left) Characteristics on both sides of a shock, (center) linear discontinuity, and (right) rarefaction (right).

The formation of compression and expansion waves is an distinguishing feature of non-linear systems. Shock waves are compressive discontinuities that connect two states. The characteristics of the two states connected by shock wave converge in the $x-t$ planeas shown in the left panel of Figure 2.4.. The Rankine-Hugoniot jump conditions for a shock wave are given by Equation 2.3.

Expansion shocks are possible solutions, however, they violate the entropy condition and are disregarded as unphysical. The entropy is defined, p_g/ρ^γ , where p_g is the gas pressure, ρ is the density, and γ is the ratio of specific heats. The entropy condition states that the

entropy cannot decrease across a shock.

Rarefactions are another nonlinear wave. They connect two states through a smooth transition. Unlike shocks, they are an expansion wave, and the characteristics of two states connected by rarefaction wave diverge in the $x-t$ plane, as shown in the right panel of Figure 2.4.

We adopt the following conventions when discussing to the structure of the solution to Riemann problems. For a wave propagating with speed S , connecting two constant states, the upstream state, \mathbf{U}_u , is the pre-shock state, i.e., the state of the flow that has not crossed the shock. The downstream state, \mathbf{U}_d , is the post-shock state, i.e., the state of the flow that has crossed the shock. For the right-going wave shown in Figure 2.1, \mathbf{U}_l the upstream state, and \mathbf{U}_r is the downstream state. The difference across a discontinuity is denoted with square brackets, e.g., $[\mathbf{U}] = \mathbf{U}_d - \mathbf{U}_u$.

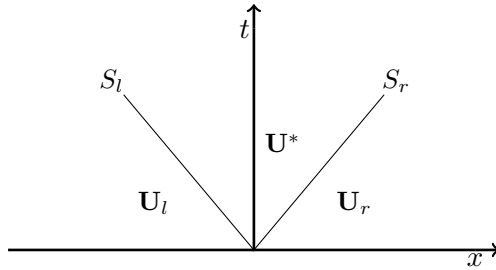


Figure 2.5: Solution to a Riemann with one intermediate state in the $x-t$ plane.

When the solution to a Riemann problem is composed of more than one wave, the state between two waves is called an intermediate state, and is denoted \mathbf{U}^* . If the solution includes more than two waves, then the intermediate states are referenced in relation to the left-most and right-most state. If $n + 1$ states compose the solution, the states downstream

of \mathbf{U}_j are denoted \mathbf{U}_{ij}^* , where $i = 1, \dots, m/2$, $j = l, r$, and

$$m = \begin{cases} n & \text{if } n \text{ is even,} \\ n + 1 & \text{if } n \text{ is odd.} \end{cases}$$

If n is even, then the middle state is written without a subscript.

2.5 Compressible hydrodynamics

The Euler equations of compressible hydrodynamics comprise a nonlinear hyperbolic system of conservation laws. The structure of the solution for Riemann problems of compressible hydrodynamics is presented below. If viscosity and thermal conductivity are neglected, then the Euler equations describe the evolution of a compressible ideal gas. The equations form a strictly-hyperbolic system that admit shocks, rarefactions, and linear discontinuities. The conservative form of the Euler equations is

$$\frac{\partial \rho}{\partial t} + \nabla \cdot (\rho \mathbf{v}) = 0 , \quad (2.8)$$

$$\frac{\partial(\rho \mathbf{v})}{\partial t} + \nabla \cdot [\rho \mathbf{v} \otimes \mathbf{v} + p_g] = 0 , \quad (2.9)$$

$$\frac{\partial E}{\partial t} + \nabla \cdot [(E + p_g) \mathbf{v}] = 0 , \quad (2.10)$$

where the energy density is defined as

$$E = \frac{p_g}{\gamma - 1} + \frac{\rho v^2}{2} , \quad (2.11)$$

$v^2 = v_n^2 + \mathbf{v}_t^2$, and the gas constant γ is the ratio of specific heats. The one-dimensional quasi-linear form of the Euler equations is

$$\frac{\partial \mathbf{U}}{\partial t} + \mathbf{A}(\mathbf{U}) \frac{\partial \mathbf{U}}{\partial x} = 0. \quad (2.12)$$

The Jacobian of $\mathbf{A}(\mathbf{U})$ must have three real and distinct eigenvalues and a set of three linearly independent right eigenvectors because the system is strictly-hyperbolic. If the eigenvalues are arranged such that $\lambda_1 < \lambda_2 < \lambda_3$, then λ_1 and λ_3 correspond to nonlinear waves, and λ_2 is a linear wave. The nonlinear waves can be either a shock (i.e., discontinuous wave) or rarefaction (i.e. smooth wave). The linear wave is contact discontinuity (CD) that carries a single jump in density and satisfies the jump conditions given by Equation 2.3. The three eigenvalues and their associated waves are:

$$\lambda_3 = v_n + a : \text{rarefaction or shock},$$

$$\lambda_2 = v_n : \text{contact discontinuity, and}$$

$$\lambda_1 = v_n - a : \text{rarefaction or shock},$$

where $a = \sqrt{\gamma p_g / \rho}$ is the speed of sound.

A possible structure of the self-similar solution $\mathbf{U}(x, t)$ to the Euler equations is shown in Figure 2.6. Three waves: a fast shock, a contact discontinuity, and a slow rarefaction, separate the four constant states: the initial left, left intermediate, right intermediate, and initial right. The state, $\mathbf{U}_{l\text{fan}}^*$, inside the rarefaction wave is not constant. It connects the states \mathbf{U}_l and \mathbf{U}_l^* through a smooth transition. The characteristic speed at the head of a rarefaction wave is $v_{nu} \pm a_u$. At the tail of a rarefaction wave, the characteristic speed is $v_{nd} \pm a_d$. The plus (minus) sign refers to right-going (left-going) waves. The speed of the contact discontinuity is given by the characteristic speed λ_2 . The shock speeds are derived from the Rankine-Hugoniot jump conditions, Equation 2.3. The speeds of a right-going

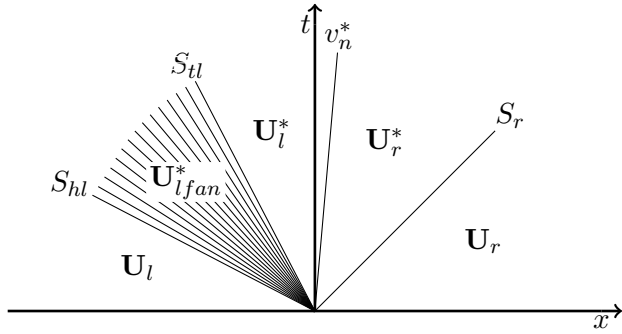


Figure 2.6: Possible structure of the solution to a Riemann problem for the Euler equations in the x - t plane. The solution consists of a rarefaction wave to the left of contact discontinuity, and a shock wave to the right.

shock, S_r , and left-going shock, S_l , are

$$S_r = v_{nr} + a_r \sqrt{\left(\frac{\gamma+1}{2\gamma}\right) \left(\frac{p_g^*}{p_{gr}}\right) + \left(\frac{\gamma-1}{2\gamma}\right)},$$

$$S_l = v_{nl} - a_l \sqrt{\left(\frac{\gamma+1}{2\gamma}\right) \left(\frac{p_g^*}{p_{gl}}\right) + \left(\frac{\gamma-1}{2\gamma}\right)},$$

where $p_g^* = p_{gl}^* = p_{gr}^*$, since the gas pressure is unchanged across a contact discontinuity. The velocity at the head (tail) of a rarefaction wave is given by the corresponding characteristic speed in the upstream (downstream) state.

2.5.1 Exact Riemann solver

The solution to a Riemann problem consists of n waves separating $n+1$ states, and it is found by determining the speed of each wave, and the jump associated with each wave. Solving a Riemann problem for the one-dimensional Euler equations requires determining two unknown states, \mathbf{U}_l^* and \mathbf{U}_r^* , and three wave speeds. The exact solution is calculated by improving an initial guess for gas pressure in the intermediate states through an iterative

procedure, e.g., Newton's method [33]. The iteration is carried out until the jump condition for the normal velocity at the contact discontinuity, $[v_n^*] = 0$, is satisfied to the desired accuracy. In practice, this is done by finding the root of the equation

$$f(p_g^*, \mathbf{U}_l, \mathbf{U}_r) \equiv f_r(p_{gr}, \mathbf{U}_r) + f_l(p_{gl}, \mathbf{U}_l) + v_{nr} - v_{nl} = 0,$$

where f_r (f_l) is a function connecting the initial right (left) state to the intermediate right (left) state. The normal velocity in the intermediate states (Equation (4.9) of [33]) is

$$v_n^* = \frac{1}{2}(v_{nr} + v_{nl}) + \frac{1}{2}(f_r - f_l).$$

The functions f_l and f_r depend on the type of wave, i.e. shock or rarefaction. If pressure increases across the wave, $p_d^* > p_{gu}$, then the wave is a shock, otherwise, the wave is a rarefaction. The function f_j , for $j = l$ and $j = r$, (Equations (4.6) and (4.7) of [33]) is given by

$$f_j(p_{gj}, \mathbf{U}_j) = \begin{cases} (p_g^* - p_{gj}) \left[\frac{2}{\rho_j((\gamma+1)p_g^* + (\gamma-1)p_{gl})} \right]^{\frac{1}{2}} & \text{if } p_g^* > p_{gj}, \\ \frac{2a_j}{(p_g^*-1)} \left[\left(\frac{p_g^*}{p_{gj}} \right)^{\frac{\gamma-1}{2\gamma}} - 1 \right] & \text{if } p_g^* \leq p_{gj}. \end{cases}$$

where $j = l$ and $j = r$. The densities ρ_j for $j = l$ and r , in the left and right intermediate states are

$$\rho_j^* = \begin{cases} \rho_j \left[\frac{\frac{p_g^*}{p_{gj}} + \frac{\gamma-1}{\gamma+1}}{\frac{\gamma-1}{\gamma+1} \frac{p_g^*}{p_{gj}} + 1} \right] & \text{if } p_g^* > p_{gj}, \\ \rho_j \left(\frac{p_g^*}{p_{gj}} \right)^{\frac{1}{\gamma}} & \text{if } p_g^* \leq p_{gj}. \end{cases}$$

If the solution contains a rarefaction wave then the states in the fan are needed to complete the solution. The state in the rarefaction wave is

$$\rho = \rho_j \left[\frac{2}{(\gamma + 1)} \pm \frac{(\gamma - 1)}{(\gamma + 1)a_j} \left(v_{nj} - \frac{x}{t} \right) \right]^{\frac{2}{\gamma - 1}},$$

$$v_n = \frac{2}{(\gamma + 1)} \left[\frac{(\gamma - 1)}{2} v_{nj} \pm a_j + \frac{x}{t} \right],$$

$$p_g = p_{gj} \left[\frac{2}{(\gamma + 1)} \pm \frac{(\gamma - 1)}{(\gamma + 1)a_j} \left(v_{nj} - \frac{x}{t} \right) \right]^{\frac{2\gamma}{\gamma - 1}},$$

for $j = l$ and r , and the plus (minus) sign corresponds to a left-going (right-going) wave.

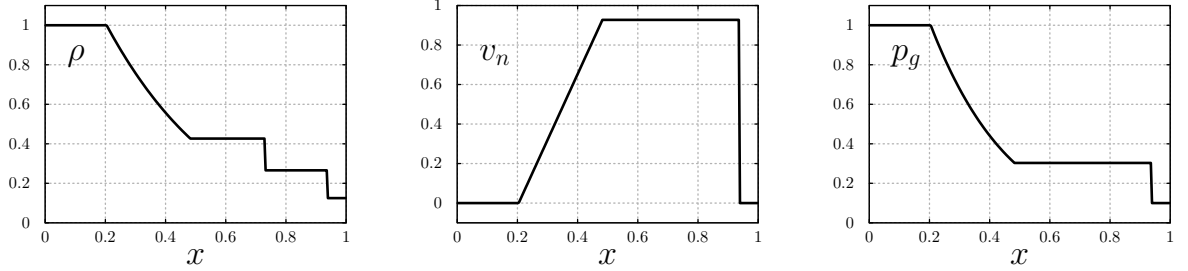


Figure 2.7: Exact solution to Sod shock tube problem. The head of the rarefaction is located at $x \approx 0.2$, and the tail is at $x \approx 0.45$. The contact discontinuity is located at $x \approx 0.72$, and the shock is located $x \approx 0.95$.

Shock tube problems in Gas Dynamics are an example of a Riemann problem for the Euler equations. They are typically used for validation and benchmarking. The problem consists two fluids are separated by a thin film at $x = 0.5$. At time $t = 0$, the film is removed and the fluids interact. The exact solution to the Sod shock tube problem at time $t = 0.25$ ([29], test 1 in [33]), is shown in Figure 2.7. The initial left state is $\mathbf{U}_l = (1.0, 0.0, 1.0)$ and the initial right state is $\mathbf{U}_r = (0.125, 0.0, 0.1)$. The problem was solved using our own

implementation of the routine *exact.f* provided in [33]. Convergence is established when

$$\frac{2|p_g^{n+1} - p_g^n|}{p_g^{n+1} + p_g^n} < 10^{-6}, \quad (2.13)$$

where p_g is the gas pressure in the intermediate states and n is the number of iterations. The solution consists of a left rarefaction, contact discontinuity, and right shock.

Convergence to the exact solution is not guaranteed since obtaining it requires Newton iteration. In flow simulations, approximate Riemann solvers maintain a similar level of accuracy as the exact solver, while reducing the computational cost since no iterations are required. Three different approximate Riemann solvers for the Euler equations are described in the following sections.

2.5.2 Approximate Riemann solvers

HLLE solver

The Harten-Lax-van Leer-Einfeldt (HLLE) [13] solver assumes a two wave solution with a single intermediate state, see Figure 2.5. The intermediate state is approximated as the integral average over the Riemann fan: $[x_l, x_r] \times [0, t]$, i.e. the region between the left and right wave in Figure 2.5. The integral form of the conservation laws are

$$\int_{x_l}^{x_r} \mathbf{U}(x, t_f) dx - \int_{x_l}^{x_r} \mathbf{U}(x, 0) dx + \int_0^t \mathbf{F}(\mathbf{U}(x_r, t')) dt' - \int_0^t \mathbf{F}(\mathbf{U}(x_l, t')) dt' = 0. \quad (2.14)$$

Applying (2.14) over $[x_l, x_r] \times [0, t]$, gives the HLLE intermediate state as

$$\mathbf{U}^* = \frac{S_r \mathbf{U}_r - S_l \mathbf{U}_l + \mathbf{F}_r + \mathbf{F}_l}{S_r - S_l}. \quad (2.15)$$

The HLLE fluxes

$$\mathbf{F}^* = \frac{S_r \mathbf{F}_l - S_l \mathbf{F}_r + S_r S_l (\mathbf{U}_l - \mathbf{U}_r)}{S_r - S_l}, \quad (2.16)$$

are found by applying (2.14) over the left ($[x_l, 0] \times [0, t]$) or right ($[0, x_r] \times [0, t]$) side of the Riemann fan, and substituting (2.15) into the result (see Appendix A). The HLLE states are defined by

$$\mathbf{U}(x, t) = \begin{cases} \mathbf{U}_l & \text{if } 0 < S_l, \\ \mathbf{U}^* & \text{if } S_l \leq 0 \leq S_r, \\ \mathbf{U}_r & \text{if } S_r < 0. \end{cases} \quad (2.17)$$

The HLLE interface fluxes are defined

$$\mathbf{F}(x, t) = \begin{cases} \mathbf{F}_l & \text{if } 0 < S_l, \\ \mathbf{F}^* & \text{if } S_l \leq 0 \leq S_r, \\ \mathbf{F}_r & \text{if } S_r < 0. \end{cases} \quad (2.18)$$

The method is very robust because it is positivity preserving, $\rho > 0$, and $p_g > 0$ [14]. However, as described in the next section, the HLLE approximate Riemann solver is diffuse because it neglects the difference in density across the contact discontinuity. The alternative approach of Toro et al. [34] restores the contact discontinuity. It is referred to as the HLLC method, where C stands for *Contact*.

HLLC solver

The approximate solution of the HLLC solver in the x - t plane is shown in Figure 2.8. The intermediate states are calculated by approximating the integral over the appropriate Riemann fan and requiring that the Rankine-Hugoniot jump conditions, $v_{nr}^* = v_{nl}^*$, $\mathbf{v}_{tr}^* = \mathbf{v}_{tl}^*$, and $p_{gr}^* = p_{gl}^*$, are satisfied across the contact discontinuity. The intermediate states are

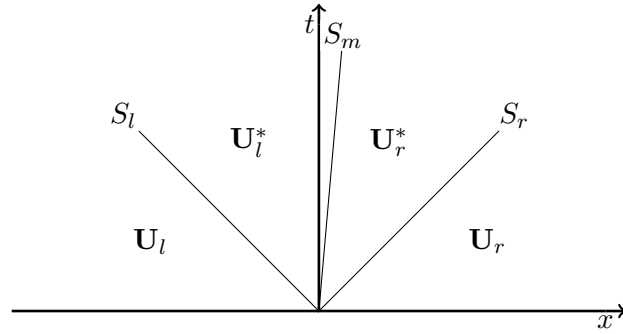


Figure 2.8: Restoration of the contact discontinuity in the HLLC approximate Riemann solver.

(Equation (10.33) of [33])

$$\mathbf{U}_j^* = \rho_j \left(\frac{S_j - v_{nj}}{S_j - v_n^*} \right) \begin{bmatrix} 1 \\ v_n \\ \mathbf{v}_{tj} \\ \frac{E_j}{\rho_j} + (S_m - v_{nj}) \left[S_m + \frac{p_{gj}}{\rho_j(S_j - v_{nj})} \right] \end{bmatrix},$$

where $j = l$ and $j = r$. The HLLC states are

$$\mathbf{U}(x, t) = \begin{cases} \mathbf{U}_l & \text{if } 0 < S_l, \\ \mathbf{U}_l^* & \text{if } S_l \leq 0 \leq S_m, \\ \mathbf{U}_r^* & \text{if } S_m \leq 0 \leq S_r, \\ \mathbf{U}_r & \text{if } S_r < 0. \end{cases} \quad (2.19)$$

The HLLC fluxes can then be derived with the procedure given in Appendix A. They are

$$\mathbf{F}(x, t) = \begin{cases} \mathbf{F}_l & \text{if } 0 < S_l, \\ \mathbf{F}_l^* = \mathbf{F}_l + S_l(\mathbf{U}_l^* - \mathbf{U}_l) & \text{if } S_l \leq 0 \leq S_m, \\ \mathbf{F}_r^* = \mathbf{F}_r + S_r(\mathbf{U}_r^* - \mathbf{U}_r) & \text{if } S_m \leq 0 \leq S_r, \\ \mathbf{F}_r & \text{if } S_r < 0. \end{cases} \quad (2.20)$$

Both the HLLE and HLLC methods depend on the approximations of the fastest (slowest) wave speed S_r (S_L). Davis [10] used wave speeds of

$$S_l = \min\{\lambda_1(\mathbf{U}_l), \lambda_1(\mathbf{U}_r)\}, \text{ and } S_r = \max\{\lambda_n(\mathbf{U}_l), \lambda_n(\mathbf{U}_r)\}, \quad (2.21)$$

where λ_1 (λ_n) is the smallest (largest) eigenvalue of (2.7). Einfeldt et al. [14] used

$$S_l = \min\{\lambda_1(\mathbf{U}_l), \lambda_1(\mathbf{U}_{\text{Roe}})\}, \text{ and } S_r = \max\{\lambda_n(\mathbf{U}_r), \lambda_n(\mathbf{U}_{\text{Roe}})\}, \quad (2.22)$$

where $\lambda_i(\mathbf{U}_{\text{Roe}})$ is an eigenvalue of the Roe matrix, see Section 2.5.2.

The middle wave speed, S_m , needs to be approximated in the HLLC solver. Batten et al. [3] argued that the middle wave speed should be determined using only (2.21) or (2.22), and the initial states. They gave the speed as

$$S_m = \frac{(S_r - v_{nr})\rho_r v_{nr} - (S_l - v_{nl})\rho_l v_{nl} - p_{gr} + p_{gl}}{(S_r - v_{nr})\rho_r - (S_l - v_{nl})\rho_l}. \quad (2.23)$$

Toro et al. [34] suggested an alternative method of determining the wave speeds by first estimating the pressure and velocity in the intermediate state according to

$$S_l = v_{nl} - a_l q_l, \quad S_m = v_n^*, \quad S_r = v_{nr} - a_r q_r, \quad (2.24)$$

where

$$q_j = \begin{cases} 1 & \text{if } p_g^* \leq p_{gj}, \\ \left[1 + \frac{\gamma+1}{2\gamma} \left(\frac{p_g^*}{p_{gj}} - 1 \right) \right]^{\frac{1}{2}} & \text{if } p_g^* > p_{gj}, \end{cases} \quad (2.25)$$

for $j = l$ and $j = r$.

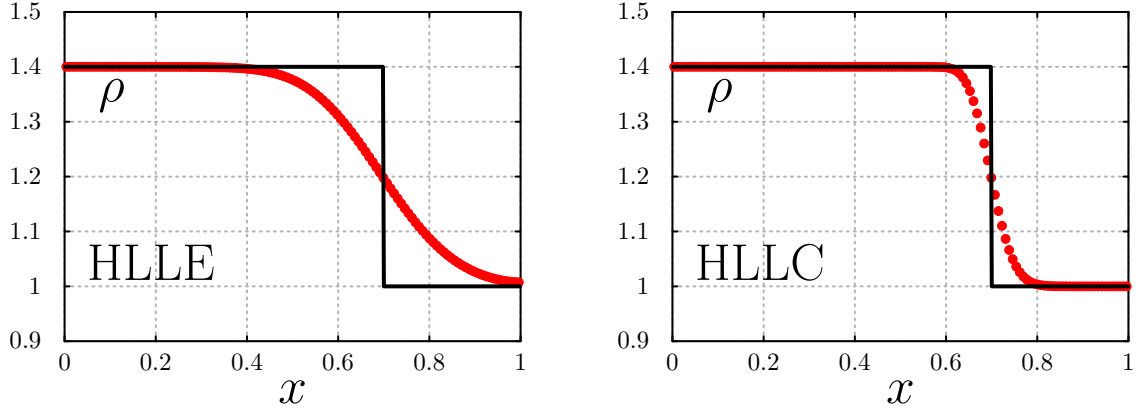


Figure 2.9: HLLE (left), and HLLC (right) approximate solutions for a slow moving contact discontinuity. Athena [30] was used to compute the approximate solutions. The exact solution was computed with code written for this dissertation: <https://github.com/akercher/dissertation>.

The two-state approximation of the HLLC method is able to resolve an isolated stationary CD exactly. In the case of a slow moving CD, the HLLC method is less diffusive than the HLLE method. This can be demonstrated by considering a Riemann problem for the Euler equations with initial conditions (test 7 of [33])

$$\begin{aligned} (\rho_l, v_{nl}, p_{gl}) &= (1.4, 0.1, 1.0), \\ (\rho_r, v_{nr}, p_{gr}) &= (1.0, 0.1, 1.0). \end{aligned} \quad (2.26)$$

The exact solution to (2.26), shown with a solid black line in Figure 2.9, consists of one CD

moving slowly to the right. The solution approximated with HLLE (HLLC) fluxes is shown with dotted red lines in the left (right) panel of Figure 2.9. The results were obtained using a uniform grid of 128 cells and the van Leer (VL) integrator of Stone and Gardiner [31]. The interface states were constructed using piece-constant (i.e. first order) interpolation. The HLLD approximate Riemann solver of Miyoshi and Kusano [24], see Section 2.6.4, is an magnetohydrodynamic extension of the HLLC solver that resolves isolated discontinuities with the same level of accuracy as the HLLC solver..

Roe solver

The Riemann solver of Roe [27] replaces the nonlinear Jacobian in (2.12), $\mathbf{A}(\mathbf{U})$, with a linear approximation, $\tilde{\mathbf{A}}(\mathbf{U}_{\text{Roe}})$, where \mathbf{U}_{Roe} is a matrix of averaged state variables. The linearized equation

$$\frac{\partial \mathbf{U}}{\partial t} + \tilde{\mathbf{A}} \frac{\partial \mathbf{U}}{\partial x} = 0. \quad (2.27)$$

of the approximated Riemann problem is then solved exactly. The linearized Jacobian is constrained to be hyperbolic, consistent with the nonlinear Jacobian of the original problem, i.e., it must equal the nonlinear Jacobian when the left and right states are equal, and it must retain conservation across discontinuities. The interface flux is built from the results of Section 2.3. It is given as

$$\mathbf{F}_{\text{Roe}} = \frac{1}{2} \left(\mathbf{F}_l + \mathbf{F}_r - \sum_{i=1}^n \tilde{\alpha}_i |\tilde{\lambda}_i| \tilde{\mathbf{r}}^i \right), \quad (2.28)$$

where $\tilde{\alpha}_i = \tilde{\mathbf{l}} \cdot (\mathbf{U}_l - \mathbf{U}_r)$ is the wave amplitude, $\tilde{\lambda}_i$ is the wave speed, $\tilde{\mathbf{l}}$ and $\tilde{\mathbf{r}}$ are the left and right eigenvectors respectively. The so-called Roe-averaged state variables are

$$\begin{aligned}\tilde{\rho} &= \sqrt{\rho_l \rho_r}, \\ \tilde{v}_n &= \frac{\sqrt{\rho_l} v_{nl} + \sqrt{\rho_r} v_{nr}}{\sqrt{\rho_l} + \sqrt{\rho_r}}, \\ \tilde{\mathbf{v}}_t &= \frac{\sqrt{\rho_l} \mathbf{v}_{tl} + \sqrt{\rho_r} \mathbf{v}_{tr}}{\sqrt{\rho_l} + \sqrt{\rho_r}}, \\ \tilde{H} &= \frac{\sqrt{\rho_l} H_l + \sqrt{\rho_r} H_r}{\sqrt{\rho_l} + \sqrt{\rho_r}}, \\ \tilde{a} &= \left[(\gamma - 1) \left(\tilde{H} - \frac{\tilde{v}^2}{2} \right) \right]^{\frac{1}{2}},\end{aligned}\tag{2.29}$$

where $\tilde{v}^2 = \tilde{v}_n^2 + \tilde{\mathbf{v}}_t^2$, and $H_j = (E_j + p_{gj})/\rho$ is the total enthalpy for $j = l$ and $j = r$. The eigenvalues of the Roe matrix are

$$\tilde{\lambda}_1 = \tilde{v}_n - \tilde{a}, \quad \tilde{\lambda}_2 = \tilde{\lambda}_3 = \tilde{\lambda}_4 = \tilde{v}_n, \quad \tilde{\lambda}_5 = \tilde{v}_n + \tilde{a}.\tag{2.30}$$

The right eigenvectors are the columns of the matrix

$$\tilde{\mathbf{R}} = \begin{bmatrix} 1 & 0 & 0 & 1 & 1 \\ \tilde{v}_n - \tilde{a} & 0 & 0 & \tilde{v}_n & \tilde{v}_n + \tilde{a} \\ \tilde{v}_{t1} & 1 & 0 & \tilde{v}_{t1} & \tilde{v}_{t1} \\ \tilde{v}_{t2} & 0 & 1 & \tilde{v}_{t2} & \tilde{v}_{t2} \\ \tilde{H} - \tilde{v}_n \tilde{a} & \tilde{v}_{t1} & \tilde{v}_{t2} & \frac{1}{2} \tilde{V}^2 & \tilde{H} + \tilde{v}_n \tilde{a} \end{bmatrix}.\tag{2.31}$$

The left eigenvectors are the rows of the matrix

$$\tilde{\mathbf{L}} = \begin{bmatrix} \left(\frac{\gamma_1}{2}\tilde{V}^2 + \tilde{v}_n\tilde{a}\right) / (2\tilde{a}^2) & -(\gamma_1\tilde{v}_n + \tilde{a}) / (2\tilde{a}^2) & -(\gamma_1\tilde{v}_{t1}) / (2\tilde{a}^2) & -(\gamma_1\tilde{v}_{t2}) / (2\tilde{a}^2) & \gamma_1 / (2\tilde{a}^2) \\ -\tilde{v}_{t1} & 0 & 1 & 0 & 0 \\ -\tilde{v}_{t2} & 0 & 0 & 1 & 0 \\ 1 - \gamma_1\tilde{V}^2 / (2\tilde{a}^2) & \gamma_1\tilde{v}_n/\tilde{a}^2 & \gamma_1\tilde{v}_{t1}/\tilde{a}^2 & \gamma_1\tilde{v}_{t2}/\tilde{a}^2 & -\gamma_1/\tilde{a}^2 \\ \left(\frac{\gamma_1}{2}\tilde{V}^2 - \tilde{v}_n\tilde{a}\right) / (2\tilde{a}^2) & -(\gamma_1\tilde{v}_n - \tilde{a}) / (2\tilde{a}^2) & -(\gamma_1\tilde{v}_{t1}) / (2\tilde{a}^2) & -(\gamma_1\tilde{v}_{t2}) / (2\tilde{a}^2) & \gamma_1 / (2\tilde{a}^2) \end{bmatrix}, \quad (2.32)$$

where $V^2 = v_n^2 + \mathbf{v}_t^2$, and $\gamma_1 = \gamma - 1$.

Sod shock tube

A common test case for the Euler equations is the shock tube problem of Sod [29]. The exact solution at time $t = 0.25$ is shown in Figure 2.7 for initial conditions

$$\begin{aligned} (\rho_l, v_{nl}, p_{gl}) &= (1.0, 0, 1.0), \\ (\rho_r, v_{nr}, p_{gr}) &= (0.125, 0, 0.1). \end{aligned} \quad (2.33)$$

The solution was approximated with the van Leer (VL) integrator of Stone and Gardiner [31] on a 128 cell grid. The interface states were constructed using piece-wise constant interpolation. The three flux schemes were used: HLLE, HLLC, and Roe. The results, shown in Figure 2.10, indicate that all three schemes produce similar results, with the HLLE solver being more diffuse than the HLLC or Roe solver. The Roe solver requires eigenvalue decomposition, which increases computation costs. This makes the HLLC solver a better choice for most simulations. These properties carry over to the MHD extensions of each of the schemes, and as such, influenced our choose of incorporating the new compound wave correction, see Chapter 4, into the HLLD solver instead of a Roe solver.

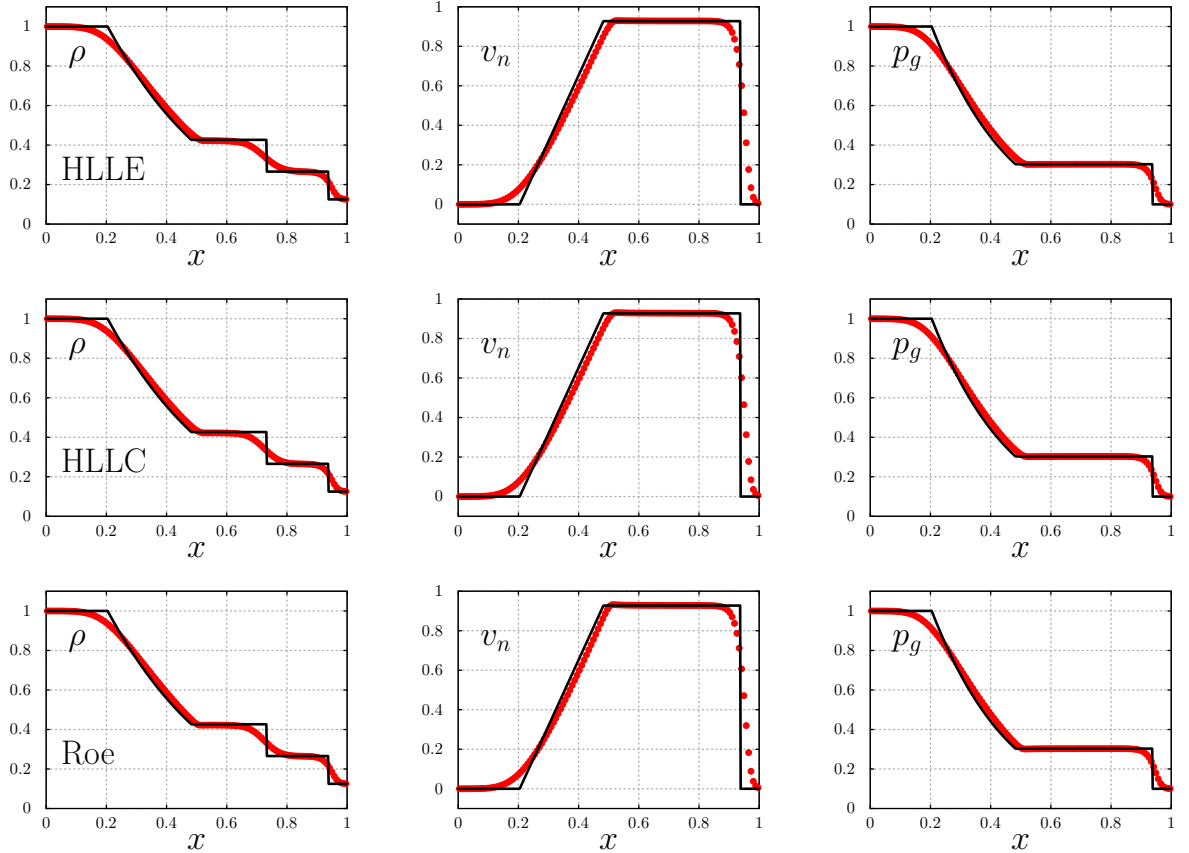


Figure 2.10: HLLE (Top row), HLLC (middle row), and Roe (bottom row) approximate solution to Sod shock tube problem computed using first-order piece-wise constant interpolation. Athena [30] was used to compute the approximate solutions. The exact solution was computed with code written for this dissertation available at: <https://github.com/akercher/dissertation>.

2.6 Ideal magnetohydrodynamics

The ideal MHD equations are an approximate description of the interaction between plasma flowing in a region with a magnetic field. They consist of the Euler equations of hydrodynamics and the magnetic induction equation, $\frac{\partial \mathbf{B}}{\partial t} = \nabla \times (\mathbf{v} \times \mathbf{B}) + \eta \nabla^2 \mathbf{B}$, for which the divergence-free condition $\nabla \cdot \mathbf{B} = 0$ is satisfied. The effects of resistivity, thermal conductivity, and viscosity are neglected. The equations are

$$\frac{\partial \rho}{\partial t} + \nabla \cdot (\rho \mathbf{v}) = 0 , \quad (2.34)$$

$$\frac{\partial(\rho \mathbf{v})}{\partial t} + \nabla \cdot \left[\rho \mathbf{v} \otimes \mathbf{v} + \left(p_g + \frac{B^2}{2} \right) \mathbf{I} - \mathbf{B} \otimes \mathbf{B} \right] = 0 , \quad (2.35)$$

$$\frac{\partial E}{\partial t} + \nabla \cdot \left[\left(E + p_g + \frac{B^2}{2} \right) \mathbf{v} - \mathbf{v} \cdot \mathbf{B} \otimes \mathbf{B} \right] = 0 , \text{ and} \quad (2.36)$$

$$\frac{\partial \mathbf{B}}{\partial t} + \nabla \cdot [\mathbf{v} \otimes \mathbf{B} - \mathbf{B} \otimes \mathbf{v}] = 0 , \quad (2.37)$$

where the energy density is defined as

$$E = \frac{p_g}{\gamma - 1} + \frac{\rho v^2}{2} + \frac{B^2}{2} , \quad (2.38)$$

the gas constant γ is the ratio of specific heats, and B is the magnitude of the magnetic field. The units are chosen so that the speed of light c and constant 4π do not appear in the equations.

In one dimension, with flow variation in the x -direction, the ideal MHD equations can be written in the form of a conservation law

$$\frac{\partial \mathbf{U}}{\partial t} + \frac{\partial \mathbf{F}}{\partial x} = \mathbf{0} ,$$

where the conservative state variables \mathbf{U} and their respective fluxes \mathbf{F} are

$$\mathbf{U} = \begin{bmatrix} \rho \\ \rho v_n \\ \rho \mathbf{v}_t \\ E \\ \mathbf{B}_t \end{bmatrix}, \quad \mathbf{F} = \begin{bmatrix} \rho v_n \\ \rho v_n^2 + p_g + B^2/2 - B_n^2 \\ \rho v_n \mathbf{v}_t - B_n \mathbf{B}_t \\ (E + p_g + B^2/2)v_n - (\mathbf{v} \cdot \mathbf{B})B_n \\ v_n \mathbf{B}_t - B_n \mathbf{v}_t \end{bmatrix},$$

and a normal (x) component is denoted with the subscript n and tangential components are denoted with the subscript t . The normal component of the magnetic field is treated as a parameter because it must be constant in order to satisfy the divergence-free condition of \mathbf{B} , which is $\partial B_n / \partial x = 0$ in one dimension.

2.6.1 Waves in ideal magnetohydrodynamics

The Jacobian matrix, $\mathbf{J}(\mathbf{U}) = \partial \mathbf{F} / \partial \mathbf{U}$, has real but not necessarily distinct eigenvalues in ideal MHD. The ideal MHD system is called non strictly hyperbolic because it can have degenerate eigenvalues. Each eigenvalue is associated with a wave that travels at the characteristic speed

v_n : contact or tangential discontinuity (entropy),

$v_n \pm c_s$: slow rarefaction or shock,

$v_n \pm c_a$: rotational discontinuity (Alfvén), and

$v_n \pm c_f$: fast rarefaction or shock,

where c_s , c_a , c_f are the slow, Alfvén, and fast wave propagation speeds, respectively. The sign in each equation indicates the direction of propagation. The propagation speeds are

$$c_{f,s}^2 = \frac{1}{2} \left[a^2 + c_a^2 + c_t^2 \pm \sqrt{(a^2 + c_a^2 + c_t^2)^2 - 4a^2 c_a^2} \right] \text{ and } c_a^2 = \frac{B_n^2}{\rho} ,$$

where $c_t^2 = B_t^2/\rho$, $a^2 = \gamma p_g/\rho$, c_a (c_t) is the Alfvén speed normal (tangential) to the wave front, and a is the speed of sound. The plus (minus) sign corresponds to the fast (slow) propagation speed.

2.6.2 Shock classification

In ideal MHD, a contact discontinuity (CD) has a discontinuous jump in density that occurs where the normal component of the magnetic field is nonzero and the velocity, gas pressure, and tangential components of the magnetic field are continuous. The heliopause and magnetopause are two astrophysical boundaries where plasma flows are separated by a density discontinuity. If the normal component of the magnetic field is zero, the contact discontinuity is referred to as a tangential discontinuity. For a tangential discontinuity, only the normal velocity and total pressure (gas plus magnetic pressure) are continuous [20].

Shocks are typed by comparing the pre-shock and post-shock velocities with the characteristic velocities in the respective states. Numbers are assigned to the state according to the inequalities $4 < c_s < 3 < c_a < 2 < c_f < 1$. If $|v_n| > c_f$, a state is referred to as superfast and denoted 1; if $|v_n| = c_f$, it is referred to as fast and denoted 1, 2; if $|v_n| < c_f$ it is referred to as subfast and denoted 2. When $|v_n| = c_a$, it is referred to as an Alfvén shock and denoted 2, 3. The shock is referred to as superslow (3) if $|v_n| > c_s$, slow (3, 4) if $|v_n| = c_s$, and subslow (4) if $|v_n| < c_s$. Finally, the shock is classified as static if $|v_n| = 0$. Shocks are then classified as an $i \rightarrow j$ type where i is the upstream type and j is the downstream type.

- $1 \rightarrow 2$ fast shocks (FS) have compression and a increase in strength of the tangential magnetic field as the shock front is transversed: $B_{t1} < B_{t2}$.

- $3 \rightarrow 4$ slow shocks (SS) have compression and a decrease in strength of the tangential magnetic field as the shock front is transversed: $B_{t1} > B_{t2}$.
- $1 \rightarrow 2, 3$ (switch-on) shocks have a tangential magnetic field that is zero upstream and nonzero downstream: $B_{t1} = 0$ and $B_{t2} \neq 0$.
- $2, 3 \rightarrow 4$ (switch-off) shocks have a tangential magnetic field that is nonzero upstream and zero downstream: $B_{t1} \neq 0$ and $B_{t2} = 0$.
- $1 \rightarrow 3, 1 \rightarrow 4, 2 \rightarrow 3$ and $2 \rightarrow 4$ intermediate shocks (IS) have a change in sign of the tangential magnetic field as the shock front is transversed: $B_{t1} < 0 < B_{t2}$ or $B_{t1} > 0 > B_{t2}$.

So-called regular waves only influence the orientation of the perpendicular magnetic field or its magnitude. Fast and slow shocks alter the magnitude of the perpendicular magnetic field while rotational discontinuities alter their orientation. A rotational discontinuity (RD) propagates with a speed of c_a and rotates the perpendicular magnetic field while the magnitude of the perpendicular magnetic field is equal on both sides of the discontinuity. Expansion waves can also occur in ideal MHD. The magnitude of the tangential magnetic field will decrease across fast rarefaction (FR); across slow rarefaction (SR) it will increase.

Intermediate shocks are over-compressive shocks that alter both the magnitude and orientation of the tangential magnetic field. These shocks are classified as $1 \rightarrow 3$, $1 \rightarrow 4$, $2 \rightarrow 4$, and $2 \rightarrow 3$. The $2 \rightarrow 3$ class is called an Alfvén shock and across it the tangential magnetic field rotates by 180°. A switch-on shock ($1 \rightarrow 2, 3$) corresponds to a pre-shock tangential magnetic field of zero and a non-zero post shock tangential magnetic field. A switch-off shock ($2, 3 \rightarrow 4$) occurs when the tangential magnetic field is zero post-shock.

2.6.3 Nonlinear Riemann solver

Analytic solutions to problems of ideal MHD are generally not known. However, highly accurate, to machine precision, solutions can be generated using a nonlinear solver [9, 28, 35]. The exact solutions presented in this work were found using a nonlinear solver that is based

on the method originally developed by Dai and Woodward [9] and improved by Ryu and Jones [28] to correctly compute rarefaction waves.

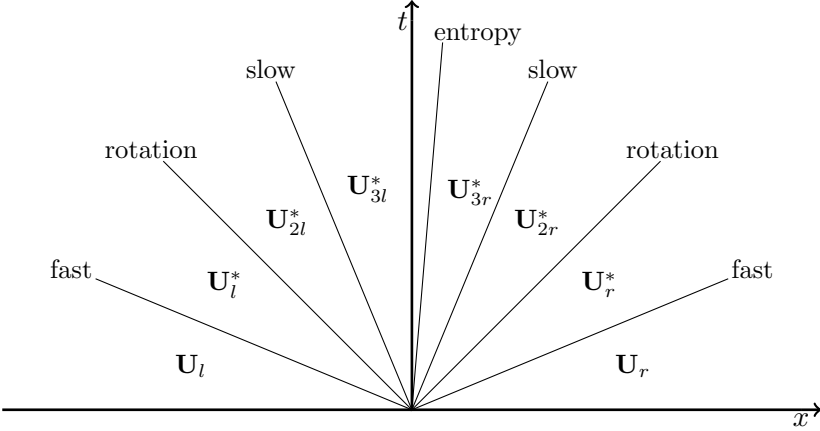


Figure 2.11: Seven possible waves and/or discontinuities separating the eight possible regions, or states of the ideal MHD Riemann problem. The initial contact discontinuity, i.e., the entropy wave, separates regions \mathbf{U}_{3l}^* and \mathbf{U}_{3r}^* .

The exact solutions are composed of eight possible MHD states separated by seven wave fronts, as depicted in Figure 2.11. The transitions from one region to another through a discontinuity is controlled by the jump conditions associated with the discontinuity. The Rankine-Hugoniot jump conditions for ideal MHD in Lagrangian mass coordinates, $dm = \rho dx$, are

$$W[V] = -[v_n], \quad (2.39)$$

$$W[v_n] = -[P - B_n^2], \quad (2.40)$$

$$W[\mathbf{v}_t] = -B_n[\mathbf{B}_t], \quad (2.41)$$

$$W[V\mathbf{B}_t] = -B_n[\mathbf{v}_t], \text{ and} \quad (2.42)$$

$$W[VE] = [v_n P] - B_n[B_n v_n + \mathbf{B}_t \cdot \mathbf{v}_t], \quad (2.43)$$

where $P = p_g + \frac{1}{2}(B_n^2 + B_t^2)$ is the total pressure and $W = -(\rho v_n)_u = -(\rho v_n)_d$ is the Lagrangian velocity of the discontinuity and $V = 1/\rho$ [9, 28]. When moving in the $-x$ direction, the velocity W is negative. Brackets are used to denote the difference between the upstream and downstream states for a quantity Q , i.e $[Q] = Q_u - Q_d$.

Dai and Woodward [9] give the fast and slow shock speeds in mass coordinates as

$$W_{f,s}^2 = \frac{1}{2(1+S_0)} \left[(C_s^2 + C_f^2 + S_1^2) \pm \sqrt{(C_s^2 + C_f^2 + S_1^2)^2 - 4(1+S_0)(C_s^2 C_f^2 - S_2)} \right], \quad (2.44)$$

where $C_f = \rho c_f$ and $C_s = \rho c_s$. The quantities S_0, S_1, S_2 are given by Ryu and Jones [28] in terms of B_t as

$$S_0 = -\frac{1}{2}(\gamma - 1) \frac{[B_t]}{B_t}, \quad (2.45)$$

$$\begin{aligned} S_1 = & \frac{1}{2} \left\{ -(\gamma - 2) V C_t^2 \frac{[B_t]}{B_t} + 2C_0^2 - (\gamma - 4) V C_t^2 \right. \\ & \left. - 2\gamma C_a^2 \right\} \frac{[B_t]}{B_t}, \text{ and} \end{aligned} \quad (2.46)$$

$$\begin{aligned} S_2 = & \frac{1}{2} \left\{ \frac{C_a^2 [B_t]^2}{V} + (\gamma + 2) C_t C_a^2 [B_t] + V C_t^2 C_a^2 (\gamma + 1) \right. \\ & \left. + (\gamma + 1) C_a^4 - 2C_0^2 C_a^2 \right\} \frac{[B_t]}{B_t}, \end{aligned} \quad (2.47)$$

where $C_0 = \rho a$ is the Lagrangian speed of sound, $C_a = \rho c_a$ is the Lagrangian Alfvén speed, and $C_t = \sqrt{\rho B_t^2}$. The quantities in equations (2.45)-(2.47) are for the state downstream of the shock.

The relationships for fast rarefactions given by Ryu and Jones [28] are

$$\frac{dC_0}{dB_t} = -\frac{\gamma+1}{2}\sqrt{\rho}\frac{C_tC_s^2}{C_0(C_s^2 - C_a^2)} = \frac{\gamma+1}{2}\sqrt{\rho}\frac{C_s^2(C_f^2 - C_a^2)}{C_a^2C_tC_0} = \frac{\gamma+1}{2}\frac{\rho}{C_0}\frac{dp_g}{dB_t}, \quad (2.48)$$

$$\frac{dv_n}{dB_t} = \mp\frac{1}{\sqrt{\rho}}\frac{C_\perp C_a^2}{C_f(C_s^2 - C_a^2)} = \pm\frac{C_f^2 - C_a^2}{\sqrt{\rho}C_tC_f} = \pm\frac{2}{\gamma+1}\frac{C_0C_a^2}{C_s^2C_f}\frac{1}{\rho}\frac{dC_0}{dB_t}, \text{ and} \quad (2.49)$$

$$\frac{1}{\cos\psi}\frac{dv_{t1}}{dB_t} = \frac{1}{\sin\psi}\frac{dv_{t2}}{dB_t} = \mp\frac{1}{\sqrt{\rho}}\frac{C_a}{C_f}, \quad (2.50)$$

where the upper and lower signs refer to right- and left-going waves, respectively. The rotation angle is defined by $\tan\psi = B_z/B_y$.

For slow rarefactions, replace the fast speed (C_f) with the slow speed (C_s) and the slow speed (C_s) with the fast speed (C_f) in Equations (2.48)-(2.50).

An initial guess for the solution in the six interior regions shown in Figure 2.11 is improved iteratively until the jump conditions of the initial contact or tangential discontinuity are satisfied to within a desired accuracy. We have found a very high rate of convergence using the intermediate states approximated using the HLLD method for the initial guess. In practice, we use a relaxation factor and apply damping to speed up convergence.

2.6.4 HLLD approximate Riemann solver

An MHD extension of the HLLC scheme for the Euler equations (see Section 2.5.2) capable of resolving all isolated linear discontinuities of ideal MHD, i.e. RDs and CDs was developed by Miyoshi and Kusano [24]. They referred to the scheme as HLLD, where the D stands for *discontinuities*. The HLLD scheme assumes a six-state solution separated by five waves as depicted in Figure 2.12. Two nonlinear waves, i.e., shocks and rarefactions, separate the left and right initial states from the intermediate states in the Riemann fan, i.e., \mathbf{U}_l^* , \mathbf{U}_{2l}^* , \mathbf{U}_{2r}^* , and \mathbf{U}_r^* . The four intermediate states are separated by two RDs with velocities, S_l^* , S_r^* , and one CD with velocity, S_m . The one-dimensional wave speeds and intermediate states of [24] have been modified for general coordinates, with $v_n = \mathbf{v} \cdot \mathbf{n}$, and $B_n = \mathbf{B} \cdot \mathbf{n}$,

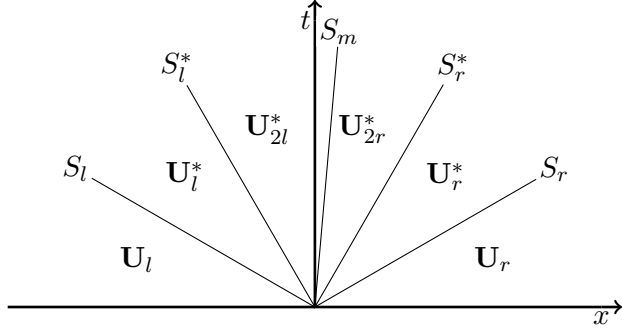


Figure 2.12: Intermediate states and waves used in the HLLD approximate Riemann solver.

where \mathbf{n} is a normal vector with unit length.

The velocity of the CD, S_m , is estimated with the HLL average given by (2.23), except gas pressure, p_g , is replaced with total pressure, p_t , and it becomes

$$S_m = \frac{(S_r - v_{nr})\rho_r v_{nr} - (S_l - v_{nl})\rho_l v_{nl} - p_{tr} + p_{tl}}{(S_r - v_{nr})\rho_r - (S_l - v_{nl})\rho_l}. \quad (2.51)$$

The intermediate states are approximated by solving the jump conditions across each wave. Since the total pressure is conserved across the linear discontinuities in ideal MHD, the total pressure is constant throughout the Riemann fan. It is given as

$$p_t^* = p_{tj}^* = p_{tj} + \rho_j(S_j - v_{nj})(S_m - v_{nj}) \quad (2.52)$$

for $j = l$ or $j = r$. Substituting (2.51) into (2.52) and averaging over the left and right states yields the explicit expression for total pressure throughout the Riemann fan:

$$p_t^* = \frac{(S_r - v_{nr})\rho_r p_{tl} - (S_l - v_{nl})\rho_l p_{tr} + \rho_r \rho_l (S_r - v_{nr})(S_l - v_{nl})(v_{nr} - v_{nl})}{(S_r - v_{nr})\rho_r - (S_l - v_{nl})\rho_l}. \quad (2.53)$$

The states downstream of the fast waves, \mathbf{U}_j^* for $j = l$ and $j = r$ of Figure 2.12, are given

in one-dimension by Eqs (41)-(47) of [24], written for general coordinates: they are

$$\rho_j^* = \rho_j \frac{S_j - v_{nj}}{S_j - S_m}, \quad (2.54)$$

$$\mathbf{v}_j^* = \mathbf{v}_j + \frac{(S_j - S_m)(p_t^* - p_{tj})\mathbf{n} - B_n \mathbf{B}_j (S_m - v_{nj})}{\rho_j(S_j - v_{nj})(S_j - S_m) - B_n^2}, \quad (2.55)$$

$$\mathbf{B}_j^* = \frac{\mathbf{B}_j (\rho_j(S_j - v_{nj})^2 - B_n^2) - B_n (p_t^* - p_{tj})\mathbf{n}}{\rho_j(S_j - v_{nj})(S_j - S_m) - B_n^2}, \quad (2.56)$$

$$E_j^* = \frac{(S_j - v_{nj})E_j - p_{tj}v_{nj} + p_t^*S_m + B_n(\mathbf{v}_j \cdot \mathbf{B}_j - \mathbf{v}_j^* \cdot \mathbf{B}_j^*)}{S_j - S_m}. \quad (2.57)$$

If $\mathbf{n} = (1, 0, 0)$, $v_x^* = S_m$, $B_x = B_n$, (2.55) and (2.56) reduce to (44)-(47) of [24], given as

$$v_{yj}^* = v_{yj} - B_x B_{yj} \frac{S_m - v_{nj}}{\rho_j(S_j - v_{nj})(S_j - S_m) - B_x^2},$$

$$v_{zj}^* = v_{zj} - B_x B_{zj} \frac{S_m - v_{nj}}{\rho_j(S_j - v_{nj})(S_j - S_m) - B_x^2},$$

$$B_{yj}^* = B_{yj} \frac{\rho_j(S_j - v_{nj})^2 - B_x^2}{\rho_j(S_j - v_{nj})(S_j - S_m) - B_x^2}, \text{ and}$$

$$B_{zj}^* = B_{zj} \frac{\rho_j(S_j - v_{nj})^2 - B_x^2}{\rho_j(S_j - v_{nj})(S_j - S_m) - B_x^2}.$$

The states downstream of the rotational discontinuity, \mathbf{U}_{2j}^* , of Figure 2.12, can be found in terms of the initial left state and \mathbf{U}_j^* . The density, normal velocity, and total pressure are

$$\rho_{2j}^* = \rho_j^*, \quad (2.58)$$

$$v_{n2j}^* = v_{nj}^*, \quad (2.59)$$

$$p_{t2j}^* = p_{tj}^*, \quad (2.60)$$

because they are constant across the rotational discontinuity. The Alfvén speeds of the left and right rotational discontinuities are

$$S_l^* = S_l - \frac{|B_n|}{\sqrt{\rho_l^*}} \text{ and } S_r^* = S_r + \frac{|B_n|}{\sqrt{\rho_r^*}}. \quad (2.61)$$

The description of the HLLD intermediate states is completed by solving for $\mathbf{v}_m^* = \mathbf{v}_{2l}^* = \mathbf{v}_{2r}^*$ and $\mathbf{B}_m^* = \mathbf{B}_{2l}^* = \mathbf{B}_{2r}^*$. This is done using the integral conversation law over the Riemann fan $(S_l\delta t, S_r\delta t) \times (0, \delta t)$ (Eq. (58) of [24]). They are given as

$$\mathbf{v}_m^* = \frac{\sqrt{\rho_l^*}v_{nl}^* + \sqrt{\rho_r^*}v_{nr}^* + (\mathbf{B}_r^* - \mathbf{B}_l^*)\text{sign}(B_n)}{\sqrt{\rho_l^*} + \sqrt{\rho_r^*}}, \quad (2.62)$$

$$\mathbf{B}_m^* = \frac{\sqrt{\rho_l^*}\mathbf{B}_r^* + \sqrt{\rho_r^*}\mathbf{B}_l^* + \sqrt{\rho_l^*\rho_r^*}(\mathbf{v}_r^* - \mathbf{v}_l^*)\text{sign}(B_n)}{\sqrt{\rho_l^*} + \sqrt{\rho_r^*}}, \text{ and} \quad (2.63)$$

$$E_{2j}^* = E_j^* \mp \sqrt{\rho_j^*}(\mathbf{v}_j^* \cdot \mathbf{B}_j^* - \mathbf{v}_{2j}^* \cdot \mathbf{B}_{2j}^*)\text{sign}(B_n), \quad (2.64)$$

where the minus (plus) sign corresponds to $j = l$ ($j = r$). The HLLD fluxes are found by applying the integral conservation laws over the left half or right half of the Riemann fan, $(S_l\delta t, 0) \times (0, \delta t)$ or $(0, S_r\delta t) \times (0, \delta t)$, see Appendix A. The fluxes are given as

$$\mathbf{F}(x, t) = \begin{cases} \mathbf{F}_l & \text{if } 0 < S_l, \\ \mathbf{F}_l^* = \mathbf{F}_l + S_l(\mathbf{U}_l^* - \mathbf{U}_l) & \text{if } S_l \leq 0 \leq S_l^*, \\ \mathbf{F}_{2l}^* = \mathbf{F}_l^* + S_l^*(\mathbf{U}_{2l}^* - \mathbf{U}_l^*) & \text{if } S_l^* \leq 0 \leq S_m, \\ \mathbf{F}_{2r}^* = \mathbf{F}_r^* + S_r^*(\mathbf{U}_{2r}^* - \mathbf{U}_r^*) & \text{if } S_m \leq 0 \leq S_r^*, \\ \mathbf{F}_r^* = \mathbf{F}_r + S_r(\mathbf{U}_r^* - \mathbf{U}_r) & \text{if } S_r^* \leq 0 \leq S_r, \\ \mathbf{F}_r & \text{if } S_r < 0. \end{cases} \quad (2.65)$$

The HLLD method is robust because it is positivity preserving and it is less computationally expensive than schemes such as Roe's that require eigenvalue decomposition. Results from MHD shock tube problems solved using the HLLD fluxes are given in Sections 3.3-3.6. However, scheme produces compound waves for coplanar and near coplanar cases as demonstrated in Sections 3.3-3.6, an issue all approximate Riemann solvers suffer from. In Chapter 4, a modification to the HLLD fluxes that removes compound waves from the solution to coplanar and near coplanar Riemann problems of ideal is described.

Chapter 3: Numerical solutions for Ideal magnetohydrodynamics

Riemann problems and the different waves that compose the solution were described in Chapter 2. The linear and nonlinear waves emitted by the equations of ideal MHD were described. The linear waves are: the entropy wave that carries a CD and the Alfvén wave that carries an RD. The nonlinear waves are: shocks and rarefactions.

This chapter applies the ideas developed in Chapter 2 and numerically solves Riemann problems of ideal MHD. The finite volume discretization and Godunov's method for computing interface fluxes and the structure of the solution to the non-planar case are then described. The jumps in ρ and \mathbf{B}_t associated with each wave of the non-planar case is discussed. Then the nonlinear solver developed for this dissertation is described. The exact and approximate solution of non-planar and coplanar test cases are given to demonstrate the accuracy of the solvers. The nonlinear solver is then used to provide new benchmarks that can be used for the development of ideal MHD codes.

We show a limitation of FV schemes for ideal MHD, which is the appearance of non-regular waves. The physicality of these waves has been debated. We confirm the appearance of non-regular waves in terms of Riemann problems with non-unique solutions. Non-uniqueness is shown to occur when the initial transverse magnetic fields are coplanar, i.e. anti-parallel. For initial conditions near those that produce a non-unique solution, convergence is shown to be nonuniform consistent with [36]. Initially, convergence is to the solution containing a non-regular wave; after heavy grid refinement, convergence is to the solution containing only regular waves. In Chapter 4, we propose a new modification to the HLLD flux that converges to the solution containing regular waves at all grid resolutions.

3.1 Finite volume discretization and Godunov's method

For the cell-centered FV discretization, the state is defined by the integral average of the cell, given as

$$\mathbf{U}_{\text{cell}} = \frac{1}{V_{\text{cell}}} \int_{\Omega} \mathbf{U} d\Omega, \quad (3.1)$$

where V_{cell} is the volume of the cell. The volume integral of the fluxes can be rewritten using the divergence theorem as

$$\int_{\Omega} \nabla \cdot \mathbf{F} d\Omega = \int_{\Gamma} \mathbf{F} \cdot \mathbf{n} d\Gamma, \quad (3.2)$$

where \mathbf{n} is the unit normal vector. Integration in time, from $t = n$ to $t = n + 1$, gives the FV discretization as

$$\mathbf{U}_{\text{cell}}^{n+1} = \mathbf{U}_{\text{cell}}^n - \frac{\delta t}{V_{\text{cell}}} \sum_{\text{faces}} \mathbf{F} \cdot \mathbf{s}, \quad (3.3)$$

where $\mathbf{F} = \frac{1}{\delta t} \int_{\delta t} \mathbf{F} dt$ is the time averaged fluxes, $\mathbf{s} = A\mathbf{n}$ is the scaled face normal, and A is the face area. The one-dimensional FV discretization for a cell center at i is

$$\mathbf{U}_i^{n+1} = \mathbf{U}_i^n - \frac{\delta t}{\delta x} \left(\mathbf{F}_{i+1/2}^n - \mathbf{F}_{i-1/2}^n \right), \quad (3.4)$$

where $\delta x = x_{i+1} - x_i$. The timestep δt must satisfy Courant-Friedrichs-Lowy (CLF) stability condition that a wave cannot transverse more than one cell per timestep. An estimation for the timestep is given by

$$\delta t = C_r \delta x / \lambda_{\max}, \quad (3.5)$$

where $C_r \leq 1$ is the Courant number. In explicit schemes, $C_r \leq 1$ is typically required.

The flux can be evaluated in a variety of ways. The Rusanov flux, given as

$$\mathbf{F}_{i+1/2} = \frac{1}{2} \left(\mathbf{F}(\mathbf{U}_{i+1}) + \mathbf{F}(\mathbf{U}_i) - |\lambda_{\max}| (\mathbf{U}_{i+1} - \mathbf{U}_i) \right) \quad (3.6)$$

where λ_{\max} is the maximum wave speed, is a stable and efficient method for flux evaluation. It simplifies Roe's method by substituting $|\lambda_{\max}| = \max\{|\lambda_k|\}$, where k corresponds to the characteristics of the solution, because the wave speed can then be factored out the last term on the right hand side of (2.28). The summation reduces to $\mathbf{U}_{i+1} - \mathbf{U}_i$, since $\mathbf{l}_k \cdot \mathbf{r}^l = \delta_{k,l}$ where $\delta_{k,l}$ is the Kronecker delta. The Rusanov flux produces a more diffuse solution than Roe's flux, especially at linear discontinuities where the maximum wave speed is greater than the characteristic speed of the wave. As discussed in Section 3.2, the properties of the Rusanov flux are desirable for a low-order scheme when used in conjunction with FCT.

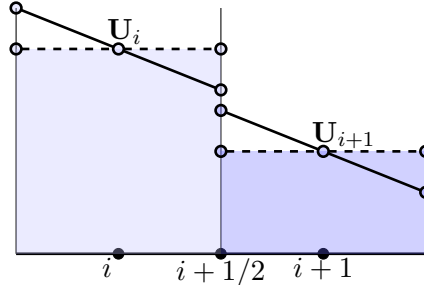


Figure 3.1: Piecewise constant (dotted line) and piecewise linear (solid line) reconstruction of interface states that define the local Riemann problem for Godunov's method.

Godunov's method uses the solution to a local Riemann problem at cell interfaces to calculate the time-averaged fluxes. The local Riemann problem is defined by reconstructing the states of neighboring cells at the interface between the cells. The reconstruction process using piecewise constant and piecewise linear interpolation is shown in Figure 3.1. Slope limiters, see Section 3.2, are used during reconstruction to ensure new extrema are not created. If the flow is not smooth, such as across a shock or discontinuity, the reconstructed

states will not be equal, and a local Riemann problem at the interface is defined. The approximate solution of to the local Riemann problem is used to calculate the time-averaged fluxes. For the Euler equations, one of the schemes described in Section 2.5.2 can be used to approximate the fluxes. For ideal MHD, the fluxes can be approximated with the HLLD scheme described in Section 2.6.4.

3.2 Higher-order extensions

In this section, two high-order extensions to first-order monotonicity preserving schemes are described. In Section 3.3 one-dimensional Riemann problems are solved using both higher order extension. The first higher order extension is implemented in *Athena*. It is a total variation diminishing (TVD) scheme, and uses the third order accurate piece-wise parabolic method (PPM) [8] for reconstruction of the interface states. The second is an FCT scheme, that was implemented for this dissertation available at: <https://github.com/akercher/dissertation>.

TVD schemes preserve monotonicity by limiting the flux of a high-order scheme or with slope limiters during interface reconstruction. To demonstrate this property, we outline the algorithm for second-order linear reconstruction of the primitive variable $\mathbf{W}_i = (\rho, v_x, v_y, v_z, p_g, B_x, B_y, B_z)$ as implemented in *Athena* [32]. The reconstruction is done in terms of characteristic variables, \mathbf{a} , and projected onto the primitive variables. The differences in primitive variables are first projected to the characteristic variables

$$\begin{aligned} \delta\mathbf{a}_l &= \sum \mathbf{l}_j \cdot (\mathbf{W}_i - \mathbf{W}_{i-1}), \\ \delta\mathbf{a}_c &= \sum \mathbf{l}_j \cdot (\mathbf{W}_{i+1} - \mathbf{W}_{i-1}), \\ \delta\mathbf{a}_r &= \sum \mathbf{l}_j \cdot (\mathbf{W}_{i+1} - \mathbf{W}_i) \end{aligned} \tag{3.7}$$

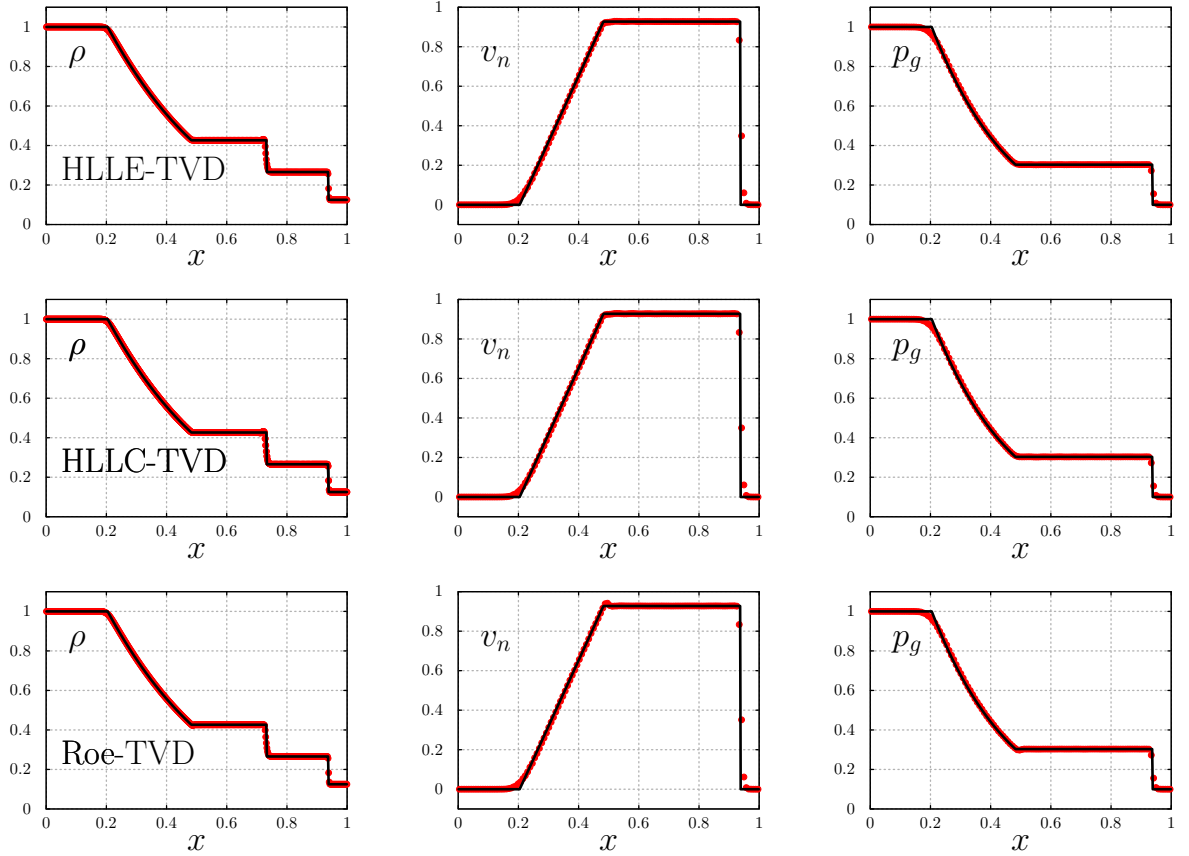


Figure 3.2: (Top row) HLLE, (middle row) HLLC, and (bottom row) Roe approximate solution to Sod shock tube problem computed using third-order parabolic interpolation. Athena [30] was used to compute the approximate solutions. The exact solution was computed with code written for this dissertation available at: <https://github.com/akercher/dissertation>.

where \mathbf{l}_j are left eigenvectors computed with the primitive variable at cell i . The monotonicity constraints are then applied, ensuring the reconstructed states are TVD:

$$\delta\mathbf{a} = \text{sign}(\delta\mathbf{a}_c) \min(2|\delta\mathbf{a}_l|, 2|\delta\mathbf{a}_r|, |\delta\mathbf{a}_c|). \quad (3.8)$$

The characteristic variables are then projected back to the primitive variables

$$\delta\mathbf{W} = \sum \delta\mathbf{a} \cdot \mathbf{r}_j, \quad (3.9)$$

where where \mathbf{r}_j are right eigenvectors computed with the primitive variables at cell i . Interpolation to the left and right face is performed to reconstruct the interface states,

$$\mathbf{w}_{i-1/2} = \mathbf{W}_i - \left(\frac{1}{2} - \min(\lambda_{\min}, 0) \frac{\delta t}{2\delta x} \right) \delta\mathbf{W}_i, \quad (3.10)$$

$$\mathbf{w}_{i+1/2} = \mathbf{W}_i + \left(\frac{1}{2} - \max(\lambda_{\max}, 0) \frac{\delta t}{2\delta x} \right) \delta\mathbf{W}_i, \quad (3.11)$$

where λ_{\min} , and λ_{\max} are the minimum and maximum eigenvalue computed at cell i . Finally, the influence of a wave that has not reached the face at the half timestep is removed from the reconstructed value

$$\mathbf{w}_{i-1/2} = \mathbf{w}_{i-1/2} + \frac{\delta t}{2\delta x} \sum_{\lambda_j < 0} ((\lambda_{\min} - \lambda_j) \mathbf{l}_j \cdot \delta\mathbf{W}_i) \mathbf{r}^j, \quad (3.12)$$

$$\mathbf{w}_{i+1/2} = \mathbf{w}_{i+1/2} + \frac{\delta t}{2\delta x} \sum_{\lambda_j > 0} ((\lambda_{\max} - \lambda_j) \mathbf{l}_j \cdot \delta\mathbf{W}_i) \mathbf{r}^j, \quad (3.13)$$

where the sums include waves that propagate towards the face. The HLL solvers use weighted averages of the flux in the left and right interfaces, and as such, a correction must be added to (3.12) and (3.13) for waves that propagate away from the interface. The

correction is [8]

$$\Delta \mathbf{w}_{i-1/2} = -\frac{\delta t}{2\delta x} \sum_{\lambda_j > 0} ((\lambda_j - \lambda_{\min}) \mathbf{l}_j \cdot \delta \mathbf{W}_i) \mathbf{r}^j, \quad (3.14)$$

$$\Delta \mathbf{w}_{i+1/2} = -\frac{\delta t}{2\delta x} \sum_{\lambda_j < 0} ((\lambda_j - \lambda_{\max}) \mathbf{l}_j \cdot \delta \mathbf{W}_i) \mathbf{r}^j. \quad (3.15)$$

The Sod shock tube test of Section 2.5.2 using higher order reconstruction is shown in Figure 3.2. The higher order extension is less diffuse than the low order counterparts shown in Figure 2.10. The contact discontinuity and shock are much better resolved.

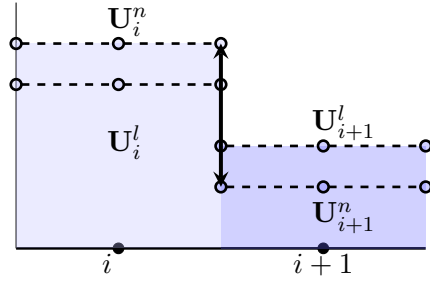


Figure 3.3: The allowable range for the high order solution is defined such that monotonicity is preserved.

The TVD scheme presented above preserves monotonicity by limiting the slope used for interface reconstruction. With FCT, the high order fluxes are limited in order to preserve monotonicity. Advancing the state variables in time with a low order scheme that preserves monotonicity is the first step in applying FCT. The time-advanced low order solution is denoted as \mathbf{U}^{td} , where td stands for transported and diffused. The antidiffusive flux is defined as the difference between the high and low order fluxes, $\mathbf{A}_{i+1/2} = \mathbf{F}_{i+1/2}^h - \mathbf{F}_{i+1/2}^l$. For the Rusanov flux, the antidiffusive flux is the second term on the right hand side of (3.6), $\mathbf{A}_{i+1/2} = \frac{1}{2}|\lambda_{\max}|(\mathbf{U}_{i+1} - \mathbf{U}_i)$. Upper and lower limiting bounds are chosen at each interface such that \mathbf{U}^{td} lies between them. The allowable range of the high-order solution

is shown in Figure 3.3. In this work, at the interface between i and $i + 1$, the limiter is chosen as

$$\mathbf{U}_{i+1/2}^{\max} = \max(\mathbf{U}_{i+1}, \mathbf{U}_i, \mathbf{U}_{i+1}^{td}, \mathbf{U}_i^{td}), \quad (3.16)$$

$$\mathbf{U}_{i+1/2}^{\min} = \min(\mathbf{U}_{i+1}, \mathbf{U}_i, \mathbf{U}_{i+1}^{td}, \mathbf{U}_i^{td}), \quad (3.17)$$

that is, the minimum and maximum values on the solution at the previous step and the low order solution. The maximum and minimum at each cell are

$$\mathbf{U}_i^{\max} = \max(\mathbf{U}_{i+1/2}^{\max}, \mathbf{U}_{i-1/2}^{\max}), \quad (3.18)$$

$$\mathbf{U}_i^{\min} = \min(\mathbf{U}_{i+1/2}^{\min}, \mathbf{U}_{i-1/2}^{\min}). \quad (3.19)$$

The positive and negative contributions of the antidiffusive fluxes are separated and limited.

For the upper bounds

$$\mathbf{P}_i^+ = \max(\mathbf{A}_{i-1/2}, 0) - \min(\mathbf{A}_{i+1/2}, 0), \quad (3.20)$$

$$\mathbf{Q}_i^+ = \mathbf{U}_i^{\max} - \mathbf{U}_i^{td}, \quad (3.21)$$

$$\mathbf{R}_i^+ = \min(1, \mathbf{Q}_i^+ / \mathbf{P}_i^+), \text{ for } \mathbf{P}_i^+ > 0, \text{ and } 0, \text{ otherwise..} \quad (3.22)$$

For the lower bounds

$$\mathbf{P}_i^- = \max(\mathbf{A}_{i+1/2}, 0) - \min(\mathbf{A}_{i-1/2}, 0), \quad (3.23)$$

$$\mathbf{Q}_i^- = \mathbf{U}_i^{td} - \mathbf{U}_i^{\min}, \quad (3.24)$$

$$\mathbf{R}_i^- = \min(1, \mathbf{Q}_i^- / \mathbf{P}_i^-), \text{ for } \mathbf{P}_i^- > 0, \text{ and } 0 \text{ otherwise.} \quad (3.25)$$

The coefficient for limiting the antidiiffusive fluxes is

$$\mathbf{C}_{i+1/2} = \min(\mathbf{R}_{i+1}^-, \mathbf{R}_i^-, \mathbf{R}_{i+1}^+, \mathbf{R}_i^+). \quad (3.26)$$

The fluxes are synchronized by taking the minimum between the coefficients of energy and density, i.e., $C_{i+1/2} = \min(\mathbf{C}_{i+1/2}(\rho), \mathbf{C}_{i+1/2}(E))$. The high order solution is then given by

$$\mathbf{U}_i^{n+1} = \mathbf{U}_i^{td} - \frac{\delta t}{\delta x} \left(C_{i+1/2} \mathbf{A}_{i+1/2}^n - C_{i-1/2} \mathbf{A}_{i-1/2}^n \right). \quad (3.27)$$

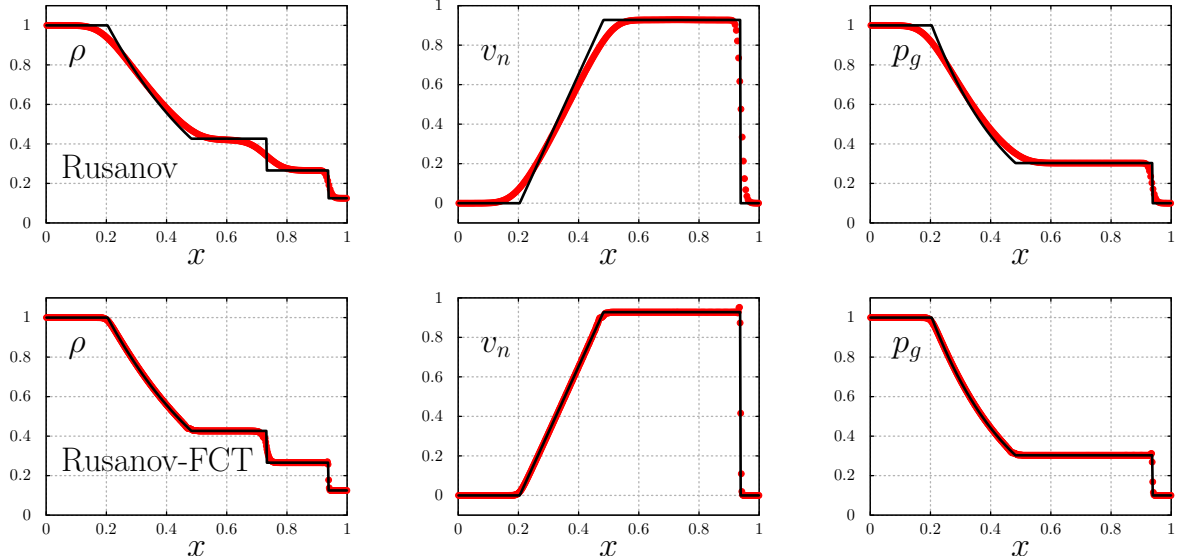


Figure 3.4: (Top row) Rusanov without FCT , and (bottom row) with FCT, approximate solutions to Sod shock tube problem on a grid of 512 points. Solutions computed with code written for this dissertation available at: <https://github.com/akercher/dissertation>.

The low order solution and high order extension using FCT for the Sod shock tube problem is shown in Figure 3.4. The low order solution is excessively diffuse, especially at the CD. FCT produces a much less diffuse solution, resolving shocks in two or three cells.

In Section 3.3 the high order extensions are used to approximate the solutions to Riemann problems of ideal MHD. For ideal MHD, the Rusanov flux is replaced by the HLLD

flux as the low order scheme in the FCT algorithm.

3.3 Riemann problems of ideal magnetohydrodynamics

The initial state of one-dimensional Riemann problems of ideal MHD are of the form

$$\begin{aligned}\mathbf{U}_l &= (\rho_l, v_{nl}, \mathbf{v}_{tl}, p_{gl}, \mathbf{B}_{tl}), \\ \mathbf{U}_r &= (\rho_r, v_{nr}, \mathbf{v}_{tr}, p_{gr}, \mathbf{B}_{tr}),\end{aligned}\tag{3.28}$$

where B_n is a parameter, $\mathbf{B}_t = (B_t \cos \psi, B_t \sin \psi)$, ψ is the rotation angle, defined by $\tan \psi = B_z/B_y$. The problem is called planar if the tangential components are parallel, i.e. $\psi_l = \psi_r$, and it is called coplanar if the tangential magnetic fields are anti-parallel, i.e. $\psi_r = \psi_l + n\pi$ for $\{n \in \mathbb{Z}^+ \text{ and } n \text{ odd}\}$. If the magnetic fields do not lie in the same plane then the problem is called non-planar. The initial configuration of the magnetic field of a non-planar problem is shown in Figure 3.5. The twist angle $\alpha = \psi_r - \psi_l$ gives the total change in orientation of the transverse magnetic field produced by the two rotational discontinuities.

As time evolves, the waves associated with each characteristic separate and distinct regions with constant states can be identified. This is shown in Figure 3.6, for the ρ and \mathbf{B}_t solutions of the non-planar Riemann problem (3.28). The evolution of \mathbf{B}_t across the regular waves of the solution is shown in Figure 3.7. The left-going fast wave is a rarefaction, across which, ρ and \mathbf{B}_t decrease. The right-going fast wave is a shock, across which both ρ and B_t increase. The rotation angle, ψ , is modified across each rotational discontinuities to produce downstream tangential magnetic fields with the same orientation. Both ρ , and B_t remain unchanged across the rotational discontinuities. The left-going slow wave is a rarefaction, across which, ρ and B_t decrease. The right-going slow wave is a shock, across which, both ρ and B_t increase. Between the states downstream of the left- and right-going slow waves, only a discontinuity in ρ is present at the location of the CD. The CD separates

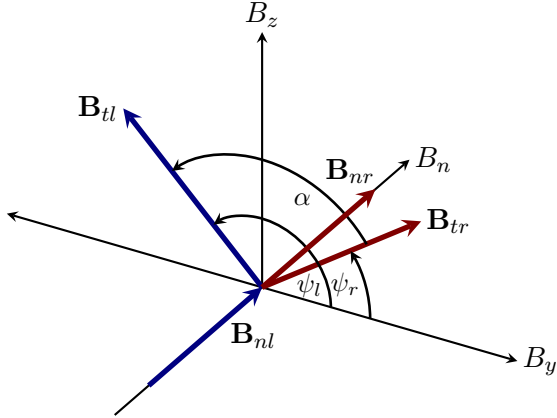


Figure 3.5: Initial configuration of magnetic field on both sides of the discontinuity. The initial twist angle $\alpha = \psi_r - \psi_l$ is the difference in rotation angles of the left and right tangential field.

intermediate states \mathbf{U}_{3l}^* and \mathbf{U}_{3r}^* of Figure 2.11. The CD is also known as the entropy wave, because it carries a jump in entropy.

3.4 Numerical tests

In this section we solve test cases that do and do not exhibit the uniqueness problem, in which more than one solution exists. Solutions to the first four test cases are comprised of only regular waves. The last two test cases involve compound waves. A slow compound wave (SCW) is present in test 5, a fast compound wave (FCW) is present in test 6, and two fast compound waves are present in Test 7. Unless otherwise stated, the domain is $x \in [0, 1]$ and the initial discontinuity is located at $x = 0.5$. In Chapter 4, tests 5, 6, and 7 are solved using a new modified flux method, and we show that only regular waves are present.

The results of several ideal MHD shock tube problems are given below. The exact solution was calculated with the nonlinear solver developed for this thesis and described in Section 2.6.3. Three different approximation methods were used: a low order base scheme, a higher order TVD scheme, and a higher order FCT scheme. All three schemes use a cell

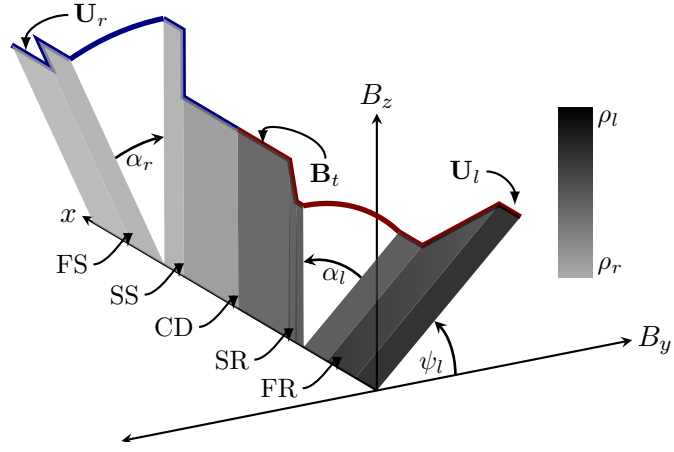


Figure 3.6: The density and tangential magnetic field of the solution to a Riemann problem of ideal MHD. All rotations are about the x-axis. In the reference frame of the CD, the direction of each wave w.r.t. the x-axis is positive for those under the solid blue line, and negative for those under the solid red line.

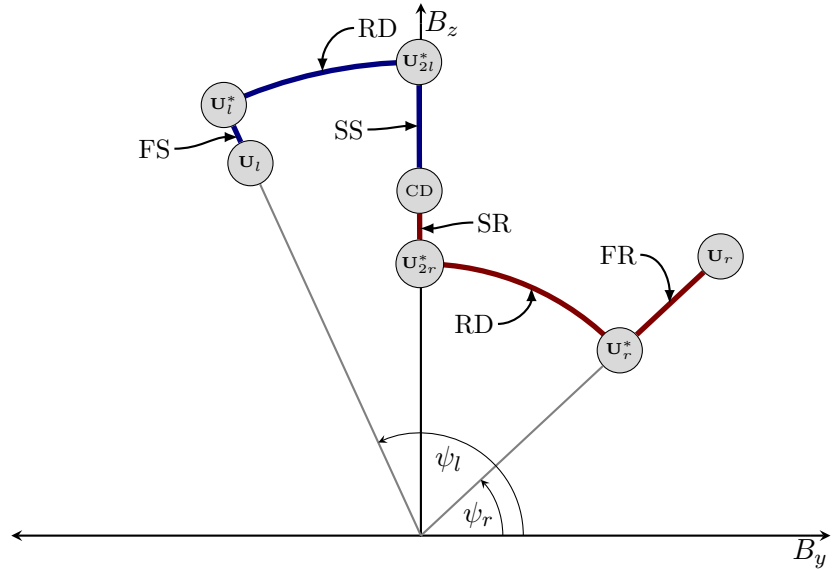


Figure 3.7: A view in the positive x-direction of Figure 3.6. The influence of regular waves on the tangential magnetic field for a non-planar Riemann problem of ideal MHD. The orientation of the tangential magnetic field is given by the angle $\psi = \tan B_z / B_y$. Regular waves only influence the magnitude or orientation of the tangential magnetic field. The intermediate states are defined in Figure 2.11, with $\mathbf{B}_{t3l}^* = \mathbf{B}_{t3r}^*$ denoted by the CD.

centered finite volume discretization and HLLD to approximate the interface flux. The base scheme, which was implemented for this dissertation, uses piece-constant interpolation for interface reconstruction and a two-stage Runge-Kutta time integration. The TVD extension to the base scheme is implemented in *Athena*. Interfaces are reconstructed with PPM, and the corner transport upwind (CTU) plus constrained transport (CT) integrator is used to advance the solution in time. The FCT extension to the base scheme was also implemented for this dissertation. The algorithms of the base scheme and the FCT extention are implemented for general geometries, but structured grids were used for comparison with *Athena*. Unless otherwise stated, the following values are used throughout the calculations, the gas constant $\gamma = 5/3$, the Courant number $C_r = 0.8$, and relaxation factor $r_k = 0.5$.

The initial conditions of the first shock tube test are

$$\begin{aligned} (\rho_l, v_{nl}, \mathbf{v}_{tl}, p_{gl}, \mathbf{B}_{tl}) &= \left(1.08, 1.2, (0.01, 0.5), 0.95, (3.6, 2.0) / \sqrt{4\pi} \right), \\ (\rho_r, v_{nr}, \mathbf{v}_{tr}, p_{gr}, \mathbf{B}_{tr}) &= \left(1.0, 0.0, (0.0, 0.0), 1.0, (4.0, 2.0) / \sqrt{4\pi} \right). \end{aligned} \quad (3.29)$$

The solution with $B_n = 2/\sqrt{4\pi}$ and $\gamma = 5/3$ is given in Table 3.1, and is shown in Figure 3.8 at time $t_f = 0.2$. From left to right, the waves of the solution are: FS, RD SS, CD, SS, RD, and FS. The solution can be compared with Table 2a of [28], and Table 1a of [9]. The nonlinear solver displays quadratic convergence, as shown in Table 3.2, where the residual, as well as the fast and slow waves speeds are listed for a sequence of iterations. The wave speeds are consistent with the result given in Table 1b of [9].

The second shock tube test for ideal MHD has initial conditions

$$\begin{aligned} (\rho_l, v_{nl}, \mathbf{v}_{tl}, p_{gl}, \mathbf{B}_{tl}) &= (3.0, 0.0, (0.0, 0.0), 3.0, (\cos \alpha_l, \sin \alpha_l)), \\ (\rho_r, v_{nr}, \mathbf{v}_{tr}, p_{gr}, \mathbf{B}_{tr}) &= (1.0, 0.0, (0.0, 0.0), 1.0, (\cos \alpha_r, \sin \alpha_r)), \end{aligned} \quad (3.30)$$

where $\alpha_l = 2.0$, $\alpha_r = 1.0$, $B_n = 3/2$, and $\gamma = 5/3$. The solution is given in Table 3.3, and is shown in Figure 3.9 at time $t_f = 0.2$. From left to right the waves of the solution are: FR,

RD SR, CD, SS, RD, and FS. The residual, as well as the fast and slow waves speeds, are listed for a sequence of iterations in Table 3.4.

The third test problem involves states of high density and low pressure. The initial conditions are

$$\begin{aligned} (\rho_l, v_{nl}, \mathbf{v}_{tl}, p_{gl}, \mathbf{B}_{tl}) &= (10.0.0, 0.0, (1.0, 0.0), 0.2, (2.0, 2.0)) , \\ (\rho_r, v_{nr}, \mathbf{v}_{tr}, p_{gr}, \mathbf{B}_{tr}) &= (5.0, 0.0, (-1.0, -0.5), 0.2, 2.0(\cos(\pi/4), \sin(\pi/4))) , \end{aligned} \quad (3.31)$$

where $B_n = 2.0$, and $\gamma = 5/3$. The solution is given in Table 3.5, and is shown in Figure 3.10 at time $t_f = 0.3$. From left to right, the waves of the solution are: FR, RD SS, CD, SS, and FR. The residual, as well as the fast and slow waves speeds are listed for a sequence of iterations in Table 3.6. The contact discontinuity speed is stationary. No scheme was able to accurately capture the transition across the CD. HLLD-TVD is the most accurate to the left of the CD, but like the other schemes, produces significant error to the right of the CD. The velocities of the left- and right-going slow shocks are -0.1013 and 0.1433 respectively. The error is caused by the fact that the waves have not had enough time to separate.

The forth test retains the initial conditions of test 3, except the densities are reduced by an order of magnitude, the magnetic field components are reduced by one half, and $v_{yr} = -1.0$. The initial conditions are

$$\begin{aligned} (\rho_l, v_{nl}, \mathbf{v}_{tl}, p_{gl}, \mathbf{B}_{tl}) &= (1.0.0, 0.0, (1.0, 0.0), 0.5, (1.0, 0.0)) , \\ (\rho_r, v_{nr}, \mathbf{v}_{tr}, p_{gr}, \mathbf{B}_{tr}) &= (0.5, 0.0, (-1.0, -0.5), 0.5, (\cos(\pi/4), \sin(\pi/4))) , \end{aligned} \quad (3.32)$$

where $B_n = 1$, and $\gamma = 5/3$. The solution is given in Table 3.7, and is shown in Figure 3.11 at time $t_f = 0.2$. The same waves that comprise the solution to test 3 are also comprise the solution of this test. From left to right, the waves of the solution are: FR, RD SS, CD, SS, and FR. Unlike test 3, there is no noticeable difference between the exact and approximate solutions in the states directly upstream and downstream of the contact discontinuity. The

residual, as well as the fast and slow waves speeds are listed for a sequence of iterations in Table 3.8. As in test 3, the contact discontinuity is stationary, but the waves have separated enough to avoid the error observed in test 3.

The final three tests demonstrate non-uniqueness of solutions to certain Riemann problems of ideal MHD. For test 5 and 6, we consider two cases: one coplanar and one near coplanar. For the coplanar case, the initial perpendicular magnetic field is anti-parallel, i.e., $\alpha = \pi$. For the near coplanar case, the twist angle is reduced so that the initial tangential magnetic fields do not lie in the same plane. In the near coplanar case, we set $\alpha = 3.0..$. Test 7 is a non-planar problem. The solution includes a left-going RD that rotates the tangential magnetic field by 2.95 radians. Riemann problems of ideal MHD with non-unique solutions are discussed in greater detail next section where the problem of non-uniform convergence is described. In Section 3.5, the problems related to non-uniqueness are overcome with a new modification to the flux calculation.

Test 5 involves a SCW comprised of a intermediate shock and fast rarefaction. It was originally considered by Torrilhon [36]. The conversion between the parameters used below and those used in [36] is given by (3.36). The initial conditions are

$$\begin{aligned} (\rho_l, v_{nl}, \mathbf{v}_{tl}, p_{gl}, \mathbf{B}_{tl}) &= (1.0.0, 0.0, (0.0, 0.0), 0.5, (0.7746, 0.0)), \\ (\rho_r, v_{nr}, \mathbf{v}_{tr}, p_{gr}, \mathbf{B}_{tr}) &= (0.2, 0.0, (0.0, 0.0), 0.12, 0.7746(\cos \alpha, \sin \alpha)), \end{aligned} \tag{3.33}$$

where $B_n = 0.7746$, and $\gamma = 5/3$, and $\alpha = 3.0, \pi$. In this test, the initial discontinuity is located at $x = 0.4$ for comparison with the results in [36]. Only the exact values of ρ and B_y are given in [36]. We give the complete solution so that it can be used as a benchmark. The exact solution for $\alpha = \pi$ (3.0) is listed in Table 3.9 (3.11), and is shown in Figure 3.12 (3.13) at time $t_f = 0.20656$. For both the coplanar and near coplanar cases, the structure of the approximate solution from left to right is: FR, SCW, CD, SS, FR. An RD and SS are found in the exact solution instead of a slow compound wave. For the near coplanar case, two rotational discontinuities are present. The residual, as well as the fast and slow waves

speeds are listed for a sequence of iterations is listed in Table 3.10 (3.12), for $\alpha = \pi$ (3.0).

Test 6 involves a FCW comprised of a fast rarefaction and intermediate shock. The initial conditions are

$$\begin{aligned} (\rho_l, v_{nl}, \mathbf{v}_{tl}, p_{gl}, \mathbf{B}_{tl}) &= (1.0.0, 0.0, (0.0, 0.0), 0.5, (1.0, 0.0)), \\ (\rho_r, v_{nr}, \mathbf{v}_{tr}, p_{gr}, \mathbf{B}_{tr}) &= (0.2, 0.0, (0.0, 0.0), 0.12, (\cos \alpha, \sin \alpha)), \end{aligned} \quad (3.34)$$

where $B_n = 1.25$, $\gamma = 5/3$, and $\alpha = 3.0, \pi$. The exact solution for $\alpha = \pi$ (3.0) is listed in Table 3.13 (3.15), and is shown in Figure 3.14 (3.15) at time $t_f = 0.15$. For both the coplanar and near coplanar cases, the structure of the approximate solution from left to right is: FCW SS, CD, SS, FR. A FR and RD is found in the exact solution instead of a fast compound wave. For the near coplanar case, two rotational discontinuities are present. The residual, as well as the fast and slow waves speeds are listed for a sequence of iterations is listed in Table 3.14 (3.16), for $\alpha = \pi$ (3.0).

Test 7 is the final test given in this section. It involves a left-going and right-going FCW. The initial conditions are

$$\begin{aligned} (\rho_l, v_{nl}, \mathbf{v}_{tl}, p_{gl}, \mathbf{B}_{tl}) &= (1.0.0, 0.0, (5.0, 0.0), 0.6, (3.25, 0.0)), \\ (\rho_r, v_{nr}, \mathbf{v}_{tr}, p_{gr}, \mathbf{B}_{tr}) &= (0.5, 0.0, (-5.0, -2.5), 0.3, 3.25(\cos \alpha, \sin \alpha)), \end{aligned} \quad (3.35)$$

where $B_n = 3.25$, $\gamma = 5/3$, and $\alpha = \pi/4$. The exact solution is listed in Table 3.17, and is shown in Figure 3.16 at time $t_f = 0.05$. From left to right is: FCW SS, CD, SS, FCW. An RD and SS are found in the exact solution instead of a fast compound wave. The left-going RD rotates the transverse magnetic field by 2.9442 radians, and the right-going RD rotates the transverse magnetic field by 2.1588 rad. The residual, as well as the fast and slow waves speeds are listed for a sequence of iterations is listed in Table 3.18. The CD is not accurately captured due to the lack of separation between the waves.

Further analysis has been performed for the coplanar case of tests 5 and 6 in order

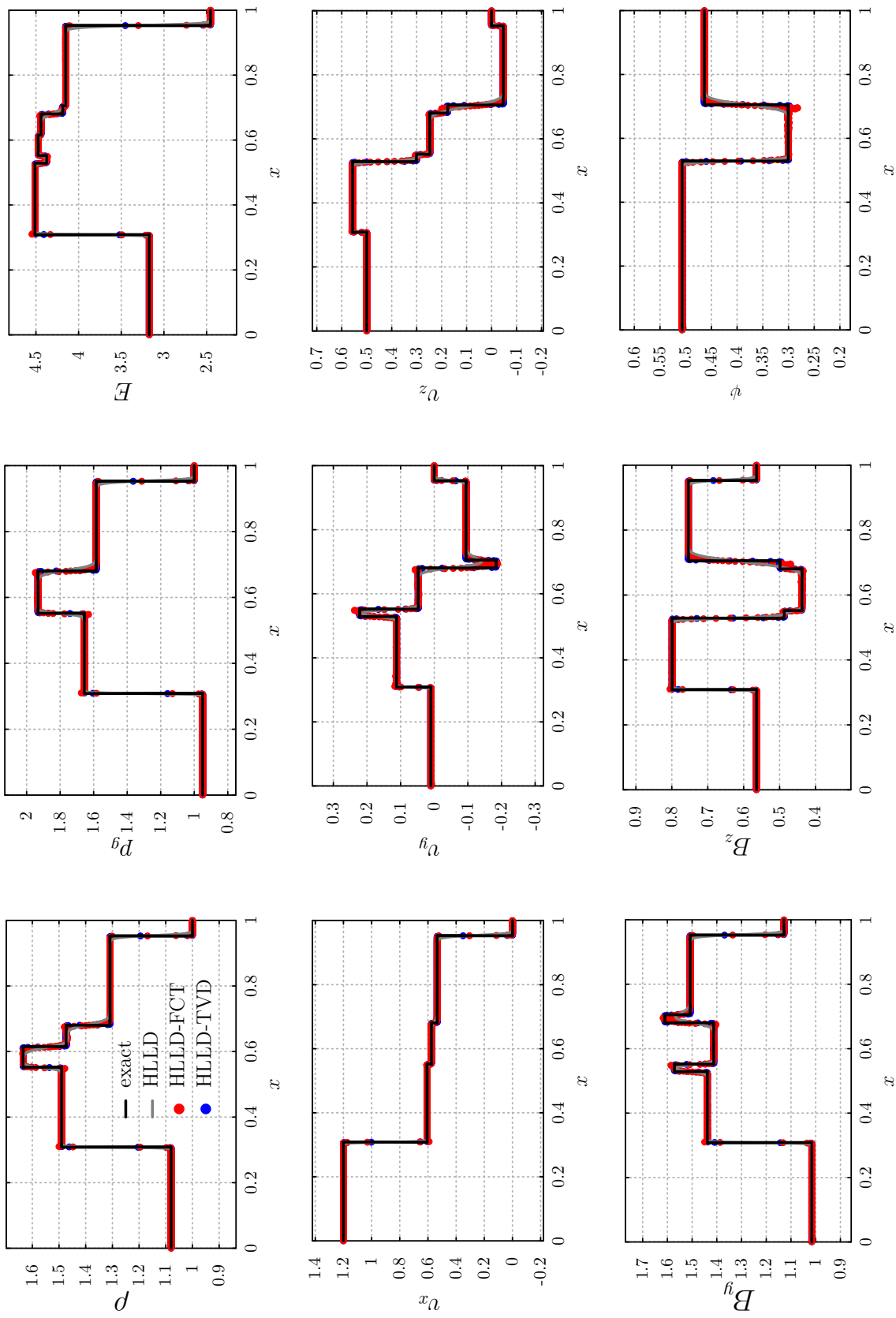


Figure 3.8: Solution of MHD shock tube test 1 at time 0.2. The initial conditions are given by (3.29). HLLC-TVD solution generated with Athena [30]. All other solutions generated with code written for this dissertation: <https://github.com/akercher/dissertation>.

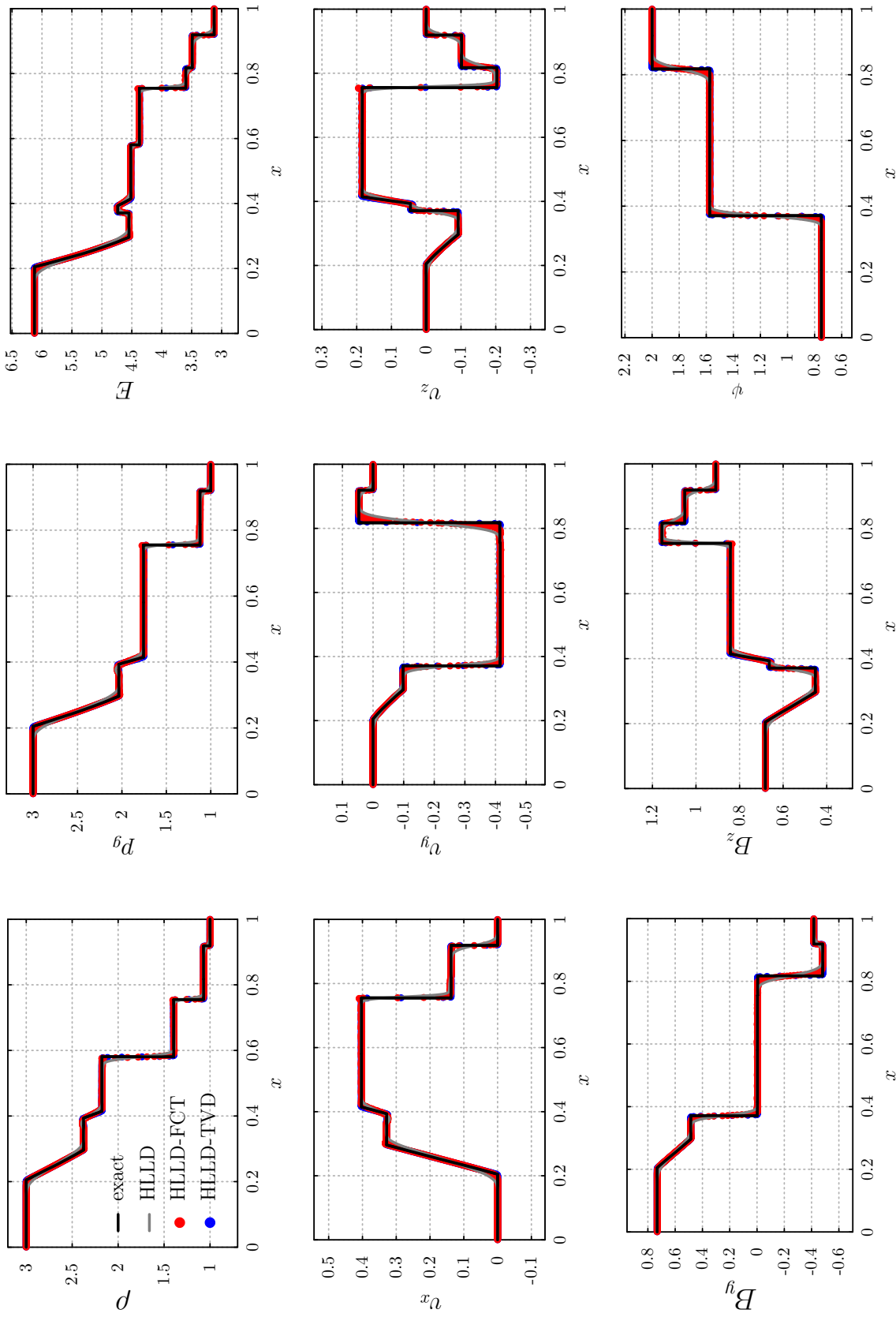


Figure 3.9: Solution of MHD shock tube test 2 at time 0.2. The initial conditions are given by (3.30). HLLC-TVD solution generated with Athena [30]. All other solutions generated with code written for this dissertation: <https://github.com/akercher/dissertation>.

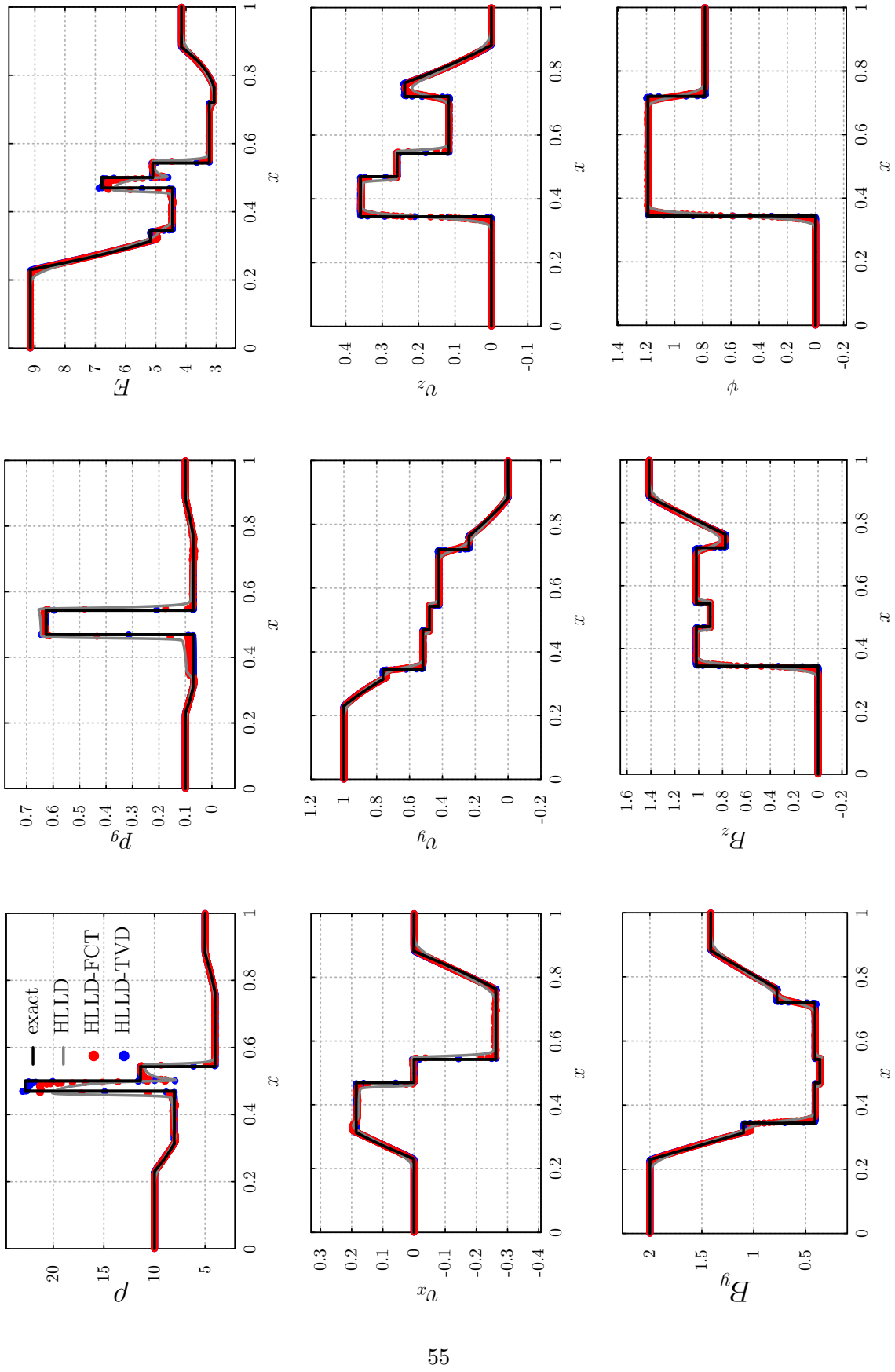


Figure 3.10: Solution of MHD shock tube test 3 at time 0.3. The initial conditions are given by (3.31). HLLC-TVD solution generated with Athena [30]. All other solutions generated with code written for this dissertation: <https://github.com/akercher/dissertation>.

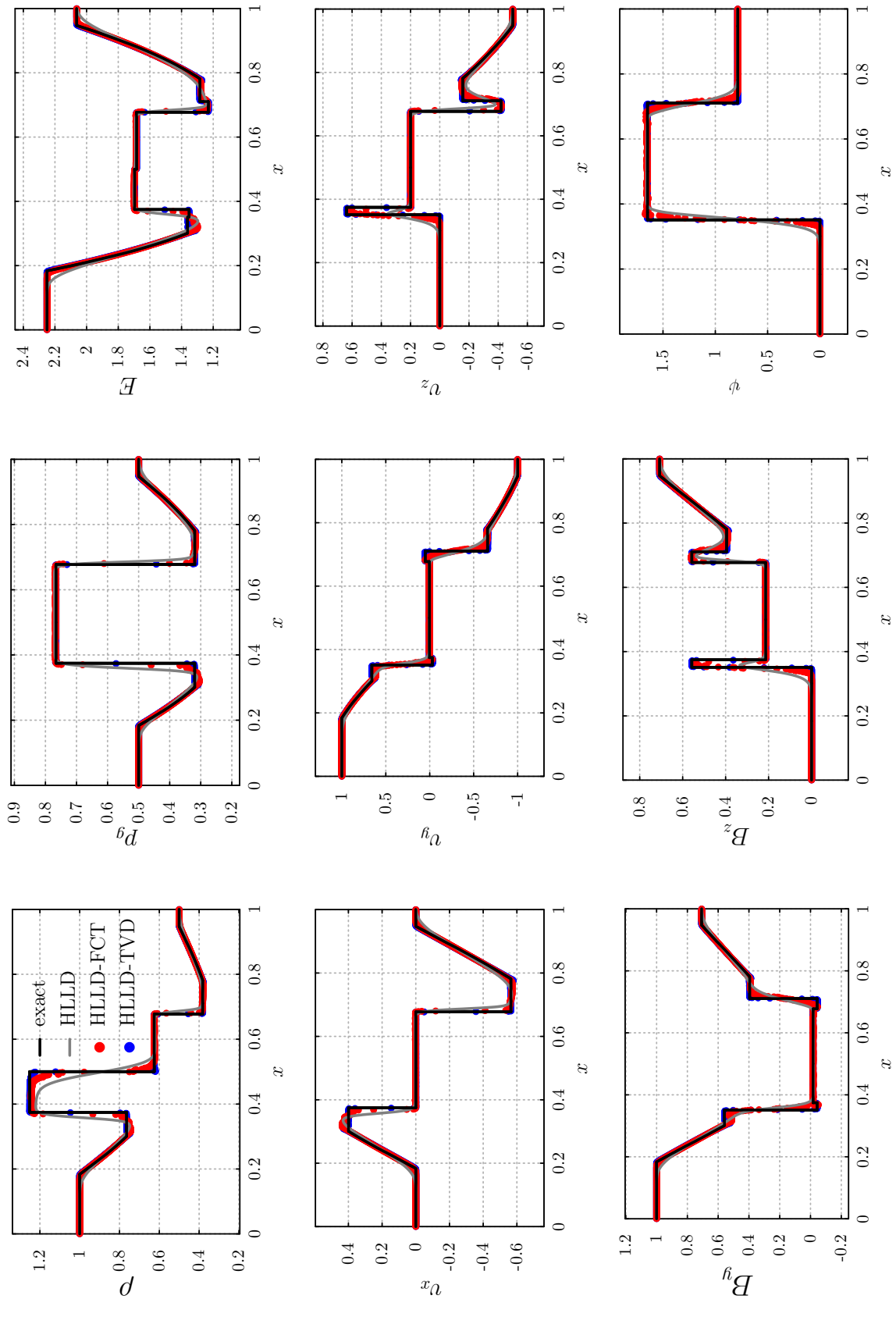


Figure 3.11: Solution of MHD shock tube test 4 at time 0.2. The initial conditions are given by (3.32). HLLC-TVD solution generated with Athena [30]. All other solutions generated with code written for this dissertation: <https://github.com/akercher/dissertation>.

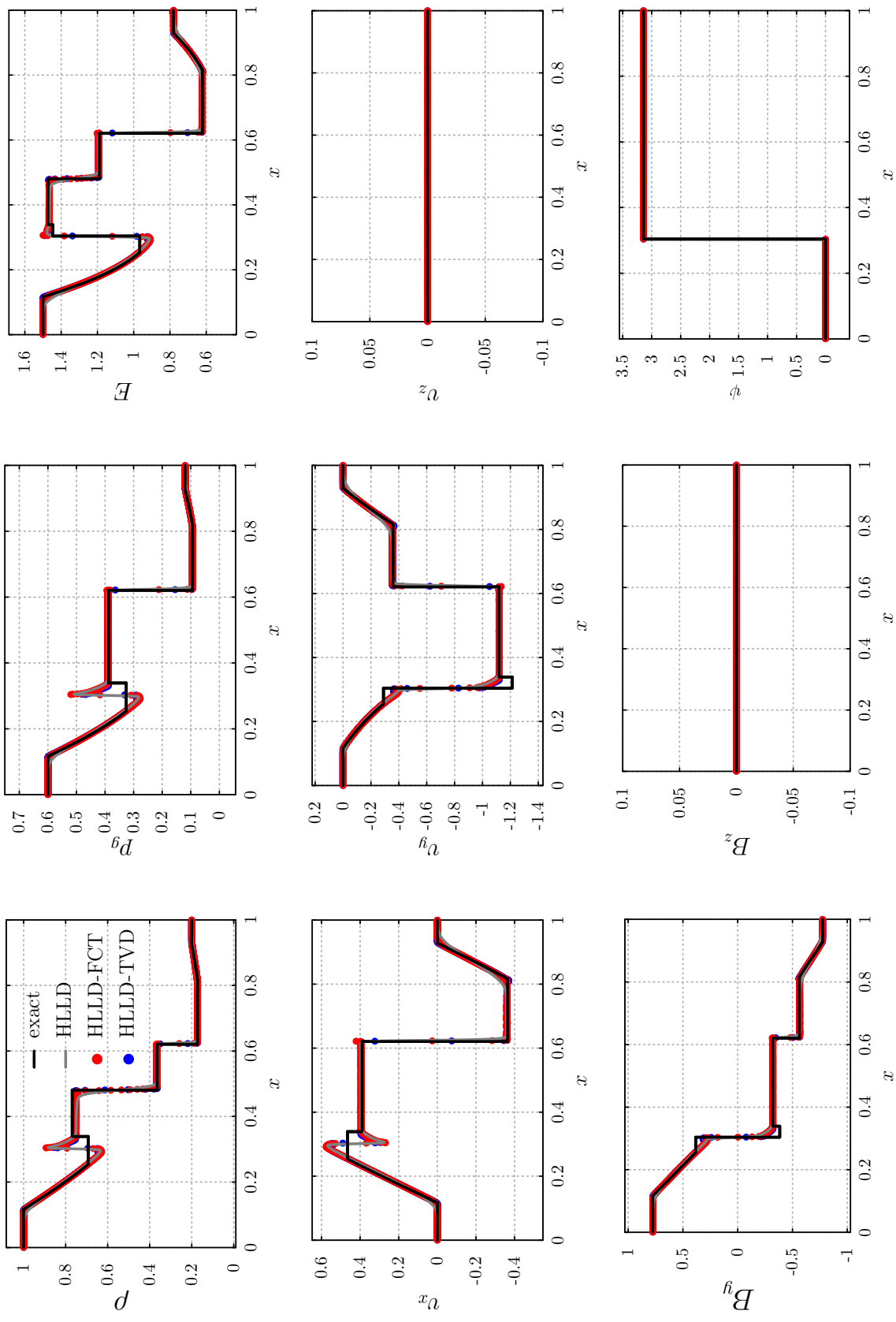


Figure 3.12: Solution of MHD shock tube test 5a (3.33) with $\alpha = \pi$, at time 0.2066. HLLC-TVD solution generated with Athena [30]. All other solutions generated with code written for this dissertation: <https://github.com/akercher/dissertation>.

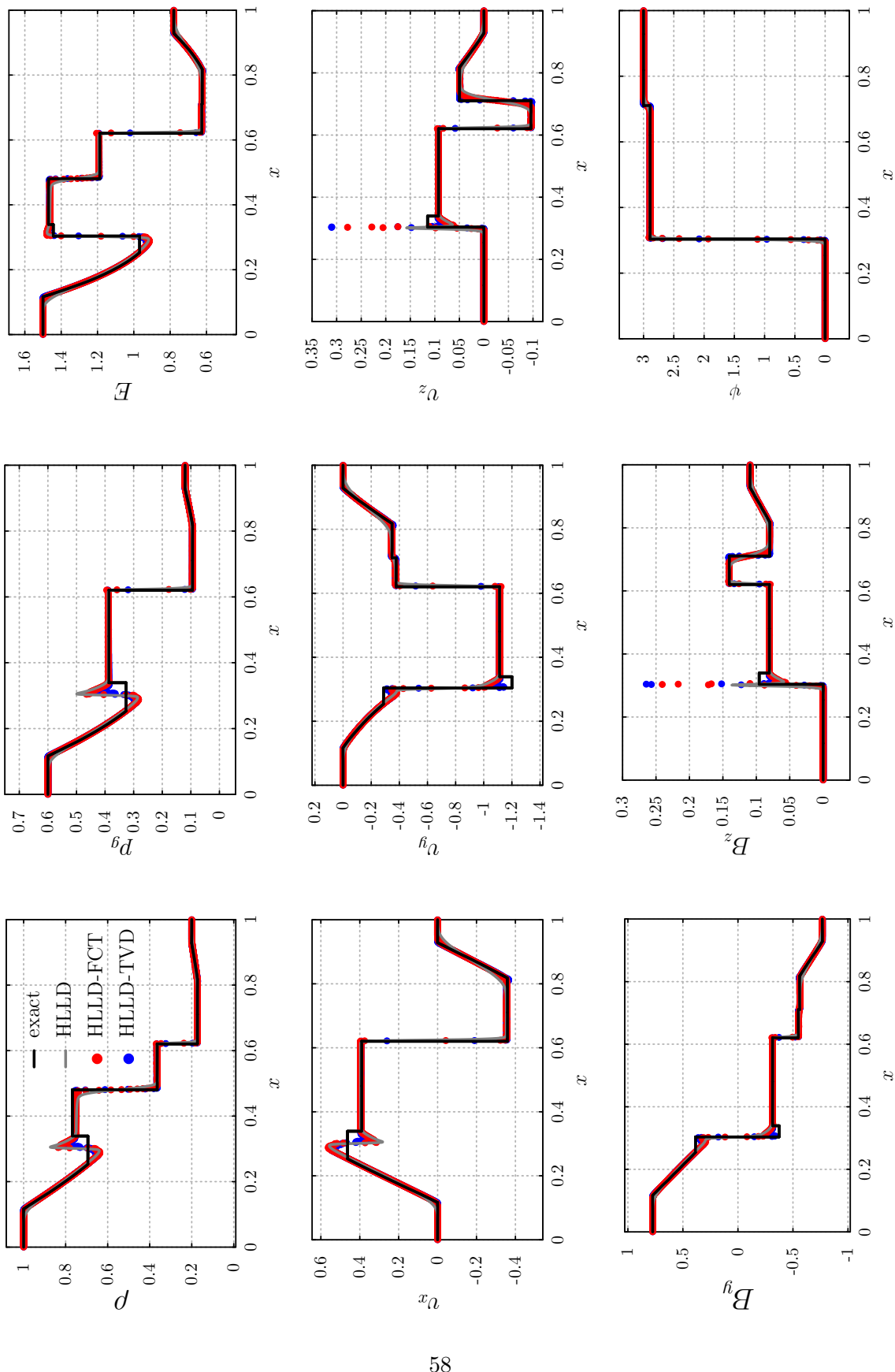


Figure 3.13: Solution of MHD shock tube test 5b (3.33) with $\alpha = 3.0$, at time 0.2066. HLLC-TVD solution generated with Athena [30]. All other solutions generated with code written for this dissertation: <https://github.com/akercher/dissertation>.

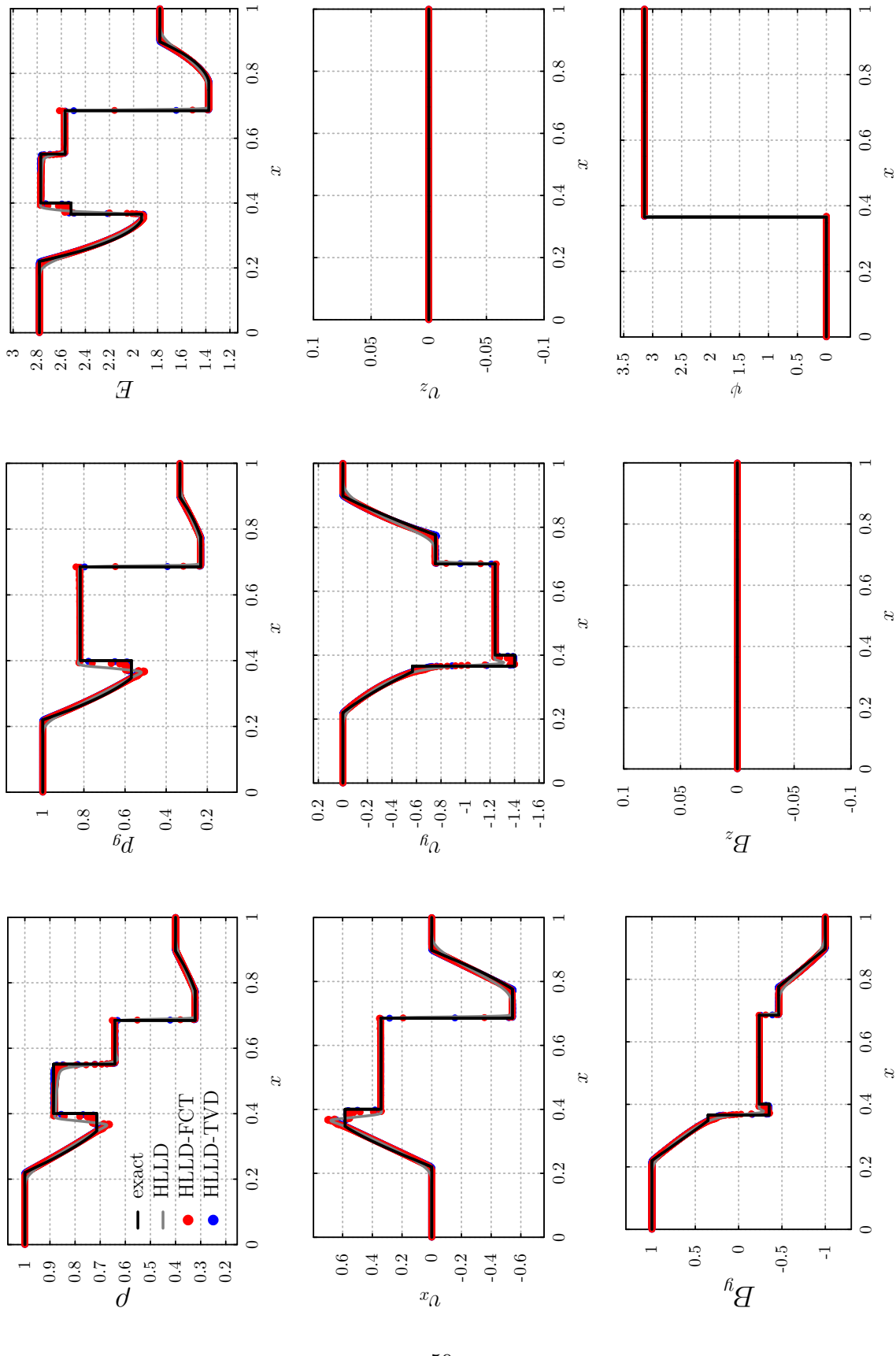


Figure 3.14: Solution of MHD shock tube test 6a (3.34) with $\alpha = \pi$, at time 0.15. HLIC-TVD solution generated with Athena [30]. All other solutions generated with code written for this dissertation: <https://github.com/akercher/dissertation>.

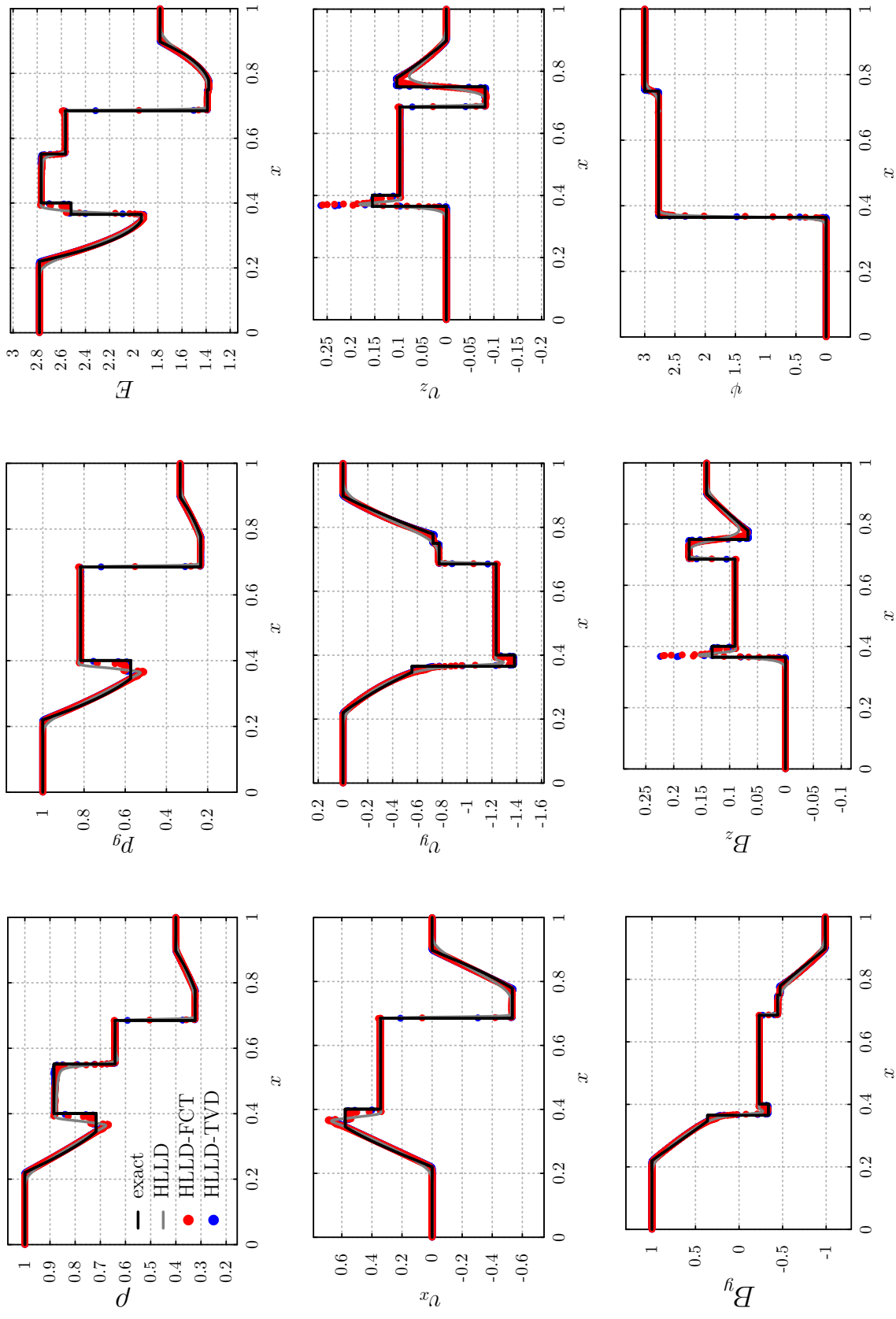


Figure 3.15: Solution of MHD shock tube test 6b (3.34) with $\alpha = 3.0$, at time 0.15. HLLC-TVD solution generated with Athena [30]. All other solutions generated with code written for this dissertation: <https://github.com/akercher/dissertation>.

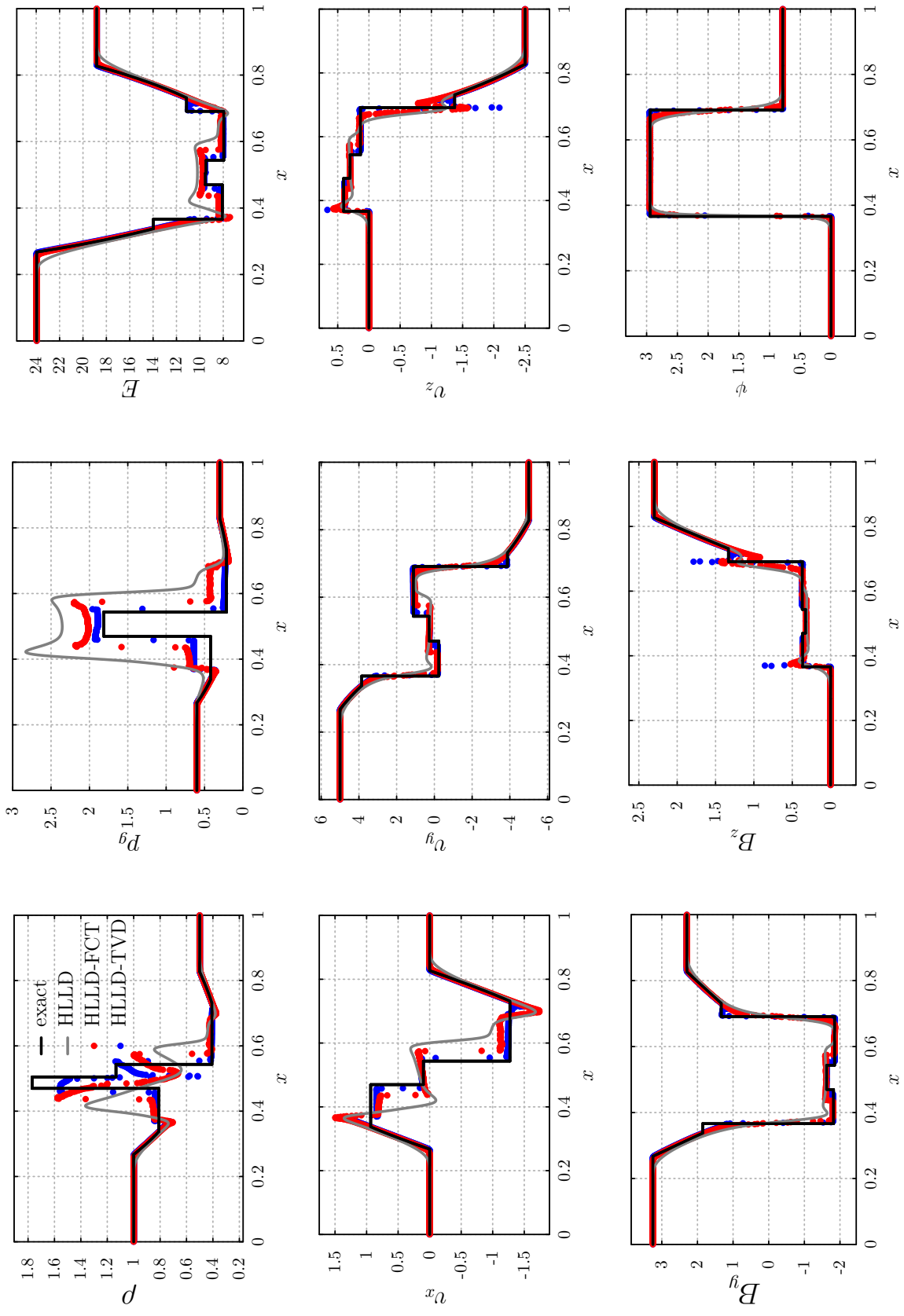


Figure 3.16: Solution of MHD shock tube test 7 (3.35) at time 0.05. HLLC-TVD solution generated with Athena [30]. All other solutions generated with code written for this dissertation: <https://github.com/akercher/dissertation>.

Table 3.17: Exact solution of MHD shock tube test 7 (solid black line of Figure 3.16)

ρ	v_n	v_y	v_z	p_g	B_t	ψ
1.0000E+0	0.0000E+0	5.0000E+0	0.0000E+0	6.0000E-1	3.2500E+0	0.0000E+0
8.0908E-1	9.3535E-1	3.8493E+0	0.0000E+0	4.2152E-1	1.8551E+0	0.0000E+0
8.0908E-1	9.3535E-1	-2.3529E-1	4.0446E-1	4.2152E-1	1.8551E+0	2.9442E+0
1.7694E+0	9.9120E-2	2.7519E-1	3.0237E-1	1.8144E+0	1.6554E+0	2.9442E+0
1.1339E+0	9.9120E-2	2.7519E-1	3.0237E-1	1.8144E+0	1.6554E+0	2.9442E+0
4.0738E-1	-1.2734E+0	1.1081E+0	1.3579E-1	2.1323E-1	1.8834E+0	2.9442E+0
4.0738E-1	-1.2734E+0	-3.8721E+0	-1.3721E+0	2.1323E-1	1.8834E+0	7.8540E-1
5.0000E-1	0.0000E+0	-5.0000E+0	-2.5000E+0	3.0000E-1	3.2500E+0	7.8540E-1

$B_n = 3.25$

Table 3.18: Residual and wave speeds of MHD shock tube test 7

Iteration	Residual	W_{fl}	W_{sl}	W_{sr}	W_{fr}
1	5.7203E-1	-4.0762E+0	-1.5950E+0	1.3839E+0	2.9997E+0
2	1.8913E-1	-3.9828E+0	-1.3063E+0	1.0509E+0	2.8512E+0
3	8.6393E-3	-3.9542E+0	-1.2395E+0	8.8355E-1	2.7973E+0
4	1.7363E-4	-3.9524E+0	-1.2465E+0	8.7248E-1	2.7925E+0
5	1.2942E-7	-3.9524E+0	-1.2466E+0	8.7262E-1	2.7925E+0

to determine the type of intermediate shock produced by the approximate solutions. The states directly upstream and downstream of the intermediate shock were approximated with the HLLD-FCT code developed for this dissertation, on a grid consisting of 2048 cells.

For coplanar case of test 5, the intermediate shock is traveling with a velocity of $S = -0.46546$. The state variables directly upstream are: $\rho_u = 0.6428$, $v_{nu} = 0.5520$, $v_{yu} = -0.3723$, $v_{zu} = 0.0$, $p_{gu} = 0.2873$, $B_{tu} = 0.3027$, $c_{fu} = 1.1295$, $c_{au} = 0.9661$, $c_{su} = 0.7382$, $c_{0u} = 0.8630$, and $v_{su} = 1.0174$ is the flow velocity in the shock reference frame. The state variables directly upstream are: $\rho_d = 0.8876$, $v_{nd} = 0.2686$, $v_{yd} = -0.8935$, $v_{zd} = 0.0$, $p_{gd} = 0.5152$, $B_{td} = -0.1168$, $c_{fd} = 1.0067$, $c_{ad} = 0.8222$, $c_{sd} = 0.8033$, $c_{0d} = 0.9835$, and $v_{sd} = 0.7341$. The Mach number w.r.t. the Alfvén speed is, $M_{au} = 1.0531$ upstream and $M_{ad} = 0.8928$ downstream. The flow upstream is subfast, and super-Alfvénic, $c_{au} < v_{su} < c_{fu}$, while downstream it is subslow, and sub-Alfvénic, $v_{sd} < c_{sd}, c_{ad}$. Thus, the compound wave is composed of a 2-4 intermediate shock followed by a SR.

For the coplanar case of test 6, the intermediate shock is traveling with a velocity of

$S = -0.8961$. The state variables directly upstream are: $\rho_u = 0.6671$, $v_{nu} = 0.6908$, $v_{yu} = -0.8670$, $v_{zu} = 0.0$, $p_{gu} = 0.5102$, $B_{tu} = 0.09560$, $c_{fu} = 1.5401$, $c_{au} = 1.5301$, $c_{su} = 1.1220$, $c_{0u} = 1.1290$, and $v_{su} = 1.5868$ is the flow velocity in the shock reference frame. The state variables directly upstream are: $\rho_d = 0.7232$, $v_{nd} = 0.5677$, $v_{yd} = -1.3912$, $v_{zd} = 0.0$, $p_{gd} = 0.5862$, $B_{td} = -0.3462$, $c_{fd} = 1.5868$, $c_{ad} = 1.4698$, $c_{sd} = 1.0766$, $c_{0d} = 1.1622$, and $v_{sd} = 1.4638$. The Mach number w.r.t. the Alfvén speed is, $M_{au} = 1.0369$ upstream and $M_{ad} = 0.9959$ downstream. The flow upstream is superfast, and super-Alfvénic , $c_{au}, c_{fu} < v_{su}$, while downstream it is superslow, and sub-Alfvénic, $c_{sd} < v_{sd} < c_{ad}$. Thus, the compound wave is composed of a FR followed by a 1-3 intermediate shock.

Tests 5a and 6a are examples of Riemann problems with non-unique solutions. Both the exact and approximate solutions satisfy the jump conditions of the shock because the tangential magnetic fields are exactly coplanar. Approximate solutions for Tests 5b and 6b give similar results, but are incorrect since the tangential magnetic field are only close to, but not exactly coplanar, the intermediate shock does not satisfy the jump conditions and should be considered unphysical. A more detailed explanation of non-unique solutions and numerical complications in problems close to non-uniqueness is given next section. In Chapter 4, a new method for removing the ambiguity, i.e., the solution the approximation converges to, is described.

3.5 Non-unique solutions to Riemann problems of ideal magnetohydrodynamics

Unique solutions to Riemann problems of ideal MHD are not guaranteed. For certain initial conditions, the Riemann problem will have non-unique solutions. Non-unique solutions will occur for problems with coplanar (anti-parallel) magnetic fields [2]. One solution has a 180° rotational discontinuity and slow shock and the other solution has a compound wave. A method for constructing Riemann problems with non-unique solutions and non-planar initial conditions is given by Torrilhon [37]. As with the coplanar case, one solution consists

of a 180° rotational discontinuity and a slow shock and the other solution has a compound wave. As discussed in this section, for cases with a 180° rotation in the solution (either a compound wave or rotational discontinuity), convergence to the solution containing only a rotational discontinuity is impossible with numerical approximations based on the finite volume method.

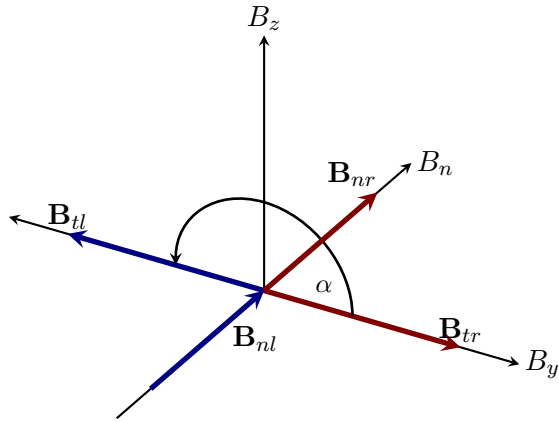


Figure 3.17: Initial configuration for a coplanar magnetic field on both sides of the discontinuity.

Using the same terminology and notation as Torrilhon [36], intermediate shocks and compound waves are referred to as non-regular structures. Regular structures include rarefactions, linear discontinuities, and Lax shocks. The solution of the ideal MHD Riemann problem that includes only regular structures is referred to as the r-solution. The solution that contains a compound wave is referred to as the c-solution.

In this work, we use the coplanar and near coplanar cases of Test 5 and 6. Test 5 was considered by Torrilhon [36]. The initial conditions (3.33) and parameters used here are equivalent but have been scaled to the unit interval $[0, 1]$ using

$$\hat{\rho} = \frac{\rho}{\rho_l}, \quad \hat{\mathbf{v}} = \frac{\mathbf{v}}{a_l}, \quad \hat{\mathbf{B}} = \frac{\mathbf{B}}{\sqrt{\gamma p_{gl}}}, \quad \hat{p}_g = \frac{p_g}{\gamma p_{gl}}, \quad \hat{L}_x = 1, \text{ and } \hat{t}_f = \frac{a_l t_f}{L_x}. \quad (3.36)$$

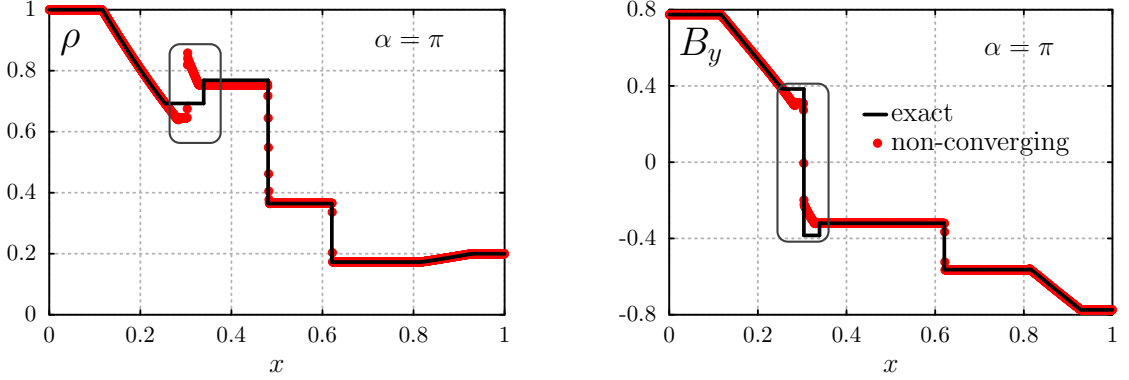


Figure 3.18: Non-convergence for the coplanar case. A non-regular structure (compound wave) in the approximate solution exists in place of the rotational discontinuity in the exact solution at $x = 0.303$. The domain used for error analysis is $x = [0.254, 0.481]$.

The initial discontinuity is located at $x = 0.4$, the final time is $t_f = 0.207$. The exact solution containing only regular structures and the approximate solution containing a compound wave for ρ and B_y are shown in Figure 3.18. For a numerical scheme to converge to the r-solution, the density and the magnitude of the transverse magnetic field must remain constant between the left-going fast and slow structures, shown in Figure 3.18 at $x = 0.254$ and $x = 0.339$ respectively, otherwise a compound wave will appear.

The coplanar case of Test 6 was considered in [28], except we have used $p_{gr} = 1/3$, and $B_n = 1.25$. The initial conditions are given by (3.34). The initial discontinuity is located at $x = 0.5$, the final time is $t_f = 0.15$. The exact solution containing only regular structures and the approximate solution containing a compound wave for ρ and B_y are shown in Figure 3.18. The density and the magnitude of the transverse magnetic field must remain constant between the left-going fast and slow structures, shown in Figure 3.19 at $x = 0.347$ and $x = 0.401$ respectively, otherwise a compound wave will appear.

Falle and Komissarov [16] described the appearance of compound waves in numerical simulations in terms of the properties of the planar ideal MHD equations. In this case, the system of equations is reduced from seven to five by removing the equations for the

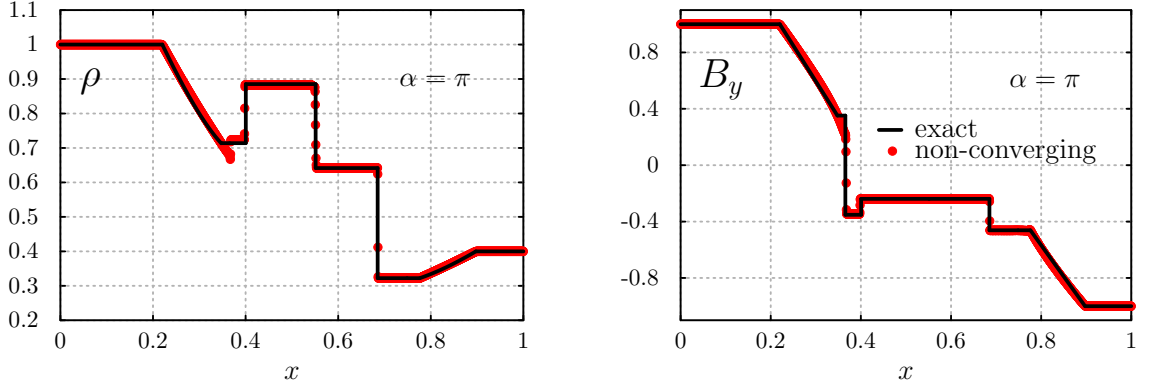


Figure 3.19: Non-convergence for the coplanar case. A non-regular structure (compound wave) in the approximate solution exists in place of the rotational discontinuity in the exact solution at $x = 0.365$. The domain used for error analysis is $x = [0.346, 0.551]$.

z -component of the velocity and magnetic field. In the reduced system, the Alfvén waves are lost but the other characteristic fields are unchanged. The Alfvén velocity is no longer a characteristic speed of the system but rotational discontinuities still satisfy the jump conditions and propagate at that velocity. In planar ideal MHD, a rotational discontinuity can only rotate the perpendicular magnetic field by 180° because it is restricted to a single plane.

Finite volume methods have no way of compensating for the reduction in dimension in the planar case. If one of the perpendicular components of velocity and magnetic field vanish, there is no mechanism to transfer energy between the perpendicular field components across the rotational discontinuity. The field in a cell would need to undergo a full 180° rotation in one time step in order for the magnitude of the perpendicular magnetic field to remain constant. Numerical diffusion and stability constraints prohibit the full rotation from being realized in one time step. In addition, any interpolation with order greater than piecewise constant will produce a magnetic field at the cell interface (where the flux is calculated) with a magnitude that is less than that in the center of the adjoining cells. From (2.38), any change in kinetic or magnetic energy will result in an increase in gas

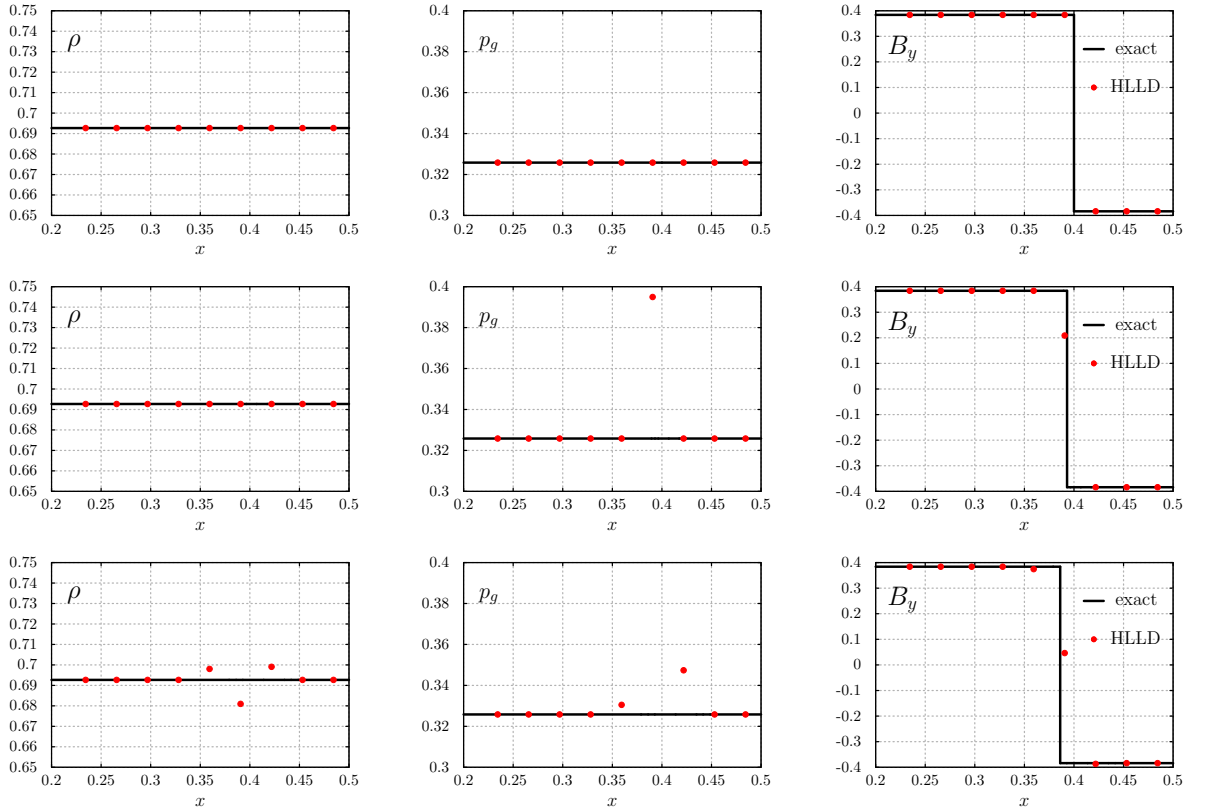


Figure 3.20: Top: initial state of left-going rotational discontinuity for the coplanar case of Test 5. Middle: the left-going rotational discontinuity for the coplanar case of Test 5 after onetime step. The gas pressure is increased as a result of the decrease in B_t . Bottom: the left-going rotational discontinuity for the coplanar case of Test 5 after two time steps. The artificial increase in pressure creates the compound wave.

pressure that is connected to the upstream state through a shock and the downstream state through a rarefaction wave (i.e., a compound wave). Thus, conservative finite volume schemes cannot converge to the r-solution for cases involving a 180° , or near 180° rotation. The formation of the compound wave is shown in Figure 3.20. This is especially problematic for low-resolution grids because a greater amount of numerical diffusion is expected [2, 36].

3.6 Nonuniform convergence

Numerical diffusion also produces compound waves in Riemann problems with initial conditions near a critical state with a non-unique solution [36]. For these problems, the angle between the perpendicular magnetic fields separated by the initial discontinuity, called the twist angle α , determines uniqueness. Solutions for $\alpha \neq n\pi$, with $n \in \mathbb{Z}$ are unique. Compound waves appear in numerical solutions on coarse grids as α approaches $n\pi$ [36]. A compound wave connecting non-planar states, i.e. $\alpha \neq n\pi$, does not satisfy the Rankine-Hugoniot equations (2.39)-(2.43) and a numerical solution containing one is therefore not correct. As numerical diffusion is decreased through grid refinement, the compound wave loses its structure and the regular waves emerge. Torrilhon [36] called this property pseudo-convergence because convergence is initially towards the c-solution; divergence from the c-solution only occurs when enough diffusion is eliminated through grid refinement. The solution for various levels of grid refinement are shown for a near-coplanar cases of Test 5 and Test 6 in Figure 3.21 and Figure 3.22 respectively. Torrilhon [36] reported that a simulation using 20,000 grid points had not completely converged to the r-solution. Pseudo-convergence also occurs in non-planar MHD Riemann problems with initial conditions near a critical state with a non-unique solution. The new CWM technique for removing pseudo-convergence is described in the following chapter. The technique is demonstrated on coplanar, near coplanar, and non-planar cases.

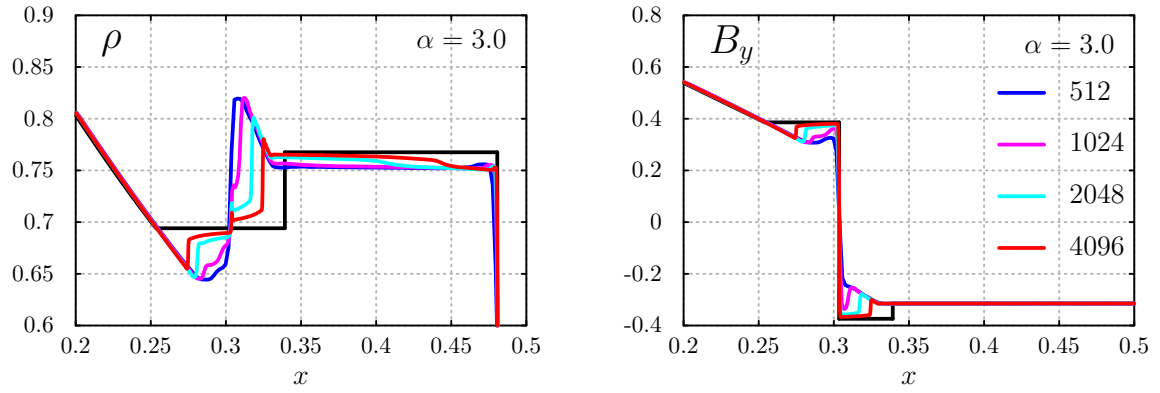


Figure 3.21: Pseudo-convergence for a near-coplanar case. As the grid is refined from 1024 and 2048 points, the solution begins to diverge from the c-solution.

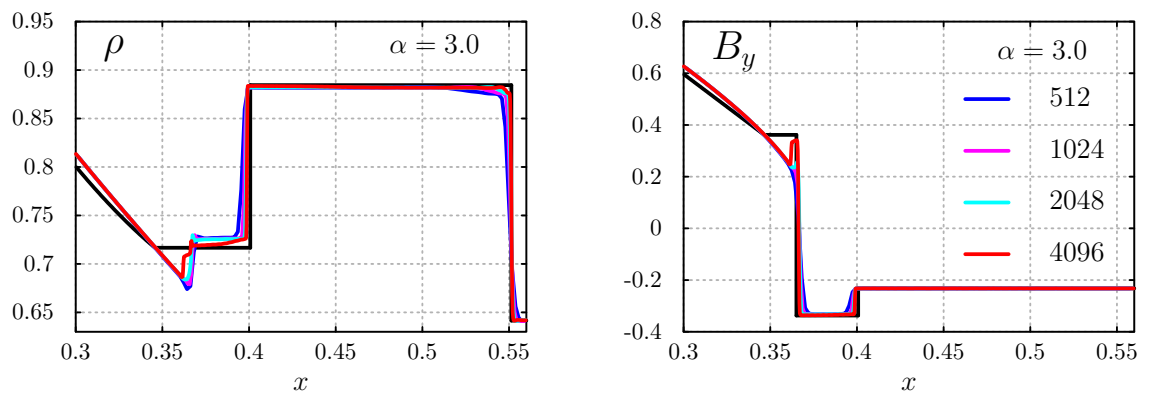


Figure 3.22: Pseudo-convergence for a near-coplanar case. As the grid is refined from 1024 and 2048 points, the solution begins to diverge from the c-solution.

Chapter 4: Compound wave modification

In Chapter 3, it was shown that FV schemes exhibit pseudo-convergence, where convergence to the solution containing regular waves only occurs at higher grid resolutions, for near coplanar case, and not at all for the coplanar case of a Riemann problem of ideal MHD. This chapter gives a detailed explanation of the formation of a compound wave and purposes a new method that involves modifying HLLD flux, which produces solutions with only regular waves at all grid resolution for coplanar and non-planar cases. The process, referred to as compound wave modification (CWM), approximates the flux associated with the compound wave and removes it from the HLLD flux before the solution is advanced in time. The performance increase from the new HLLD-CWM is demonstrated with root-square-mean-error (RMSE) calculations.

4.1 Convergence with finite volume schemes

The influence of a compound wave on the numerical solution can be minimized by limiting the artificial perturbation in pressure caused by numerical diffusion. We do this by subtracting flux so that only the tangential components of momentum and the magnetic field are affected and thus the upstream and downstream states will still satisfy the jump conditions for a rotational discontinuity. The subtracted flux is chosen to be proportional to the flux contribution of the compound wave. We refer to this as compound wave modification (CWM) and its use in conjunction with HLLD as HLLD-CWM. The flux responsible for the formation of the compound wave is calculated by solving a reduced Riemann problem with initial conditions set to the upstream and downstream states of the 180° rotational discontinuity. These intermediate states correspond to regions \mathbf{U}_l^* and \mathbf{U}_{2l}^* of Figure 2.11 for the coplanar (near-coplanar) problem shown in Figure 3.18 (3.21). For test 5a, the exact

values in the intermediate region are given by rows 2 and 3 of Table 3.9. The exact values are generally not known, so they are approximated with HLLD. If the wave is traveling in the positive direction, i.e., the direction of the outward face normal, then intermediate states correspond to regions \mathbf{U}_{2r}^* and \mathbf{U}_r^* of Figure 2.11. The direction of the wave is determined by the wave speeds, S_m (2.51), and S_r^* (2.61). The interface state are \mathbf{U}_l^* and \mathbf{U}_{2l}^* , if $S_m > 0$, and \mathbf{U}_{2r}^* and \mathbf{U}_r^* , if $S_r^* > 0$.

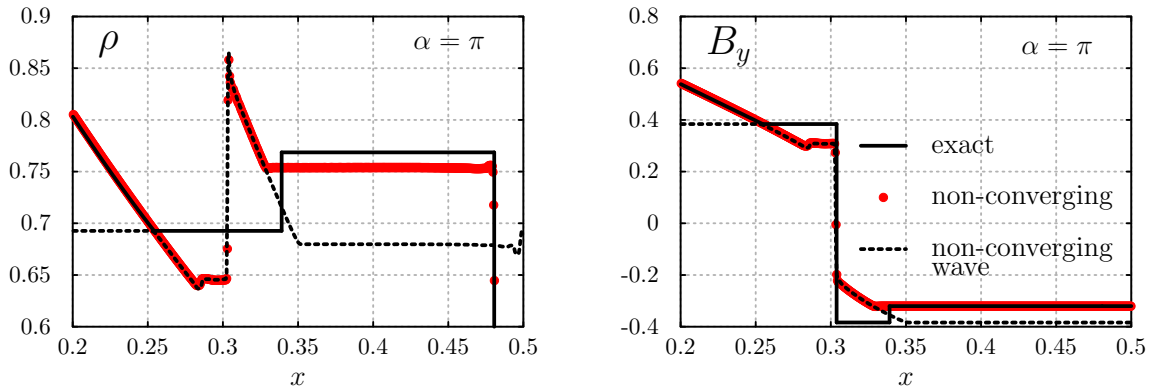


Figure 4.1: The slow compound wave of Test 5a, approximate non-converging c-solution, and exact r-solution for the coplanar case.

The solution to the reduced coplanar Riemann problem as well as the solution to the full coplanar Riemann problem are shown in Figure 4.1. Three left-going structures are visible in the solution to the reduced Riemann problem. The intermediate shock at $x \approx 0.3$ is directly followed by a slow rarefaction whose head is located at $x \approx 0.3$ and tail at $x \approx 0.32$. The speed at the head of the slow rarefaction equals the speed of the intermediate wave, $v - c_a$, and the two structures move together forming a compound wave. The third structure in the compound wave solution is a fast rarefaction that connects the upstream state of the intermediate shock to the initial conditions. The speed at the head of the fast rarefaction (dotted black line in Figure 4.1) is equal to the speed at the tail of the fast rarefaction in the solution to the full coplanar Riemann problem (solid black line in Figure 4.1). These two fast rarefactions, one in the regular solution to the full Riemann problem and one in

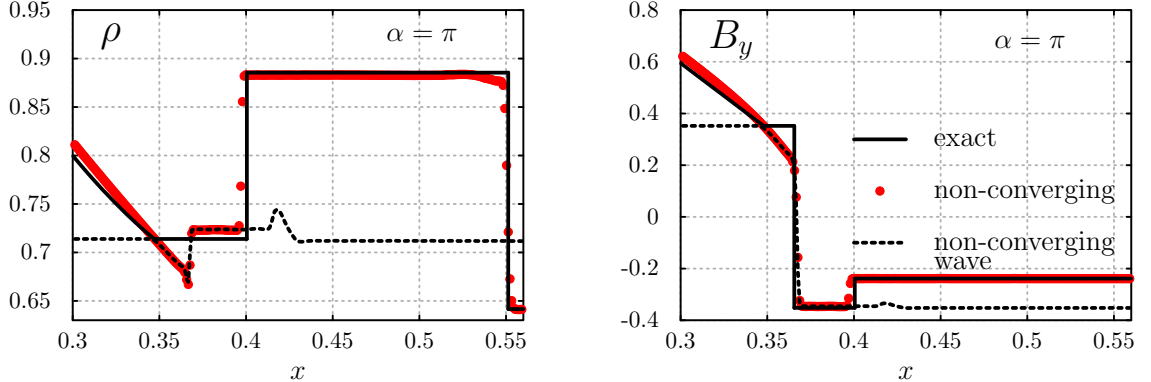


Figure 4.2: The fast compound wave of Test 6a, approximate non-converging c-solution, and exact r-solution for the coplanar case.

the compound wave, form a single structure in the compound wave solution to the full coplanar Riemann problem. The compound wave solution also produces a right-going slow rarefaction wave that connects the state downstream of the left-going slow rarefaction wave to the initial right-state. The change in density through the right-going slow rarefaction is equal to the difference in density between the exact solution and compound wave solution downstream (left) of the contact discontinuity, at $x \approx 0.48$ in Figure 4.1. The compound wave solution requires four structures, as opposed to one in the regular solution (i.e., the rotational discontinuity), to connect two intermediate states in full Riemann problem.

The intermediate states are calculated with the nonlinear solver described in Section 2.6.3. The accuracy is determined by the number of iterations. If the number of iterations is not restricted, the jump conditions can be satisfied to near machine precision. This precision was not used in the solutions presented here, but may be used when the solution is known to contain at most one non-regular structure. In that case, the exact solution only needs to be calculated once (at the beginning) and the intermediate states can be used for the remainder of the calculation. If the number of iterations is set to zero, the intermediate states are those found from the HLLD approximate Riemann solver. We have found convergence to the correct solution to be independent of the number of iterations used in the

exact solver. This is important because it eliminates the need of a nonlinear solver. Their implementation can be complex and they have the potential to diverge because of the use of Newton's method. The implementation of CWM is simplified because it uses the HLLD intermediate states.

It is important to limit the removal of the flux responsible for producing the compound wave in a way that does not affect the solution in other parts of the domain. In CWM, the flux is modified if the cell is located in a discontinuity region with a near- 180° rotation. Cell i is considered to be in such a discontinuity region when $|\psi_{i+1} - \psi_{i-1}| > \beta_T$ where β_T is a threshold value. Unless otherwise stated, a value of $\beta_T = 2.0$ radians was used. This criteria ensures that the flux across regular shocks, waves, or contact discontinuities is unchanged and only rotational discontinuities with a large change in α are affected. Only rotational discontinuities can change the orientation of the tangential magnetic field if the normal component of the magnetic field is nonzero. If this criteria is met, the intercell flux at i is modified according to $\mathbf{F}_i^r = \mathbf{F}_i^r - A\mathbf{F}_i^c$, where \mathbf{F}^r is the flux for the full Riemann problem, \mathbf{F}^c is the flux due to the compound wave, and A is a user-specified constant. The value of A determines the states upstream and downstream of the rotational discontinuity. We set $A = 0.1$ in the near-coplanar and coplanar problems shown in Figures 4.3 and 4.8 and set the Courant number less than 0.4 is used in order to limit oscillations downstream of the rotational discontinuity.

As shown in Figure 4.3, the transition across the rotational discontinuity is initially unresolved. The CWM procedure removes the compound wave from the solution except in this layer and leaves a deviation from the exact solution as the rotational discontinuity is crossed. Because the deviation occurs where there is a change in sign of the tangential magnetic field, it needs to be detected, unless an exact solver is used, in which case the location is determined from the wave speed.

A point is considered to be within the transition region of a 180° rotation if $|\alpha_{i+2} - \alpha_{i-2}| > 2.5$ rad. The state variables at these points must be adjusted in order to satisfy the jump conditions of a rotational discontinuity: $[\rho] = [v_n] = [p_g] = [B_\perp^2] = 0$, $\pm\sqrt{\rho}[v_y] = [B_y]$,

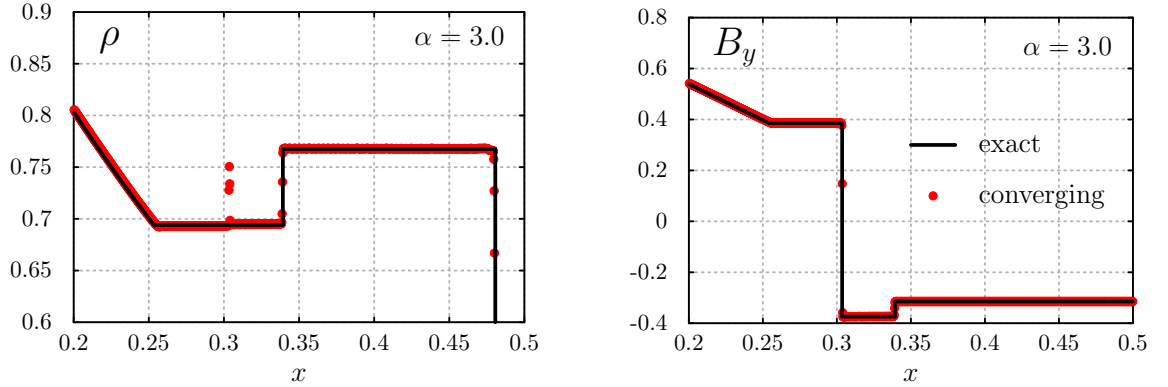


Figure 4.3: The approximate solution after the first flux correction of HLLD-CWM and exact r-solution to the full Riemann problem for the near-coplanar case with 4096 grid points. The compound wave is almost completely removed, except near $x = 0.303$ where a weak intermediate shock remains.

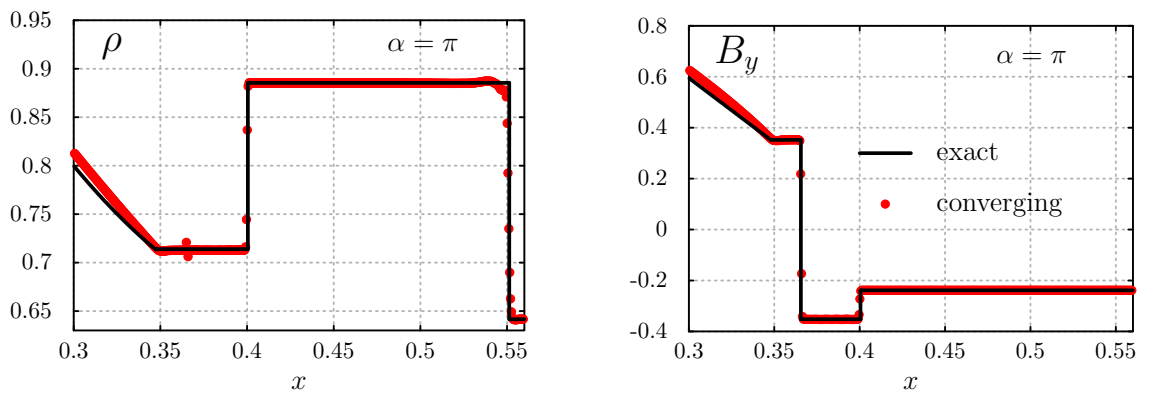


Figure 4.4: The approximate solution after the first flux correction of HLLD-CWM and exact r-solution to the full Riemann problem for the near-coplanar case with 2048 grid points. The compound wave is almost completely removed, except near $x = 0.365$ a weak intermediate shock remains.

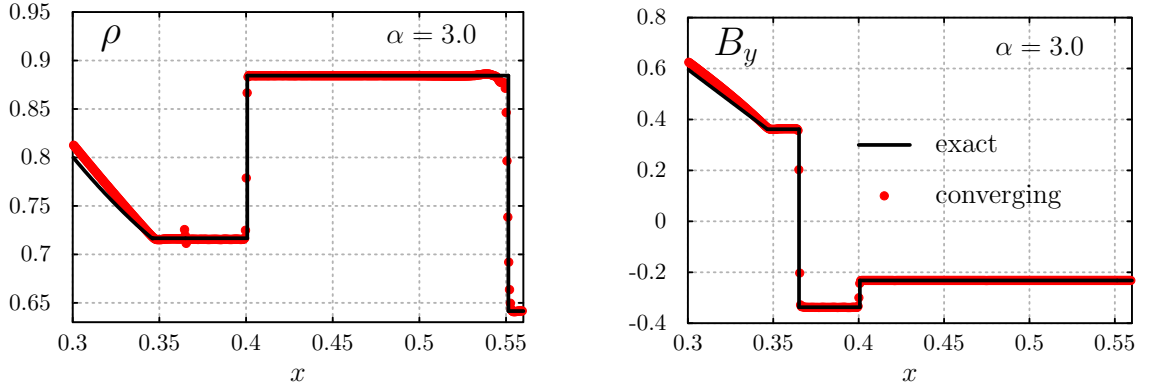


Figure 4.5: The approximate solution after the first flux correction of HLLD-CWM and exact r-solution to the full Riemann problem for the near-coplanar case with 2048 grid points. The compound wave is almost completely removed, except near $x = 0.365$ where a weak intermediate shock remains.

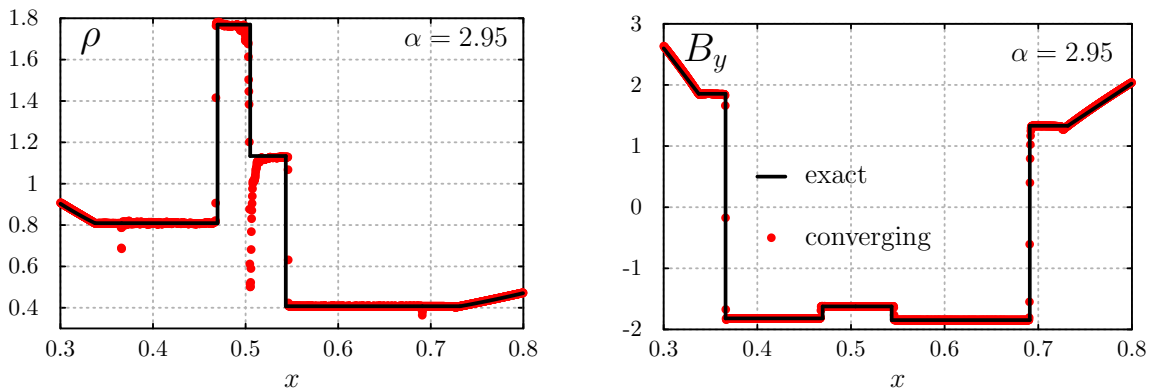


Figure 4.6: The approximate solution after the first flux correction of HLLD-CWM and exact r-solution to the full Riemann problem for the near-coplanar case of Test 5 with 4096 grid points. The compound wave is almost completely removed, except near $x = 0.366$ and $x = 0.691$ where weak intermediate shocks remain.

$\pm\sqrt{\rho}[v_y] = [B_y]$ $\pm\sqrt{\rho}[v_z] = [B_z]$, and $[E] = \pm\sqrt{\rho}[\mathbf{v} \cdot \mathbf{B}]$. A straight-forward adjustment is to have points with a rotation angle less (greater) than $\pi/2$ be assigned the value of the upstream (downstream) value outside of the transition. Although this approach produces acceptable results for the considered one-dimensional cases, it is not conservative because mass, momentum, and energy are removed. However, the magnetic energy in the transition can be transferred from one tangential component to the other while maintaining conservation and satisfying the jump conditions. We also note that the goal is to produce the correct states upstream and downstream of the rotational discontinuity, not to describe how energy is stored throughout the transition across the rotational discontinuity.

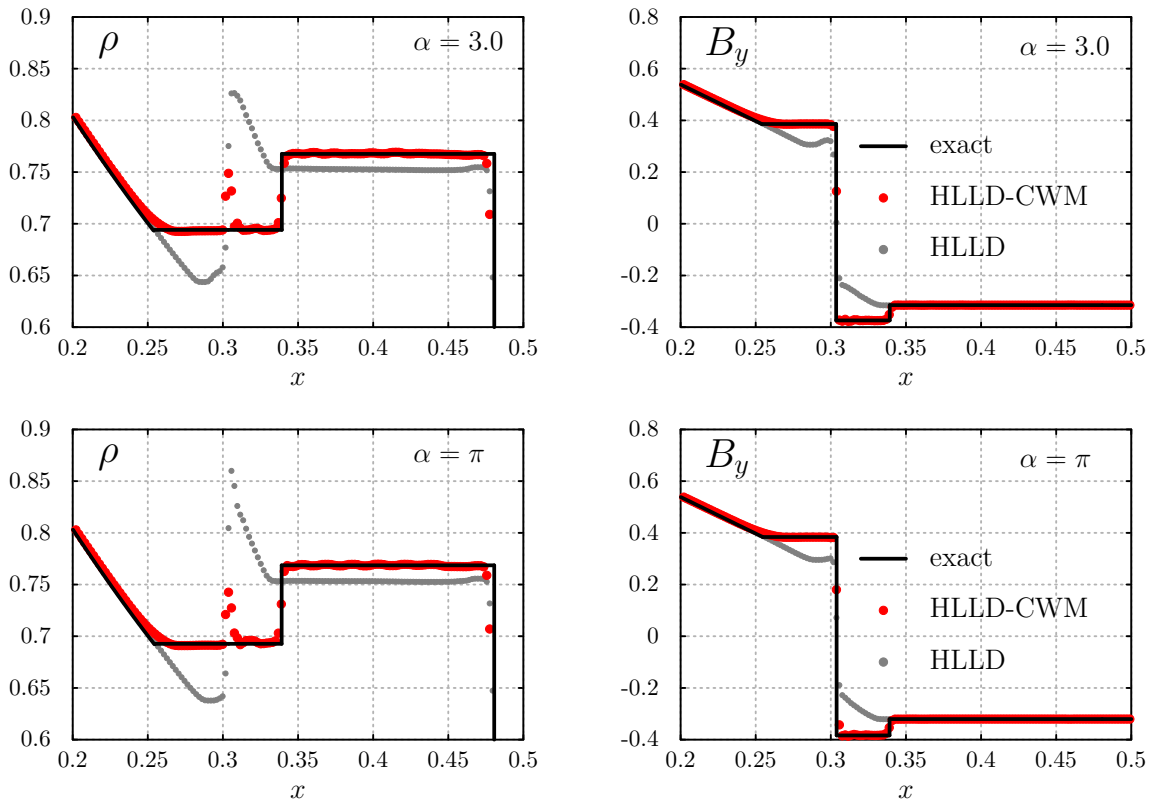


Figure 4.7: The rotational discontinuity and slow shock solution found using HLLD-CWM without the (optional) flux redistribution step, HLLD, and the exact solver using 512 grid points for (top) a near-coplanar and pseudo-converging case and (bottom) the planar and non-converging (bottom) case.

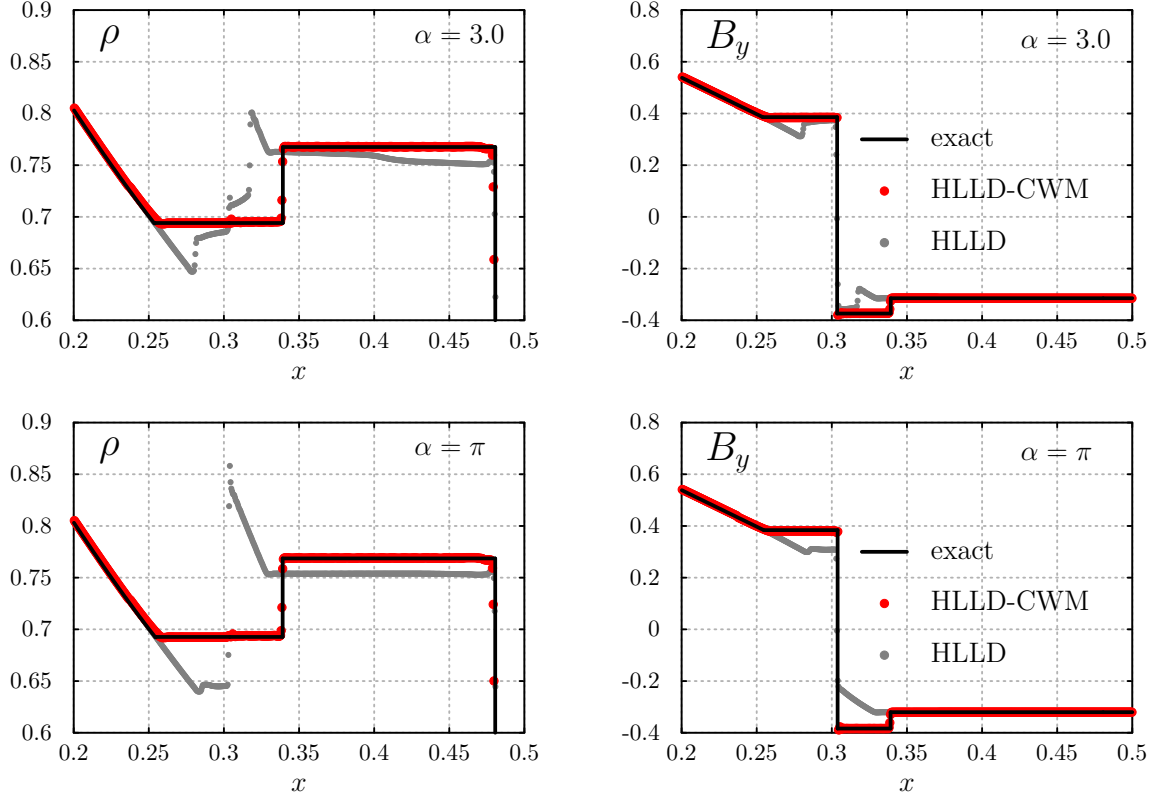


Figure 4.8: The rotational discontinuity and slow shock solution found using HLLD-CWM after the (optional) flux redistribution step, HLLD, and the exact solver using 2048 grid points for (top) a near-coplanar and pseudo-converging case and (bottom) the planar and non-converging (bottom) case.

Solutions obtained using HLLD-CWM, without any additional artificial viscosity, and HLLD for a near-coplanar case and the coplanar case of Test 5 with $A = 0.1$ for 512 grid points are shown in Figure 4.7, and for 2048 grid points are shown in Figure 4.8. The solutions now include a left-going rotational discontinuity and slow shock. This is the correct solution for ideal MHD. Pseudo-convergence does not occur in the coplanar case – successive refinement only reduces the error w.r.t. the r-solution. For the near-coplanar case, pseudo-convergence occurs – the compound wave structure is lost as the grid is refined from 1024 to 2048 points.

In the unmodified solution for the near-coplanar case of Test 5, the state between the left-going slow shock and the contact discontinuity slowly converges to the exact solution, but at different rates. The state should be constant throughout the region, but directly behind the left-going slow shock, the solution differs from the exact by $\approx 0.7\%$ and the difference behind the contact discontinuity is $\approx 2\%$. For the coplanar case, the solution in this region remains constant, but differs from the exact solution by $\approx 3\%$. These issues are eliminated with HLLD-CWM. The appearance of the rotational discontinuity and slow shock is independent of the value of α and the regular structures are present and have correct values for the state variables in both cases.

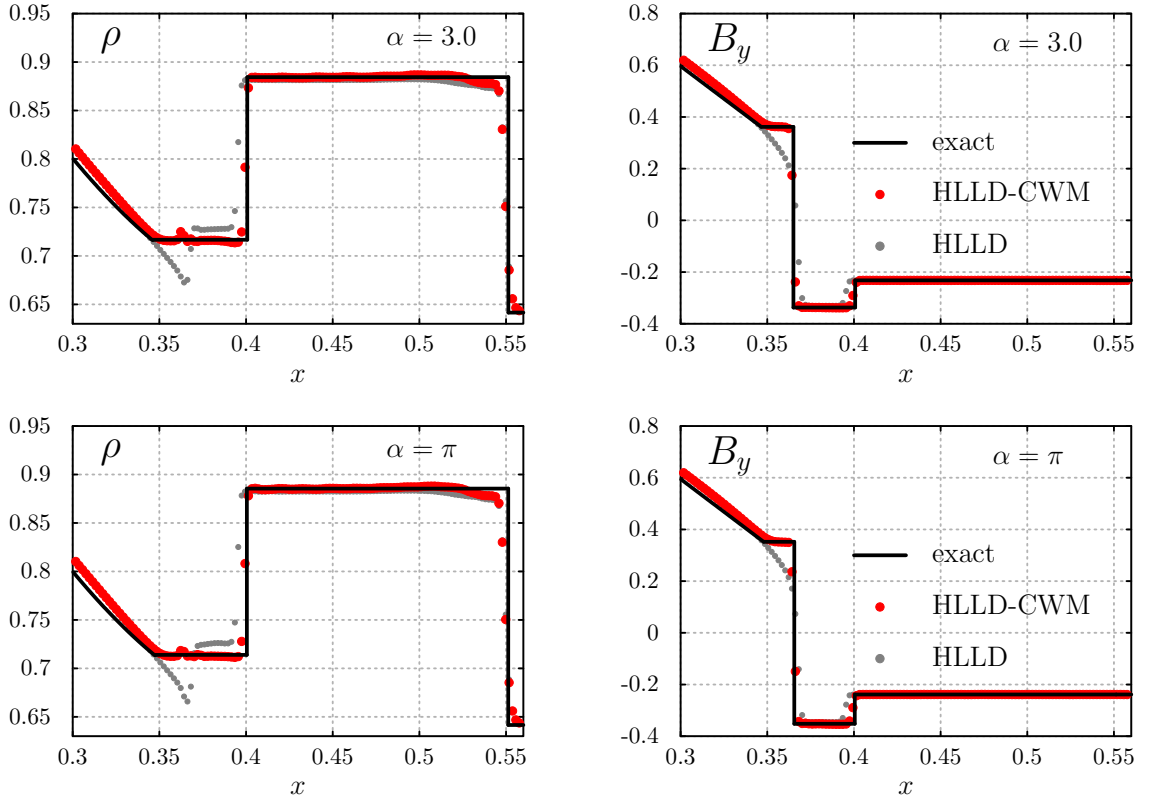


Figure 4.9: The fast rarefaction and rotational discontinuity solution found using HLLD-CWM without the (optional) flux redistribution step, HLLD, and the exact solver using 512 grid points for (top) a near-coplanar and pseudo-converging case and (bottom) the planar and non-converging (bottom) case.

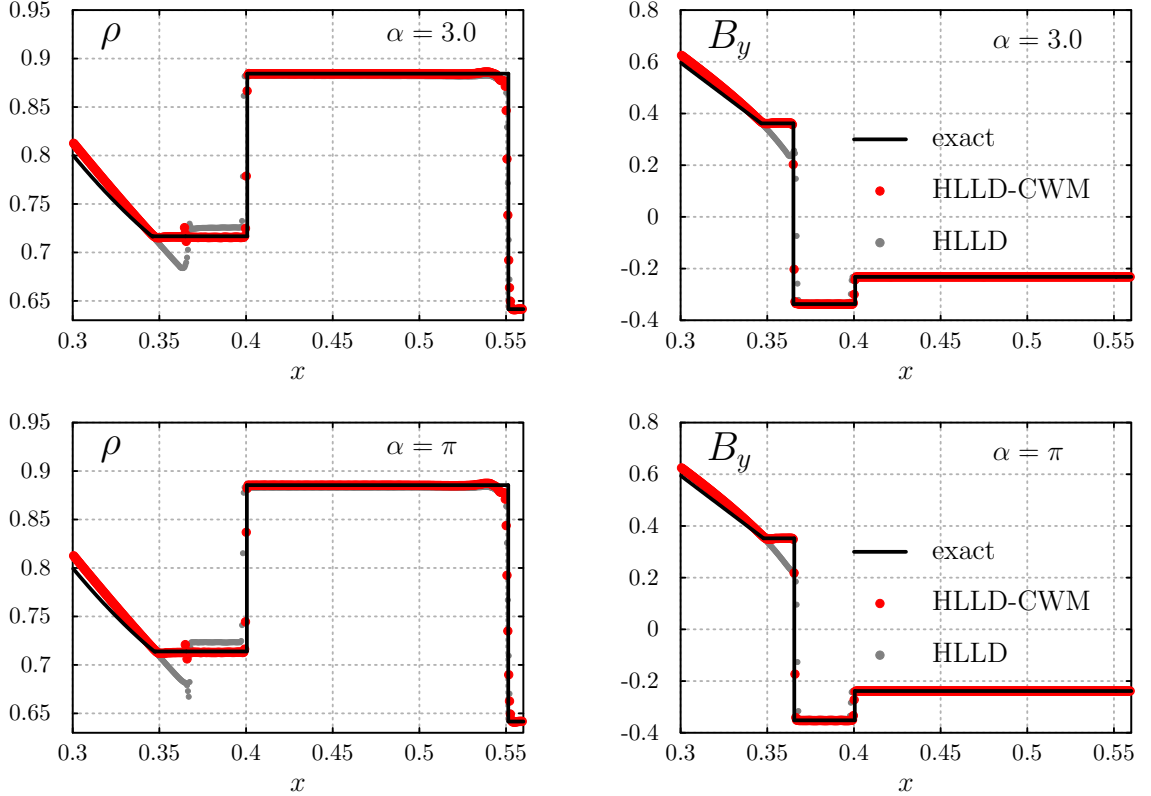


Figure 4.10: The fast rarefaction and rotational discontinuity solution found using HLLD-CWM without the (optional) flux redistribution step, HLLD, and the exact solver using 2048 grid points for (top) a near-coplanar and pseudo-converging case and (bottom) the planar and non-converging (bottom) case.

For Test 6, the solutions of the coplanar and near coplanar cases obtained with $A = 0.05$ using HLLD, and HLLD-CWM without any additional artificial viscosity for 512 grid points are shown in Figure 4.9, and for 2048 grid points are shown in Figure 4.10. The approximate position of the left-going SS is improved with HLLD-CWM for both levels of grid refinement. This test indicates HLLD-CWM performs extremely well for weak intermediate shocks, with minimal error through the transition.

The solution of Test 7 with $A = -0.1$ and 4096 grid points using HLLD, and HLLD-CWM without any additional artificial viscosity is shown in Figure 4.11. The right-going

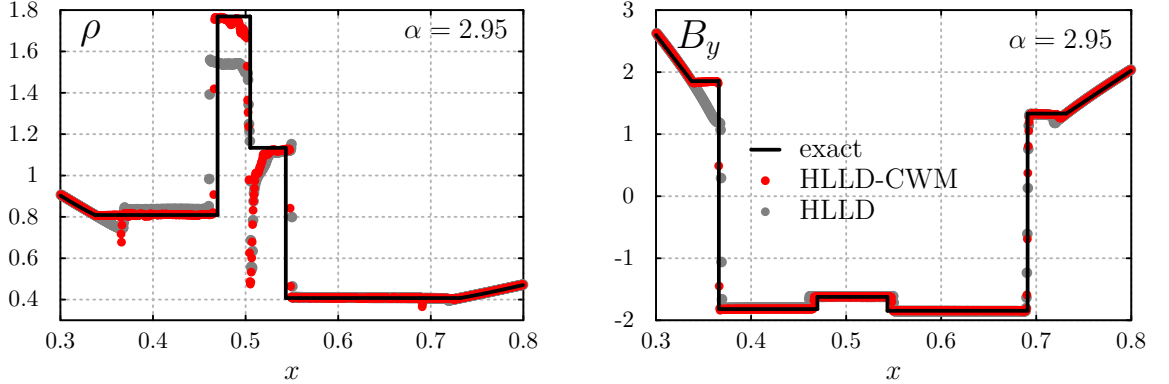


Figure 4.11: Solution consisting of two fast rarefactions and two rotational discontinuities found using HLLD-CWM without the (optional) flux redistribution step, HLLD, and the exact solver using 2048 grid points for the non-planar case.

compound wave is no longer present in either the HLLD or HLLD-CWM solution. A small deviation at $x \approx 0.691$ is present in the CWM solution. This can be eliminated by increasing the threshold value β_T for when CWM is applied. However, if β_T were increased so that CWM was not applied to the right-going compound wave, the error in the approximate solution at the tail of the right-going rarefaction located at $x \approx 0.732$ would increase. This is a desirable property of the CWM method, the adjustment applied is reduced as the compound wave disappears. The jump across the CD is still incorrect with and without CWM, however, the state downstream of the CD is better approximated with CWM because the jump across the left-going SS at $x \approx 0.47$ is more accurate. The maximum value of ρ approximated with CWM is 1.7657 and 1.5596 without it. The percent difference from the exact solution downstream of the CD (row 4 of Table 3.17) is reduced from 12% to 0.2% when CWM is enabled.

Test 7 differs from Tests 5 and 6 in that the base scheme does not approximate the positions of the SS downstream of a CW correctly. The SCW of Tests 5a and 5b removed the SS from the approximate solution. In Tests 6a and 6b, the approximated position of the SS is relatively accurate, although slight improvement is seen when CWM is enabled. In

Test 7, the position of both the left- and right-going SS is incorrect. Although still incorrect, when CWM is enabled, the approximation of the shock positions improves.

The increase in accuracy obtained with CWM was demonstrated with three different test problems. In each case, when CWM was enabled, the jump across and position of each wave affected by pseudo-convergence was more accurately captured. In the next section, the increase in accuracy provided by CWM is quantified with RMSE calculations where CWM is shown to reduce the RMSE for both coplanar and near coplanar cases.

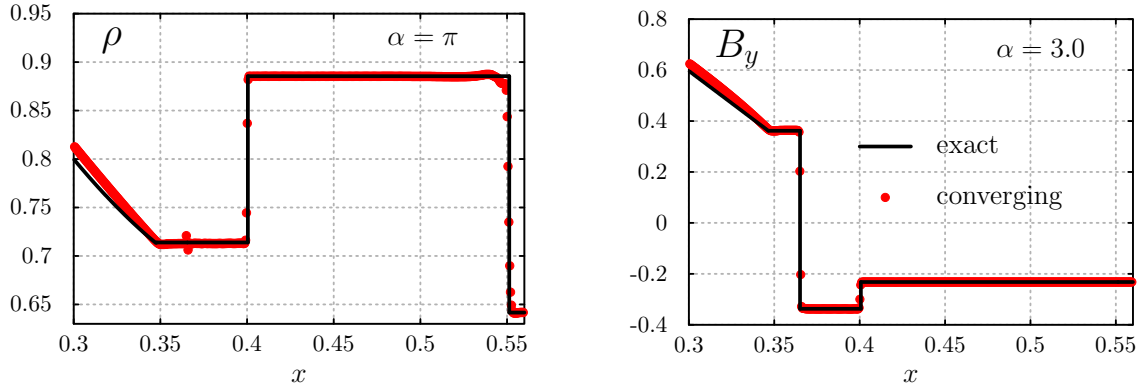


Figure 4.12: The approximate solution after the first flux correction of HLLD-CWM and exact r-solution to the full Riemann problem for the near-coplanar case with 2048 grid points. The compound wave is almost completely removed, except near $x = 0.365$ where a weak intermediate shock remains.

4.2 Error analysis

The appearance of regular structures in the approximate solution is also independent of grid refinement in the region $x = [0.254, 0.481]$ of Figure 4.8 for Test 5 and $x = [0.348, 0.551]$ of Figure 4.10, where the c-solution differs from the r-solution. This is the region between the tail of the left-going fast rarefaction and the right-going contact discontinuity (CD). The region includes either a left-going slow shock and rotational discontinuity or, a slow compound wave for Test 5 or a fast compound wave and slow shock for Test 6.

The RMSE was computed using

$$\text{RMSE} = \sqrt{\sum_{i=1}^M \mathcal{E}_i^2},$$

and

$$\mathcal{E} = \frac{1}{N} \sum_{i=1}^N |U_i - U_{ex}(x_i)|$$

where M is the number of conservative state variables, N is the number of grid points, U_i is an approximated conservative state variable, and U_{ex} is the exact solution for the conservative state variable.

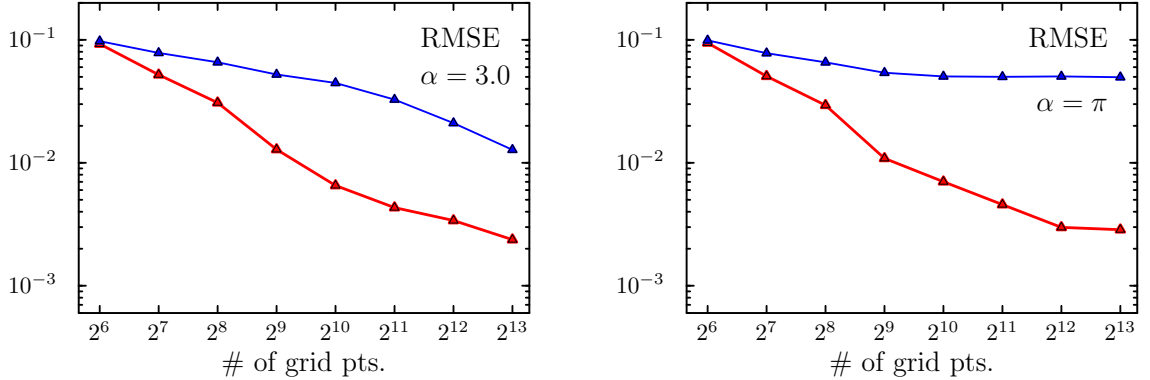


Figure 4.13: RMSE in $x = [0.254, 0.481]$ using HLLD (blue) and HLLD-CWM (red) for Tests (left) 5a and (right) 5b.

The RMSEs of the original HLLD scheme and the modified HLLD-CWM scheme for both the coplanar and near-coplanar cases of Test 5 are shown in Figure 4.13. For the near-coplanar case, a reduction in RMSE through grid refinement occurs with both HLLD and HLLD-CWM. Initially convergence is much quicker with HLLD-CWM. As numerical diffusion is decreased through grid refinement, the compound wave breaks apart and the

convergence rate using HLLD increases at about 2^{10} grid points. For the coplanar case, the RMSE is reduced through grid refinement only when the HLLD-CWM flux is used. Note that the domain used in this analysis differs slightly from $x = [0.2, 0.4]$ used in [36]; the domain used here covers the largest differences between the exact and non-converging solution.

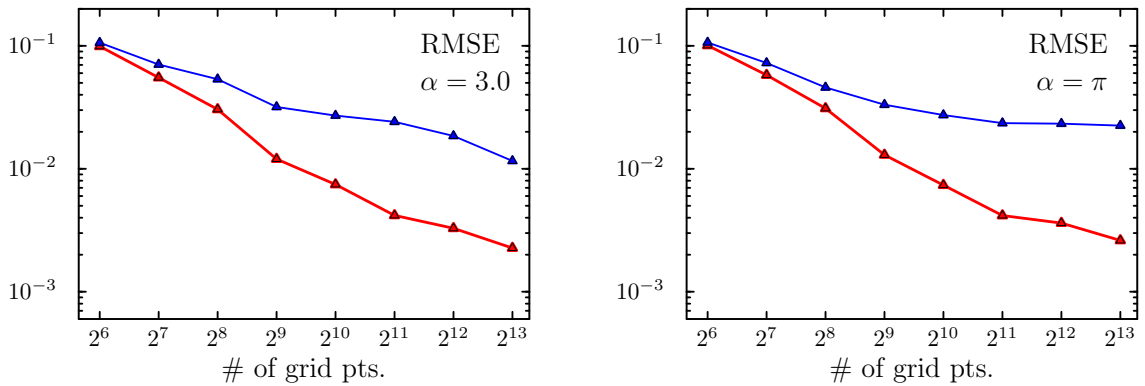


Figure 4.14: RMSE in $x = [0.348, 0.551]$ using HLLD (blue) and HLLD-CWM (red) for Tests (left) 6a and (right) 6b.

The RMSEs of the original HLLD scheme and the modified HLLD-CWM scheme for both the coplanar and near-coplanar cases of Test 6 are shown in Figure 4.14. Unlike Test 5, a regular slow shock is located in the domain in which the RMSEs were computed. The presence of the regular shock is the reason for the initial reduction in error with HLLD for the coplanar case. For the near-coplanar case, a reduction in RMSE through grid refinement occurs with both HLLD and HLLD-CWM. As with Test 5, convergence is faster with HLLD-CWM until between 2^{10} and 2^{11} grid points at which point the rate using HLLD increases at about. For the coplanar case, after the initial convergence, between 2^8 and 2^9 grid points, only HLLD-CWM is able to reduce the RMSE. The CWM should be tested with high order WENO schemes. This has the potential to reduce the need for artificial viscosity downstream of the rotational discontinuity at higher Courant numbers.

The new method known as CWM, which eliminated the compound wave from the solution to coplanar and near coplanar cases at all grid resolutions. The CWM method was shown to localize the effects of a compound wave to the transition layer of a rotational discontinuity while maintaining conservation for a multiple of test problems. For weak intermediate shocks, as in Test 6, the compound wave was removed with minimal error through the transition. In Test 7, CWM was shown to drastically reduce the effects of a compound wave in the presence of other numerical inaccuracies. These results have never been achieved prior to CWM without an exact solver. In the next section, a description of numerical methods for two-dimensional HD and MHD is given. CT is incorporated into the ideal MHD solver to maintain $\nabla \cdot \mathbf{B} = 0$ the machine precision. The process of implementing the solvers for shared memory parallelism is described. Results concluding the GPU out preforms the CPU by two to three times are reported.

Chapter 5: Parallel processing

A description of a new method, known as CWM, which produces an approximate solution to Riemann problems of ideal MHD that contain only regular waves without knowledge of the exact was completed last chapter. The final chapter of this dissertation describes the implementation of a multidimensional flow solver for HD and MHD capable of shared memory parallelism on both a CPU and GPU. An overview of the multidimensional algorithms and grid structure is given. Although the HD solver is relatively unchanged, CT [15] is incorporated into the MHD solver to ensure that $\nabla \cdot \mathbf{B} = 0$ throughout the simulation (assuming it was initially zero). Important concepts for parallel programming on shared memory devices, e.g., avoiding memory contention, are described. A performance comparison of parallel execution for three multidimensional test problems of HD and MHD is given. We find a performance increase of seven times for the GPU over the CPU.

5.1 Methods for ideal MHD in higher dimensions

Care must be taken in multidimensional MHD simulations to ensure errors associated with $\nabla \cdot \mathbf{B}$ do not grow large enough to introduce numerical instabilities. A number of different approaches have been devised to contain the growth of $\nabla \cdot \mathbf{B}$. A brief description of a few of the more popular approaches is given below. For a thorough review and a performance comparison of the schemes discussed below, see [38].

Powell et al. [26] derived the following non-conservative set of form of (2.34) - (2.37) where source terms proportional to $\nabla \cdot \mathbf{B}$ are added to the right-hand side

$$\frac{\partial \rho}{\partial t} + \nabla \cdot (\rho \mathbf{v}) = 0 , \quad (5.1)$$

$$\frac{\partial(\rho \mathbf{v})}{\partial t} + \nabla \cdot \left[\rho \mathbf{v} \otimes \mathbf{v} + \left(p_g + \frac{B^2}{2} \right) \mathbf{I} - \mathbf{B} \otimes \mathbf{B} \right] = -\mathbf{B}(\nabla \cdot \mathbf{B}) , \quad (5.2)$$

$$\frac{\partial E}{\partial t} + \nabla \cdot \left[\left(E + p_g + \frac{B^2}{2} \right) \mathbf{v} - \mathbf{v} \cdot \mathbf{B} \otimes \mathbf{B} \right] = -\mathbf{v} \cdot \mathbf{B}(\nabla \cdot \mathbf{B}) , \text{ and} \quad (5.3)$$

$$\frac{\partial \mathbf{B}}{\partial t} + \nabla \cdot [\mathbf{v} \otimes \mathbf{B} - \mathbf{B} \otimes \mathbf{v}] = -\mathbf{v}(\nabla \cdot \mathbf{B}). \quad (5.4)$$

It is known as the eight-wave scheme with the eighth wave corresponding to the propagation of $\nabla \cdot \mathbf{B}$.

Brackbill and Barnes [4] introduced a corrective step for \mathbf{B} where the updated solution is projected to one that is divergence free. The so-called projection scheme corrects the updated magnetic field by subtracting the scalar potential associated with the updated field. This is done by writing the updated solution \mathbf{B}^* as the sum of the curl and gradient of the vector and scalar potentials,

$$\mathbf{B}^* = \nabla \times \mathbf{A} + \nabla \phi. \quad (5.5)$$

The correction of (5.5) is found by taking the curl of both sides and solving the resulting Poisson equation

$$\nabla^2 \phi = \nabla \cdot \mathbf{B}^*. \quad (5.6)$$

The solution of (5.6) is then subtracted from \mathbf{B}^* to give the advanced the magnetic field as

$$\mathbf{B}^{n+1} = \mathbf{B}^* - \nabla \phi. \quad (5.7)$$

In order for $\nabla \cdot \mathbf{B}^{n+1} = 0$, the Laplacian of (5.6) must be calculated as the divergence of the gradient.

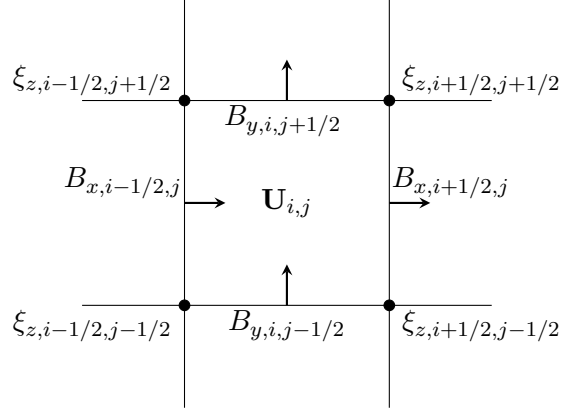


Figure 5.1: Staggered field geometry of the constrained transport scheme. The components of the magnetic field are located at the cell interfaces, ξ_z is located at the cell corners.

The final approach discussed here, and the one implemented for this dissertation, is the CT method of Evans and Hawley [15]. For CT, the $\nabla \cdot \mathbf{B} = 0$ is maintained by staggering the grid with the magnetic field components placed at the cell interfaces. The electromotive force $\mathbf{E} = -\mathbf{v} \times \mathbf{B}$ is defined along the edges in three-dimensions and at the cell corners in two-dimensions. Following the notation of [32], the z-component of the electromotive force is denoted ξ_z . The placement of \mathbf{B} and ξ_z in two-dimensions is shown in Figure 5.1, with B_x place at $x_{i+1/2}, y_j$ and B_y place at $x_i, y_{j+1/2}$. The integration is done along cell edges in terms of finite areas instead of finite volumes. The updated magnetic field components are

$$B_{x,i+1/2,j}^{n+1} = B_{x,i+1/2,j}^n - \frac{\delta t}{\delta y} (\xi_{z,i+1/2,j+1/2} - \xi_{z,i+1/2,j-1/2}), \text{ and} \quad (5.8)$$

$$B_{y,i,j+1/2}^{n+1} = B_{y,i,j+1/2}^n + \frac{\delta t}{\delta x} (\xi_{z,i+1/2,j+1/2} - \xi_{z,i-1/2,j-1/2}). \quad (5.9)$$

Due to perfect cancellation, the numerical divergence in the cell

$$(\nabla \cdot \mathbf{B})_{i,j} = \frac{1}{\delta x} (B_{x,i+1/2,j} - B_{x,i-1/2,j}) + \frac{1}{\delta y} (B_{y,i,j+1/2} - B_{y,i,j-1/2}) \quad (5.10)$$

remains zero after the solution is updated.

The electromotive forces are initially calculated at the faces and must be integrated to the corners. Gardiner and Stone [18] argued that simple averaging across the faces will produce incorrect results for plane-parallel grid aligned flows and proposed an upwind method. They gave the emfs at the cell corner as

$$\xi_{z,i+1/2,j+1/2} = \frac{1}{4} (\xi_{z,i+1/2,j} + \xi_{z,i+1/2,j+1} + \xi_{z,i,j+1/2} + \xi_{z,i+1,j+1/2}) \quad (5.11)$$

$$+ \frac{\delta y}{8} \left(\left(\frac{\partial \xi_z}{\partial y} \right)_{i+1/2,j+1/4} - \left(\frac{\partial \xi_z}{\partial y} \right)_{i+1/2,j+3/4} \right) \quad (5.12)$$

$$+ \frac{\delta x}{8} \left(\left(\frac{\partial \xi_z}{\partial x} \right)_{i+1/4,j+1/2} - \left(\frac{\partial \xi_z}{\partial x} \right)_{i+3/4,j+1/2} \right). \quad (5.13)$$

The derivatives of the emf, $\partial \xi_z / \partial y$ ($\partial \xi_z / \partial x$), at the x (y) interfaces are upwinded based on the contact mode. In [18], they are given as

$$\left(\frac{\partial \xi_z}{\partial y} \right)_{i+1/2,j+1/4} = \begin{cases} \left(\frac{\partial \xi_z}{\partial y} \right)_{i,j+1/4} & \text{if } v_{n,i-1/2,j} > 0, \\ \left(\frac{\partial \xi_z}{\partial y} \right)_{i+1,j+1/4} & \text{if } v_{n,i+1/2,j} < 0, \\ \frac{1}{2} \left(\left(\frac{\partial \xi_z}{\partial y} \right)_{i,j+1/4} + \left(\frac{\partial \xi_z}{\partial y} \right)_{i+1,j+1/4} \right) & \text{otherwise.} \end{cases} \quad (5.14)$$

The derivatives are

$$\left(\frac{\partial \xi_z}{\partial y} \right)_{i,j-1/4} = \frac{\xi_{z,i,j}^r - \xi_{z,i,j-1/2}}{2\delta y}. \quad (5.15)$$

where $\xi_{z,i,j}^r$ is a reference emf computed at the cell center, see Figure 5 of [32]. Similar

expressions can be obtained for $\partial\xi_z/\partial x$.

The steps of the two-dimensional algorithm are given as follows:

1. Calculate the fluxes at each interface replacing the normal component of the magnetic field at cell center with the value at the interface.
2. Calculate the emfs at the cell corners using the algorithm described above.
3. Calculate the reference field $\xi_{i,j}^r$ at the cell centers.
4. Update the hydrodynamical conserved variables and B_z at the cell centers.
5. Update the magnetic field at each interface using CT.
6. Calculate the normal and tangential components of the cell-centered magnetic field as the average of the interface values.
7. Advance the solution in time.
8. Apply higher order extension.
9. Update the solution.
10. Calculate new time step and repeat steps 1-9 until stopping criteria is met.

In the next section, a detailed description is given of how the one- and two-dimensional algorithms are implemented for this dissertation to run in parallel on shared memory processors.

5.2 Shared memory parallelism

Shared memory parallelism refers to simultaneous execution on a common section of memory. It was implemented for this dissertation using Thrust, a C++parallel template library based on the Standard Template Library (STL). It supports four device backends: CUDA, OMP, TBB, and the standard C++device for serial runs. The CUDA backend utilizes the

GPU, while the OMP and TBB backends utilize multi-core processing on the CPU. This dissertation compares the performance of the the CUDA and OMP backends.

It is essential that there is no overlap of memory access of the different threads. In fluid dynamics, this done by what is termed *coloring* the faces/edges. Coloring refers to grouping the faces/edges, i.e., coloring them, so that no two members of the group need to access the same memory space for the calculations. For FV schemes, an iteration over the faces in serial becomes an iteration over the colors and the corresponding faces in parallel.

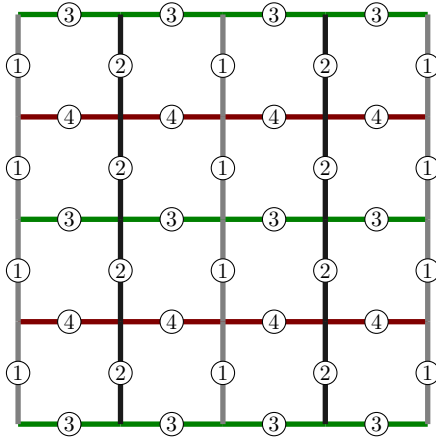


Figure 5.2: Colored grouping of interior faces for avoiding memory contention with cell centered finite volume schemes. Four groups, labeled 1-4, are required.

A possible coloring, and the one implemented for this dissertation, of the interior faces for cell-centered FV schemes is shown in Figure 5.2. For each loop, the flux at the face is calculated and the residual at the cells is built by adding the contribution of each face. Coloring ensures two faces will not attempt to update the residual of a cell simultaneously.

Coloring is more complicated when CT is used in conjunction with a cell-centered FV scheme. In this case, each loop over the faces consists of a contribution to the residual at the cell center and a contribution to the emf at the cell corner. Not only accessing the same cell, but also the same point must be avoided. The coloring scheme shown in Figure 5.2 only avoids one these potential pitfalls, because the faces/edges of each group can access

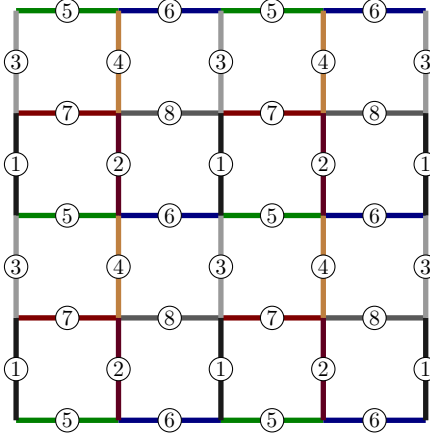


Figure 5.3: Colored grouping of interior faces for avoiding memory contention with cell centered finite volume schemes plus constrained transport. Eight groups, labeled 1-8, are required.

the same point simultaneously. An alternative coloring scheme is shown in Figure 5.3 where eight colors are used instead of four. In this case, the faces and the edges are colored, this is equivalent to doubling the amount of colors for the faces since edges and faces are the same in two-dimensions.

5.3 Efficient algorithms

This section discusses increasing parallel performance with efficient data storage and utilization computational power. Two types of data storage are AoS and SoA. With limited memory available on the GPU, it is important to limit data storage. This is achieved through function composition, or operator fusion.

The goal of operator fusion is to reduce storage of temporary data for similar operations. As an example, consider the two transformations, $f(x)$ and $g(f(x))$ [19].

```

thrust::device_vector<float> x(n); // independent variable
thrust::device_vector<float> y(n); // y = f(x)
thrust::device_vector<float> z(n); // z = g(y)

// compute y = f(x)

```

```

    thrust::transform(x.begin(), x.end(), y.begin(), f());

    // compute z = g(y)
    thrust::transform(y.begin(), y.end(), z.begin(), g());

```

The above example requires storage of $3n$ floats, $2n$ reads, $2n$ writes, and uses n temporary floats. The operations can be fused by using transform iterators.

```

thrust::device_vector<float> x(n); // independent variable
thrust::device_vector<float> z(n); // z = g(y) = g(f(x))

// compute z = g(f(x))
thrust::transform(make_transform_iterator(x.begin(), f()),
                 make_transform_iterator(x.end(), f()),
                 z.begin(),
                 g());

```

Using `transform_iterators` reduces the storage requirements to $2n$ floats, n reads, n writes, and no temporary storage. As another example, consider initializing the cell-centered variables for an HD shock tube problem in one-dimension. The initial discontinuity is given by `discontinuity_position` and the initial left and right states are given in primitive variables by the tuples of floats `state_l` and `state_r` respectively. The inefficient method for initializing the cell centers with conservative state variables is given below.

```

// type definitions
typedef thrust::device_vector<float, float> Point; // (x, y)
typedef thrust::device_vector<float, float, float> Vector; // (d, mx, E)
typedef thrust::device_vector<Point> PointArray; // SoA
typedef thrust::device_vector<Vector> VectorArray; // SoA

int n; // number of cells
float discontinuity_position;
PointArray cell_positions(n);
VectorArray primitive_states(ncell);
VectorArray conservative_states(n);

// compute cell positions
thrust::transform_n(thrust::make_counting_iterator(0),
                   n,
                   cell_positions.begin(),
                   cells_initialize());

// set state of cell based on position
thrust::transform_n(cell_positions.begin(),
                   cell_positions.size(),

```

```

        primitive_states.begin(),
        shock_tube_initialize(discontinuity_postion,
                               state_l,
                               state_r));

// convert primitive variables to conservative variables
thrust::transform_n(primitive_states.begin(),
                    primitive_states.size(),
                    conservative_states.begin(),
                    convert_primitive_to_conservative());

```

The storage of the cell positions and primitive variables is eliminated using the `make_transform_iterator` as follows

```

// type definitions
typedef thrust::device_vector<float, float, float> Vector; // (d, mx, E)
typedef thrust::device_vector<Vector> VectorArray; // SoA

int n;
float discontinuity_postion;
VectorArray conservative_states(n);

// set conservative state at cell center based on position
thrust::transform_n(make_transform_iterator(
    make_transform_iterator(
        make_device_counting_iterator(),
        cells_initialize()),
    shock_tube_initialize(discontinuity_postion,
                           state_l,
                           state_r)),
    ncell(),
    conservative_states.begin(),
    convert_primitive_to_conservative());

```

see Appendix B for the definitions of `transform_n` and `make_device_counting_iterator`.

By fusing the transformations, the need to store $5n$ floats was eliminated, the number of reads and writes was reduced by $5n$, and no temporaries were stored. The storage requirements are reduced by $10n$ in the case of multi-dimensional MHD. Transform iterators help reduce the amount of stored data, however, it is important to properly store the remaining data to achieve memory coalescing.

Memory coalescing occurs when multiple memory addresses are accessed with a single transaction. A warp is 32 consecutive threads on the GPU. It can access 128 bytes, i.e., 32

single precision values, with one transaction. If memory is uncoalesced, multiple transactions are required to load 128 bytes. Coalescing does not occur when data is stored with AoS, it will however, with SoA. Below is an example of a structure containing one-dimensional hydrodynamic state variables.

```
struc conservative_variables{
    float density;
    float momentum_x;
    float energy;
}

conservative_variables *state; // AoS

state[i].density = some_number;
state[i].momentum_x = another_number;
state[i].energy = one_more_number;
```

To ensure memory is coalesced, the variables need to be stored in an SoA, as shown below.

```
struc conservative_variables{
    float *density;
    float *momentum_x;
    float *energy;
}

conservative_variables state; // SoA

state.density[i] = some_number;
state.momentum_x[i] = another_number;
state.energy[i] = one_more_number;
```

Memory coalescing can be achieved with thrust through the use of the `zip_iterator`. It creates tuples from arrays on the fly. Converting from primitive variables to conservative variables using the slower AoS approach is shown below.

```
struc convert_primitive_to_conservative
    : public thrust::unary_function<primitive_variables,
                                         conservative_variables>
{
    float _gamma;

    convert_primitive_to_conservative(float gamma)
        : _gamma(gamma) {}

    __host__ __device__
    conservative_variables operator()(const primitive_variables& pstate)
```

```

    float half = 1.0f/2.0f;
    float d = pstate.density;
    float vx = pstate.velocity_x;
    float pg = pstate.pressure_gas;

    float density = d;
    float momentum_x = d*vx;
    float energy = pg/(1.0f - this->_gamma) + half*d*vx*vx;

    return make_conservative_variables(density,momentum_x,energy);
}

thrust::device_vector<primitive_variables> pstate(n); // AoS
thrust::device_vector<conservative_variables> state(n); // AoS
thrust::transform_n(pstate.begin(),
                    pstate.size(),
                    state.begin(),
                    convert_primitive_to_conservative(gamma));

```

The faster SoA approach using the `zip_operator` is shown below.

```

struct convert_primitive_to_conservative
: public thrust::unary_function<tuple<float,float,float>,
  tuple<float,float,float>>
{
    float _gamma;

    convert_primitive_to_conservative(float gamma)
: _gamma(gamma) {}

__host__ __device__
tuple<float,float,float>operator()(const tuple<float,float,float>& pstate)

    float half = 1.0f/2.0f;
    float d = thrust::get<0>(pstate);
    float vx = thrust::get<1>(pstate);
    float pg = thrust::get<2>(pstate);

    float density = d;
    float momentum_x = d*vx;
    float energy = pg/(1.0f - this->_gamma) + half*d*vx*vx;

    return make_tuple(density,momentum_x,energy);
}

thrust::device_vector<float> d(n),vx(n),pg(n);
thrust::device_vector<float> mx(n),en(n);
thrust::transform_n(thrust::make_zip_iterator(make_tuple(d.begin(),
                                                       vx.begin(),
                                                       pg.begin())),
                  n,

```

```

    thrust::make_zip_iterator(make_tuple(d.begin(),
                                         mx.begin(),
                                         en.begin())),
    convert_primitive_to_conservative(gamma));

```

The algorithms and techniques discussed above have been implemented in an multidimensional hydrodynamic and ideal magnetohydrodynamic solver capable of shared memory parallelism. In the following section, the accuracy and performance of the code is demonstrated on some well known test problems, namely Kelvin-Helmholtz instability, spherical blast waves, and Orzag-Tang vortex.

5.4 Performance results

In Section 5.2 performance enhancing techniques such as operator fusion and SoA data storage were described. The algorithms described in Section 5.1 were implemented in an edge-based finite-volume flow solver. The performance results on a Dell Precision 7500 workstation with a (Dual CPU) Intel Xeon E5645 @ 2.40 Ghz and a GeFroce GTX TITAN GPU with a memory bandwidth of 288.4 GB/sec and 2688 CUDA cores are given for three test cases, the Kelvin-Helmholtz instability, spherical blast waves, and Orzag-Tang vortex. In all three tests, we use the initial conditions of [30] for comparison purposes.

The Kelvin-Helmholtz instability [6] considers a slip surface, i.e., a discontinuity between oppositely directed flows. The version of the test considered here is identical to the version given by Stone et al. [30]. The simulation is performed on a square domain, $[0, 1] \times [0, 1]$, with periodic boundaries everywhere. The flow speed is 0.5; it is in the $-x$ direction for $y < 0.25$ and $y > 0.75$, where $\rho = 1$, and in the x direction for $0.25 \leq y \leq 0.75$, where $\rho = 2$. The gas pressure is initially 2.5 everywhere and the ratio of specific heats is $\gamma = 1.4$. The instability is produced by adding random perturbations with a peak amplitude of 0.01 to both the x and y velocities.

The density at times $t = 1$ and $t = 5$ is shown in the top and bottom panels of Figure 5.4 respectively. The initial conditions are shown in Figure C of Appendix C. The boundary between the two fluids is well resolved at later times, this indicates numerical diffusion is not

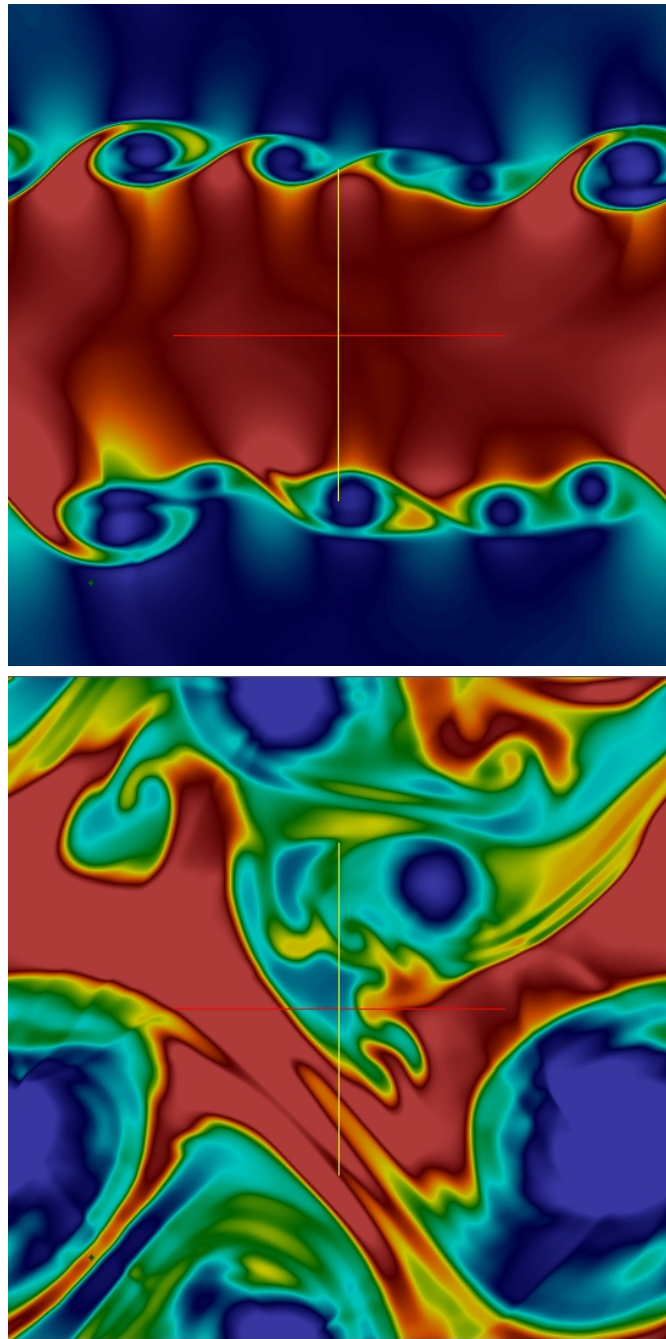


Figure 5.4: The Kelvin-Helmholtz instability, ρ at times: $t = 1$ (top) and $t = 5$ (bottom). Simulation performed on a 400×400 grid of triangular elements with code written for this dissertation available at: <https://github.com/akercher/dissertation>.

excessive. If excessive numerical diffusion were present, the instability would be suppressed [30].

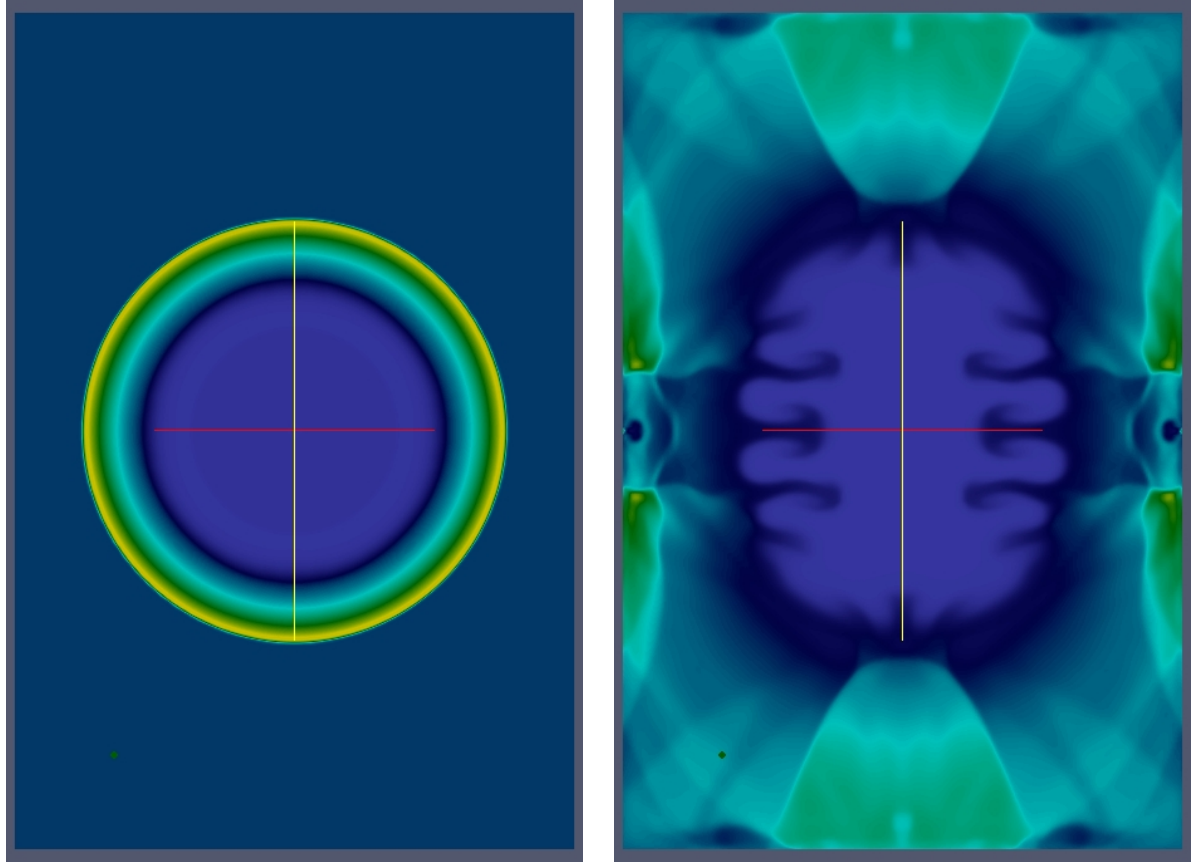


Figure 5.5: Spherical blast waves at times: $t = 0.2$ (left) and $t = 1.75$ (right). Simulation performed on a 400×600 grid of quadrilateral elements with code written for this dissertation available at: <https://github.com/akercher/dissertation>.

For second case, a spherical blast wave is simulated on a rectangular domain with $L_y = 3L_x/2$ and periodic boundary conditions [39, 1, 23]. The problem is initialized with a high pressure region corresponding to $r < 0.1$ where the gas pressure is two orders of magnitude greater than the background pressure. A uniform density of $\rho = 1$ is used throughout the domain; the background gas pressure is 0.1; the ratio of specific heats is $\gamma = 5/3$.

The density at times $t = 0.2$ and $t = 1.5$ is shown in the left and right panels of Figure 5.5 respectively. The blast wave is initially spherical as there are no effects due to grid alignment. As the blast reaches the boundaries, complex interactions between linear and nonlinear waves are produced and solution remains symmetric across the x and y axis.

The Orszag-Tang vortex [25] has been extensively studied and used for comparisons to previous results. The simulation is performed on a square domain, $[0, 1] \times [0, 1]$, with periodic boundaries everywhere. The density, $\rho = 25/(36\pi)$ and pressure, $5/(12\pi)$ are constant throughout the domain. The initial velocities are $v_x = -\sin(2\pi y)$ and $v_y = \sin(2\pi x)$; the initial magnetic field is defined in terms of the magnetic vector potential, $A_z = B_0 (\cos(4\pi x)/(4\pi) + \cos(2\pi x)/(2\pi))$, where $B_0 = 1/\sqrt{4\pi}$; the ratio of specific heats is $\gamma = 5/3$.

Table 5.1: Performance comparison of GPU and CPU.

grid size	KH-Instability	Blast Waves	Orszag-Tang
64×64	5	5	5
128×128	19	19	22
256×256	58	58	60
512×512	75	75	79
1024×1024	81	81	86

Performance comparisons between the GPU and CPU for the three test cases described above are listed in Table 5.1. The CPU has six physical cores and two logical cores per physical, making 12 cores available with hyper-threading enabled. Assuming near perfect scaling, running on the GPU is approximately seven times faster than running in parallel on the CPU. A larger increase in performance of the GPU over the CPU is observed in the MHD test as compared to the HD tests. The MHD equations are more complex than the HD equations and more calculations are required per time step. The performance increase demonstrates the superior ability of the GPU to process many operations simultaneously.

The results indicate that the cost to performance ratio for a GPUs such as NVIDIAs GTX Titan, which retails for about \$1000.00, is such that they are an ideal choice for shared memory processors, if the limited memory is managed properly. The relatively large memory capacity of 6 GB on the GTX Titan is around 6.5% of the 92 GB available on the Xeon E5. For the equivalent memory of one, Xeon E5, fifteen GPUs are required, costing nearly three times that of one Xeon E5. In order for GPUs to be worth the investment, computations on the fly must be maximized and data storage minimized.

Chapter 6: Conclusion

This dissertation contributed to the computational physics and space weather communities in numerous ways. New benchmarks for ideal MHD code validation were provided in Section 3.3. The benchmarks were produced with code written for this dissertation which implemented the method described in Section 2.6.3. The availability of nonlinear solver is a significant contribution to the computational physics and space weather communities since it can be used for benchmarking or incorporated into flow solvers for flux evaluations.

Entirely new work was presented in Chapter 4. A modification to the finite volume method can be used to produce the correct solutions to non-unique Riemann problems of ideal MHD equations. The properties of the planar ideal MHD equations discussed in [16] were used to describe the appearance of compound wave structures in finite volume approximations. The solution can be modified near a large rotation ($\beta_T > 2.0$) in order for the upstream and downstream states to satisfy the jump conditions of a rotational discontinuity. The method may be well suited for simulations in two- and three-dimensions because it does not track the rotational discontinuity.

The CWM method also achieves true convergence for problems with initial conditions near those with a non-unique solution. It is the first flux approximation for a dissipative finite volume scheme that does not exhibit pseudo-convergence. The number of grid points required to obtain RMSEs on the order of 10^{-2} is reduced by nearly two orders of magnitude for both the near coplanar case containing a SCW and the case containing a FCW.

The CWM method can be applied in simulations on a wide range of spatial scales, but it is best suited for large-scale simulations for two reasons: smoothing oscillations caused by over-shoots downstream of the Alfvén wave is required for small scale simulations and the greatest reduction in L^1 -errors are achieved at lower resolutions.

The CWM method should be tested with other methods of approximating numerical fluxes in FVMs. For Roe-type methods that use solutions to the linearized system of equations, the intermediate states can be approximated as linear combinations of the eigenvalues and eigenvectors of the Jacobian (Eq. 3.19, [28]). The HLLD method is convenient to use with the CWM method because it gives the exact solution to an isolated rotational discontinuity [24] and its intermediate states provide an initial guess that results in a high rate of convergence when a nonlinear solver is used. If a nonlinear solver is used, more frequent calls may be required for problems in two- and three- dimensions. In this case, reducing the number of iterations can decrease computational costs without a loss in accuracy of the final solution. It is important to stress that the results of Chapter 4 were obtained exclusively with the HLLD approximate Riemann solver in conjunction with CWM. Although a nonlinear solver may potentially improve the accuracy of CWM, it is not required. That is a unique property of CWM and another reason why, along with improved accuracy and the potential for simulations in higher dimension, its development is a substantial contribution to the computational physics and space weather communities.

The new results of Section 3.3 and Chapter 4 were bookended by the development of a multidimensional fluid solver capable of running in parallel on shared memory processors. This code was developed to test the viability of using a GPU as the primary device for shared memory parallelism in place of the CPU. The GPU was shown to outperform the CPU by two to three times. Essential algorithms such as face coloring were explained for cell center FV with and without CT. It was argued that the cost to performance ratio for a GPUs such as NVIDIAAs GTX Titan is worth the investment as long as the reduction in available memory from the CPU is handled effectively. This dissertation described and implemented operator fusion to reduce memory requirements and SoA data storage to increase performance on the GPU. This fluid solver, which is capable of shared memory parallelism along with the accompanying description within this dissertation can be used as a blueprint or benchmark by anyone looking to incorporate GPUs to increase solver performance, making it a significant contributions to the computational physics and space

weather communities.

Appendix A: Derivation of HLL fluxes

The integral average over the Riemann fan: $[x_l, x_r] \times [0, t]$ is found with the conservation law

$$\int_{x_l}^{x_r} \mathbf{U}(x, t) dx - \int_{x_l}^{x_r} \mathbf{U}(x, 0) dx + \int_0^t \mathbf{F}(\mathbf{U}(x_r, t')) dt' - \int_0^t \mathbf{F}(\mathbf{U}(x_l, t')) dt' = 0. \quad (\text{A.1})$$

Integrating and subtracting the last terms of equation (A.1) gives

$$\int_{x_l}^{x_r} \mathbf{U}(x, t) dx = x_r \mathbf{U}_r - x_l \mathbf{U}_l + t(\mathbf{F}_l - \mathbf{F}_r). \quad (\text{A.2})$$

Substituting $x_l = tS_l$, $x_r = tS_r$, into (A.2) and dividing it by $t(S_r - S_l)$, gives the integral average

$$\frac{1}{t(S_r - S_l)} \int_{x_l}^{x_r} \mathbf{U}(x, t) dx = \frac{S_r \mathbf{U}_r - S_l \mathbf{U}_l + \mathbf{F}_l - \mathbf{F}_r}{S_r - S_l}. \quad (\text{A.3})$$

The HLL intermediate state, \mathbf{U}^* , is defined as the intergral average given above in (A.3).

The HLL fluxes are found by integrating over the left or right half of the Riemann fan. Integration over the right half, $[0, x_r] \times [0, t]$, and dividing by t , gives

$$\frac{1}{t} \int_0^{x_r} \mathbf{U}(x, t) dx = S_r \mathbf{U}_r + \mathbf{F}_r - \mathbf{F}^*. \quad (\text{A.4})$$

Rearranging (A.4), and approximating the integral of the left hand side with (A.4), gives

$$\mathbf{F}^* = \frac{S_r \mathbf{F}_l - S_l \mathbf{F}_r + S_r S_l (\mathbf{U}_l - \mathbf{U}_r)}{S_r - S_l}. \quad (\text{A.5})$$

Appendix B: Thrust templates

Below are `transform_n` templates for unary and binary functors, as well as the inline function `make_device_counting_iterator` [A. Corrigan, private correspondence]. The type `Struct` is being iterated over when used in conjunction with `make_device_counting_iterator`.

```
namespace thrust
{
    template<typename InputIterator,
              typename Size,
              typename OutputIterator,
              typename UnaryFunction>
    OutputIterator transform_n(InputIterator first, Size n,
                               OutputIterator result,
                               UnaryFunction op)
    {
        return transform(first, first+n, result, op);
    }

    template<typename InputIterator1,
              typename Size,
              typename InputIterator2,
              typename OutputIterator,
              typename BinaryFunction>
    OutputIterator transform_n(InputIterator1 first1, Size n,
                               InputIterator2 first2,
                               OutputIterator result,
                               BinaryFunction op)
    {
        return transform(first1, first1+n, first2, result, op);
    }
}

//end namespace

typedef int Index;
typedef thrust::device_vector<Struct>::iterator StructIterator;
typedef thrust::iterator_system<StructIterator>::type device_iterator_system
;
typedef thr::counting_iterator<Index, device_iterator_system>
device_counting_iterator;

inline device_counting_iterator make_device_counting_iterator(Index start=
Index(0)) { return device_counting_iterator(start); }
```

Appendix C: Kelvin-Helmholtz instability initial conditions

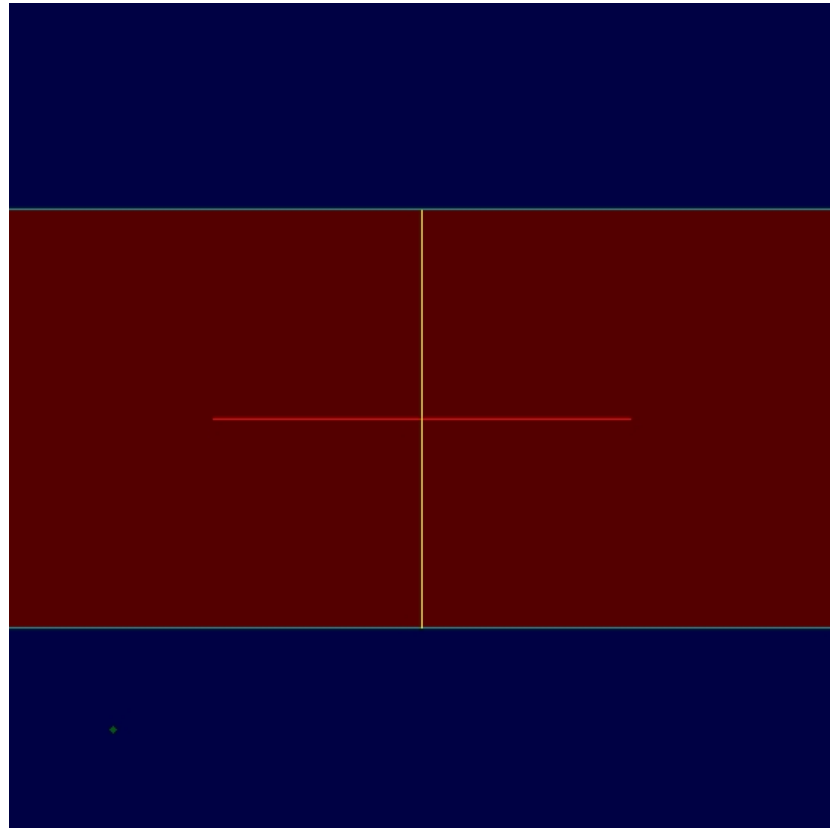


Figure C.1: Initial conditions of the Kelvin-Helmholtz instability problem. See Section 5.4 for solutions at times $t=1$ and $t=5$.

Bibliography

- [1] D.S. Balsara, D.S. Spicer, *J. Comp. Phys.* 149 (1999) 270–292.
- [2] A.A. Barmin, A.G. Kulikovskiy, N.V. Pogorelov, *J. Comp. Phys.* 126 (1996) 77–90.
- [3] P. Batten, N. Clarke, C. Lambert, C.D. M., *SIAM J. Sci. and Stat. Comp.* 18 (1997) 1553–1570.
- [4] J.U. Brackbill, D.C. Barnes, *J. Comp. Phys.* 35 (1980) 426–430.
- [5] M. Brio, C.C. Wu, *J. Comp. Phys.* 75 (1988) 400–422.
- [6] S. Chandrasekhar, *Hydrodynamic and hydromagnetic stability*, Dover classics of science and mathematics, Dover Publications, cop. 1961, New York, 1981.
- [7] J.K. Chao, L.H. Lyu, B.H. Wu, A.J. Lazarus, T.S. Chang, R.P. Lepping, *J. Geophys. Res.* 98 (1993) 17443–17450.
- [8] P. Colella, P.R. Woodward, *J. Comp. Phys.* 54 (1984) 174–201.
- [9] W. Dai, P.R. Woodward, *J. Comp. Phys.* 111 (1994) 354–372.
- [10] S.F. Davis, *SIAM J. Sci. and Stat. Comput.* 9 (1988) 445–473.
- [11] H. de Sterck, B.C. Low, S. Poedts, *Physics of Plasmas* 5 (1998) 4015–4027.
- [12] H. de Sterck, S. Poedts, *Physical Review Letters* 84 (2000) 5524–5527.
- [13] B. Einfeldt, *SIAM J. Numer. Anal.* 25 (1988) 294–318.
- [14] B. Einfeldt, P.L. Roe, C.D. Munz, B. Sjogreen, *J. Comp. Phys.* 92 (1991) 273–295.

- [15] C.R. Evans, J.F. Hawley, ApJ 332 (1988) 659–677.
- [16] S.A.E.G. Falle, S.S. Komissarov, J. Plasma Phys. 92 (2001) 29–56.
- [17] H. Feng, J.M. Wang, Solar Phys. 247 (2008) 195–201.
- [18] T.A. Gardiner, J.M. Stone, Journal of Computational Physics 205 (2005) 509–539.
- [19] J. Hoberock, N. Bell, Thrust: A parallel template library, 2010. Version 1.7.0.
- [20] A. Jeffrey, Magnetohydrodynamics, London: Oliver & Boyd, 1966.
- [21] A. Jeffrey, T. Taniuti, Non-linear wave propagation, 1964.
- [22] L.D. Landau, E.M. Lifshitz, L.P. Pitaevskii, Electrodynamics of continuous media, 3rd edition, 1984.
- [23] P. Londrillo, L. Del Zanna, ApJ 530 (2000) 508–524.
- [24] T. Miyoshi, K. Kusano, J. Comp. Phys. 208 (2005) 315–344.
- [25] S.A. Orszag, C.M. Tang, Journal of Fluid Mechanics 90 (1979) 129–143.
- [26] K.G. Powell, P.L. Roe, T.J. Linde, T.I. Gombosi, D.L. de Zeeuw, J. Comp. Phys. 154 (1999) 284–309.
- [27] P.L. Roe, J. Comp. Phys. 43 (1981) 357–372.
- [28] D. Ryu, T.W. Jones, ApJ 442 (1995) 228–258.
- [29] G.A. Sod, J. Comp. Phys. 27 (1978) 1–31.
- [30] J. Stone, T. Gardner, P. Teuben, Athena mhd code project, <https://trac.princeton.edu/Athena/>, 2010.
- [31] J.M. Stone, T. Gardiner 14 (2009) 139–148.

- [32] J.M. Stone, T.A. Gardiner, P. Teuben, J.F. Hawley, J.B. Simon, *The Astrophysical Journal Supplement Series* 178 (2008) 137–177.
- [33] E.F. Toro, *Riemann solvers and numerical methods for fluid dynamics : a practical introduction*, Springer, Berlin, New York, 2nd edition, 1999.
- [34] E.F. Toro, M. Spruce, W. Speares, *Shock Waves* 4 (1994) 25–34.
- [35] M. Torrilhon, in: Zurich: Seminar for Applied Mathematics, ETH., research report 2002-06., Zurich, Switzerland.
- [36] M. Torrilhon, *J. Comp. Phys.* 192 (2003) 73–94.
- [37] M. Torrilhon, *Journal of Plasma Physics* 69 (2003) 253–276.
- [38] G. Tóth, *J. Comp. Phys.* 161 (2000) 605–652.
- [39] A. Zachary, A. Malagoli, P. Colella, *SIAM Journal Scientific Computing* 15 (1994) 263–284.

Curriculum Vitae

Include your *curriculum vitae* here detailing your background, education, and professional experience.